



University of
Massachusetts
Amherst

A single molecule visualization of DNA diffusion and partitioning in model porous materials.

Item Type	Dissertation (Open Access)
Authors	Nykypanchuk, Dmytro
DOI	10.7275/54ey-mt65
Download date	2025-11-03 23:46:25
Link to Item	https://hdl.handle.net/20.500.14394/11047



312066 0288 8646 6

**A SINGLE MOLECULE VISUALIZATION OF DNA DIFFUSION AND
PARTITIONING IN MODEL POROUS MATERIALS**

A Dissertation Presented

by

DMYTRO NYKYPANCHUK

Submitted to the Graduate School of the
University of Massachusetts Amherst in partial fulfillment
of the requirements for the degree of

DOCTOR OF PHILOSOPHY

February 2005

Polymer Science and Engineering

© Copyright by Dmytro Nykypanchuk 2005

All Rights Reserved

**A SINGLE MOLECULE VISUALIZATION OF DNA DIFFUSION AND
PARTITIONING IN MODEL POROUS MATERIALS**

A Dissertation Presented

by

DMYTRO NYKYPANCHUK

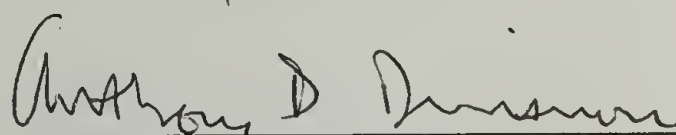
Approved as to style and content by:



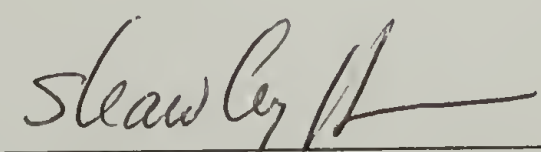
David A. Hoagland, Chair



Helmut H. Strey, Member



Anthony Dinsmore, Member



Shaw Ling Hsu, Department Head
Polymer Science and Engineering

ACKNOWLEDGMENTS

I want to thank my advisors, David A. Hoagland and Helmut H. Strey, for their support and guidance through these years. I would also like to thank my committee member, Anthony Dinsmore, for his valuable comments and suggestions.

I want to express my appreciation to Muthukumar and Joey Kong for inspiring discussions and comments regarding my research, and to Thomas P. Russell, Alan J. Lesser, and James D. Capistran for the help in my professional development.

I wish to acknowledge financial support from NSF-MRSEC, University of Massachusetts Amherst.

I am indebted to my family for their support and love.

ABSTRACT

A SINGLE MOLECULE VISUALIZATION OF DNA DIFFUSION AND PARTITIONING IN MODEL POROUS MATERIALS

FEBRUARY 2005

DMYTRO NYKYPANCHUK, DIPLOMA, IVAN FRANKO UNIVERSITY

M.S., UNIVERSITY OF MASSACHUSETTS AMHERST

Ph.D., UNIVERSITY OF MASSACHUSETTS AMHERST

Directed by: Professor David A. Hoagland and Professor Helmut H. Strey

We developed an experimental approach that enables molecule visualizations of macromolecular diffusion and partitioning within well-defined pores. By colloidal templating, two-dimensional arrays of open, submicron cavities interconnected by small holes were created in dense polyacrylamide gels. Cavity size of the arrays varied from 600 to 1400 nm, with the corresponding holes about 4-5 times smaller. DNA molecules of sizes from 2.69 to 48.5 kbp were inserted into the cavity arrays and monitored by fluorescent microscopy. In video sequences, individual chain positions identified as the chains diffused under Brownian motion over a period of seconds to tens of minutes. For larger chains, dynamic configurations were resolved during the motion.

Over full range of molecular and pore sizes, we found that chain dynamics could be understood through the entropic barriers transport mechanism. At high confinement (large molecules in small cavities), this mechanism produces unexpected trends, for example, independence of diffusion coefficient on molecular size or faster diffusion of molecules in smaller pores. These trends reflect segmental excluded volume.

Complicated dynamics akin to motion of an inchworm characterized the largest DNA chains, those with radius of gyration larger than the cavity radius.

Diffusion of linear and circular DNA molecules was compared for different molecular sizes, and the resulting differences in diffusion coefficient explained by differences in diffusion mechanism; linear molecules translocate through holes by forming loops, while linear chains predominantly translocate by threading one chain end.

A similar colloidal templating approach was also employed to create isolated cavity pair interconnected by a small hole. When templated by bidisperse colloid, the two cavities have unequal diameters. A DNA chain trapped inside such pair partitions unevenly, preferring the larger cavity, which afford greater configurational freedom. This sort of partitioning underlies many separation technologies but had not been visualized previously. The partition coefficient between cavities was measured visually for many combinations of cavity and molecular sizes, trends in this coefficient were then compared to existing theories for polymer partitioning. Good agreement over a two orders-of-magnitude variation of partition coefficient was obtained when effect of excluded volume on confinement free energy was introduced in a mean-field manner.

TABLE OF CONTENTS

	Page
ACKNOWLEDGMENTS	iv
ABSTRACT	v
LIST OF TABLES	ix
LIST OF FIGURES	x
CHAPTER	
1. THEORETICAL MODELS AND EXPERIMENTAL RESULTS ON POLYMER DIFFUSION AND PARTITIONING IN POROUS MEDIA	1
Polymer Dynamics under Confinement.....	1
Polymer Partitioning – Theory and Experiment	7
Single Molecule Imaging in Polymer Physics.....	8
Polymer Transports in Ordered Structures	10
References.....	12
2. EXPERIMENTAL METHODS AND MATERIAL PREPARATION	16
Templating with Colloidal Crystals.....	16
Colloidal Crystal Preparation	17
Surface Modification	19
Template Polymerization	23
Array Characterization	26
DNA labeling and characterization.....	29
Visualization of Diffusion	32
References.....	34

3.	VISUALIZATION OF DNA DIFFUSION UNDER PERIODIC CONFINEMENT	36
	Diffusion Mechanism	36
	Hopping Frequency Distribution	40
	Jumping Direction Distribution	41
	Microscopic vs. Macroscopic Diffusion Coefficient.....	44
	References.....	47
4.	DIFFUSION OF A LINEAR DNA IN AN ARRAY OF SPHERICAL CAVITIES.....	49
	Effect of Molecular Weight	49
	Effect of Cavity Size.....	56
	References.....	60
5.	DIFFUSION OF A CIRCULAR DNA IN AN ARRAY OF SPHERICAL CAVITIES.....	62
	References.....	73
6.	DNA PARTITIONING IN SPHERICAL CAVITIES.....	76
	Weak and Moderate Confinement	76
	Strong Confinement.....	89
	References.....	94
	BIBLIOGRAPHY.....	96

LIST OF TABLES

Table	Page
1. The dimensions of cavities and holes in the templated arrays	55
2. Average number of nicks per circular DNA molecule introduced with nicking enzymes.....	68
3. Measured diffusion coefficients of circular and linear molecules in the cavity array.....	70
4. Experimental parameters	76

LIST OF FIGURES

Figure	Page
1. The schematic of entropic barrier transport mechanism for macromolecular diffusion in a dense heterogeneous medium.....	3
2. Schematic of the geometry used by Muthukumar to predict the effect of molecular weight of polymer on entropic barrier height.	5
3. Schematic of surface modification with 3-glycidoxypropyltrimethoxysilane.....	20
4. 3-Glycidoxypropyltrimethoxysilane thickness measured by ellipsometry on a silicon wafer.....	22
5. Height image of the photopolymerized 80% HEMA hydrogel with embedded 600 nm polystyrene particles after attempt to remove particles with toluene.	24
6. Optical (A) and electron micrographs (B and C) of hydrogels templated with colloidal crystals.	27
7. Fluorescence intensity of TOTO-1 labeled λ -DNA in buffers of different compositions.	31
8. Schematic of the assembly used to fill the spherical cavity arrays with DNA molecules.....	33
9. Visualization of 7.25 kbp DNA trajectories.....	38
10. A sampling at various times of configurations observed for a single 48.5 kbp DNA.....	39
11. Measured values of $P(n)$ (plotted as solid bars) compared to Poisson distributions (plotted as open bars) with identical means.	41
12. Schematic of hopping direction indexing.....	42

13. The histograms of hopping direction distribution measured for 4.69kbp DNA molecules in 920 nm cavity arrays.....	43
14. DNA diffusion analysis.....	46
15. Variation of diffusion coefficient with size of DNA molecules.....	50
16. Variations of reduced diffusion coefficient with DNA size.....	54
17. Change of diffusion coefficient of DNA molecules with the size of cavities in the arrays.....	59
18. Modes of polymer diffusion through a pore for the molecules of various topologies.....	63
19. Jumping frequency distribution of linear and nicked DNA molecules plotted as a probability $P(n)$ of number of jumps n in a time window t	67
20. Jumping frequency distribution for nicked 4.36 kbp DNA molecules plotted as a probability $P(n)$ of number of jumps n in a time window $t=50$ s.....	69
21. Schematic of two-cavity confinement for unequal size cavities.....	77
22. Six frames of 7,249 bp DNA partitioned dynamically between 1,400 and 608 nm diameter cavities.....	79
23. Scanning electron microscope image of templated hydrogels in a point of contact of templated beads and supporting surface.....	80
24. Sedimentation profile of TOTO-labeled DNA given as the optical density of DNA solution as a function of the distance from the center of the centrifuge rotor.....	82
25. The logarithm of relative concentration change with sedimentation time for labeled (solid symbols) and unlabeled (open symbols) DNA.....	83

26. Experiment compared to theory for the Gaussian chain cavity-to-cavity partition coefficient K_p using extreme values for b	85
27. Experiment compared to theory for the Gaussian chain cavity-to-cavity partition coefficient K_p when b is fitted.	87
28. Experiment compared to theory for the cavity-to-cavity partition coefficient K_p	88
29. Free energy histogram for configurations adopted by 48,502 bp DNA in a pair of 920 nm diameter cavities.....	92

CHAPTER 1

THEORETICAL MODELS AND EXPERIMENTAL RESULTS ON POLYMER DIFFUSION AND PARTITIONING IN POROUS MEDIA

Polymer Dynamics under Confinement

Separation of synthetic and biological macromolecules relies, to a great extent, on heterogeneous porous media such as gels. A thorough understanding of diffusion in these dense environments is necessary for designing more efficient separation methods and systems. In particular, this understanding is important for biological macromolecules, where current research focuses on miniaturization and speed of a new generation “chip-based” separation device. Vast experimental and theoretical research in the area of constrained polymer diffusion has produced several models and theories, of which the most important are sieving, reptation, and entropic barrier.[1-9]

The sieving model of constrained diffusion presumes that only molecules or particles smaller than a medium’s pore size can diffuse, and the diffusion coefficient is proportional to the number of paths available for the diffusing species. This concept can be extended to polymer diffusion when the pore size is bigger than the dimensions of the polymer chain. In this case, polymer chains are approximated as hard spheres of effective radius R , which corresponds to an average chain size. The Ogston model and its modifications give a prediction for a diffusion coefficient in a medium constructed of randomly placed “obstacles”:[6, 10]

$$D/D_0 = f_v = \exp(-Kc) \quad (1)$$

where D is the solute diffusion coefficient in the porous medium, D_0 is the solute diffusion coefficient in free solution, f_v is fraction of free available volume, K is a

retardation coefficient, and c is an obstacle concentration. Values of K and c depend on the obstacle geometry and size; the retardation coefficient also depends on the solute size. c is given as number of obstacles per volume, length of obstacles per volume, or surface of obstacles per volume for zero-dimensional, one-dimensional, and two-dimensional gels, respectively. For several simple cases the form of K is also known: for an isotropic array of infinitely long fiber like obstacles (1-D gels) $K \sim (r+R)^2$, where r is the obstacle size; $K \sim (r+R)$ for infinite sheetlike obstacles (2-D gels); and $K \sim (r+R)^3$ for spherical obstacles (0-D gels). Optimal separation is expected when the solute approaches the size of the pores in the separation media. The Ogston model neglects excluded volume in the placement of obstacles.

While the sieving model is conceptually useful for the case of polymers it does not rigorously capture the underlying physical phenomena as chain dimensions become comparable to those of the confining space, conditions for which the sieving model predicts optimal separation. Namely, polymer chains do not behave as hard spheres, and consequently, chain energy changes gradually under different degrees of confinement. Because of flexibility, polymers can fit through openings smaller than any reasonable value of R .

The sieving model is usually applied by fitting experimental data to the model predictions, letting obstacle size be a fitting parameter. Good fits are often obtained, but fitted obstacle sizes are frequently unreasonable.

More recently, a new diffusion model was proposed for the case of intermediate confinement when description of polymer diffusion by sieving fails.[1, 2, 7] This model is based on the fact that in dense heterogeneous media, spatial variation of

confinement produces a change in available chain conformations.[2] Polymer chains partition to the least confining spaces to achieve maximum configurational entropy and minimum free energy (if no enthalpic interactions between the chain and the media are present). Under thermal fluctuations, polymer molecules can diffuse from one local free energy minima to another via crossing of more confined spaces and imposed energy barriers; see Figure 1. Ignoring hydrodynamics and thus focusing on configurational aspects of transport, D depends on the heights of the energy barriers, as follows[1]:

$$D/D_0 = \exp(-\Delta F), \quad (2)$$

where ΔF is the energy barrier. In essence, diffusion becomes entropically activated process.

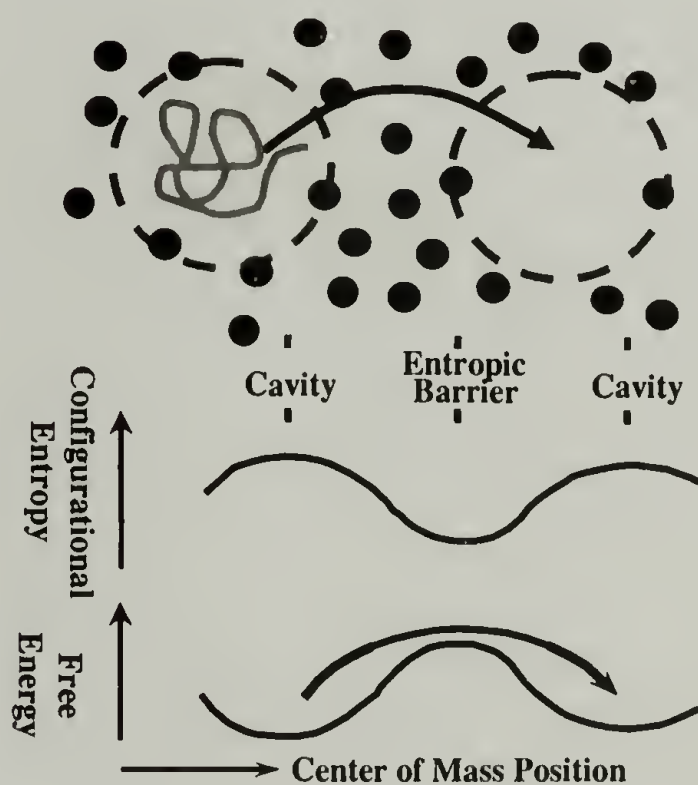


Figure 1. The schematic of entropic barrier transport mechanism for macromolecular diffusion in a dense heterogeneous medium.

In order for entropic barrier model to have predictive power, knowledge of how of free energy ΔF depends on experimental parameters such as polymer size/topology and pore size/geometry is needed. A scaling argument was used to predict dependence of D on the number of segments N for the geometry shown in Figure 2.[1]

$$\frac{D}{D_0} = \exp\left\{-N\left[fc^{-1/\nu} + \left(\frac{1-f}{z} - 1\right)L^{-1/\nu}\right]\right\} \quad (3)$$

$$f=1 \quad \xi \leq 1 \quad (4)$$

$$f = N^{-1}c^{(1/\nu)-1} \quad \xi \gg 1 \quad (5)$$

where L is a cavity size, c is a bottle neck size, f is the fraction of segments in a bottle neck, z is the average number of cavities that contain $(1-f)N$ unconfined segments per bottle neck, $\xi \sim R_{\perp}^2 R_{\parallel}/c^2\lambda$ with R_{\perp}^2 and R_{\parallel} being the components of the radius of gyration of the chain in a plane perpendicular and parallel to the axis of the bottleneck, respectively, and λ is a length of a bottleneck. Equations (4) and (5) describe the limiting cases of weak and strong confinement in a bottleneck, respectively. For experiments, the most relevant situation is when ξ is greater than unity but not by much (intermediate confinement). Here, Muthukumar and Baumgärtner [1, 7] predict

$$\ln\left(\frac{D}{D_0}\right) = AN - s \quad (6)$$

where A is negative and proportional to $(1/L)^{1/\nu}$, and s is proportional to $c^{-1}[1-z^{-1}(c/L)^{1/\nu}]$. A and s parameters are not given explicitly, and exact predictions on how the bottleneck and cavity sizes affect the diffusion at given N are impossible to make if both dimensions are changed simultaneously.

The entropic barrier regime corresponds to intermediate confinement ranges, where the regime represents the crossover from sieving to reptation. The entropic barrier depiction is a relatively recent view of transport, but potentially provides the richest opportunities for tuning media properties via variations in confining geometry.

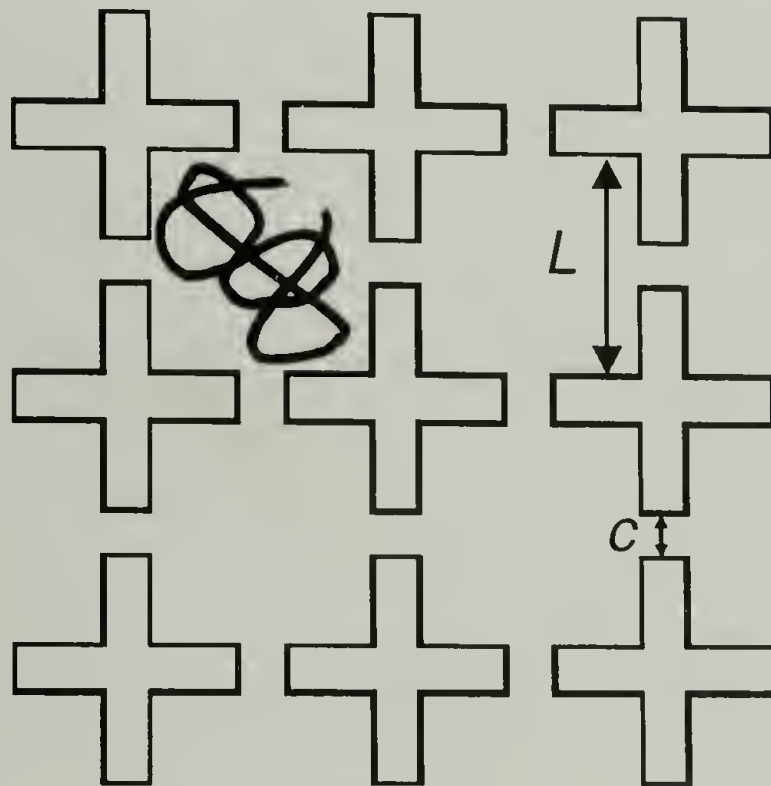


Figure 2. Schematic of the geometry used by Muthukumar [1] to predict the effect of molecular weight of polymer on entropic barrier height.

The reptation theory, proposed by de Gennes and later confirmed by experimental observations in polymer melts and concentrated solutions, describes chain motion constricted to a fictitious tube in which molecules diffuse only through curvilinear motion along the tube axis.[4, 5, 11, 12] Mobility for the reptation model is

governed by the chain length L , where $D \sim L^{-2}$. This mechanism usually requires high degree of confinement, with heterogeneities on the order of the molecular persistence length or smaller.

Until recently, diffusion was exclusively studied measuring bulk properties – a macroscopic approach. Usually, the dependency of diffusion coefficient on polymer molecular weight (M) was taken as evidence of a specific diffusion mechanism. For reptation, the functional form of $D(M)$ is well established, but the analogous dependences are less evident for the sieving and entropic barrier transport mechanisms. For both, D should depend exponentially on chain dimensions or chain dimension raised to some power. For the former, R is the governing parameter, while for the latter, the number of chain segments N is the crucial parameter. The Microscopic approach to diffusion (direct visualization) allows verification of the diffusion mechanism directly. Such experiments for reptating systems have been performed and qualitatively agree with the theoretical predictions.[11, 12] On the other hand, the diffusion experiments in porous environments where the confinement dimensions and geometries are well characterized and controlled have not yet been performed. This absence diminishes our ability to match theory with experiment quantitatively, making scaling relations the primary evaluation tool.

The exact conditions at which each of the three mechanisms prevail are the subject of debate,[13, 14] and it remains problematic to predict, *a priori*, the transport properties of a polymer in a given dense environment.

Polymer Partitioning – Theory and Experiment

The macromolecular mobility within the entropic barrier transport mechanism is governed by spatial variations in the confining energy along the path of the diffusing molecule. Thus, it is important to know how the energy of confinement changes with the size of macromolecules and with the size of a confining space.

Equilibrium partitioning of solute between two regions of dissimilar free energy is quantified through the partition coefficient K , the ratio of the two solute concentrations. By picking an unconfined region as the reference state, $K = \exp(\Delta S_c/k)$, where ΔS_c is the confinement entropy, and k is the Boltzmann constant. Employing a Gaussian description for a confined chain and allowing the chain to sample equally all configurations not intersecting pore boundaries, Casassa[15, 16] developed the earliest theories of ΔS_c germane to flexible polymers. Analytical results were reported for chains trapped within spherical, cylindrical, and slit-like pores. For a polymer partitioned into a pore of comparable or smaller size a , a Gaussian chain description leads to a scaling relationship, $\Delta S_c \sim N/a^2$. Scaling relationships for ΔS_c are extensively discussed in de Gennes.[17]

Several features missing in a Gaussian chain description can significantly influence ΔS_c . In a good solvent, excluded volume effectively precludes overlap of chain segments, and an unconfined flexible polymer responds by swelling. Pore walls frustrate this swelling, thereby increasing $|\Delta S_c|$ from its Gaussian chain value. For chains of finite stiffness/length, confinement models must replace Gaussian chain statistics with wormlike chain statistics.[18-21] Assessed at equal R , $|\Delta S_c|$ for a wormlike chain is usually less than for a Gaussian chain (pore geometry affects the

direction of the trend). Finally, nondilute chains in a good solvent feel each other even as they interact with pore walls, and the correlation length of the bulk solution supersedes R as the polymer length governing partitioning. Computational methods, along with more sophisticated scaling approaches, address deficiencies of the Gaussian chain description, and detailed results have been reported for several idealized confinement geometries.[21-27]

Sorption, size exclusion chromatography, and interferometry experiments have all provided average K values for flexible polymers partitioned from solution into bulk materials possessing geometrically ill characterized and/or polydisperse pores.[28-31] For dilute polymer solutions, trends fall roughly in line with predictions derived using the Gaussian chain description. Recently, a conductance method has been applied to the study of polymers partitioned within membrane-bound protein nanopores;[32] systematic variations of the chemistry, geometry, and size of such nanopores are difficult or impossible.

Single Molecule Imaging in Polymer Physics

Single molecule experiments have certain advantages over traditional ensemble average measurements. In traditional experiments, one gets a measurement over the whole population, and information about the property distribution within the population is lost and subpopulations in the system are hard to identify. For polymers, a single molecule experiment can provide information on the conformation distribution within the temporal, spatial, or reaction coordinates, and in dynamics experiments, reveal the time trajectories of an individual member of an ensemble.[33]

Single molecule imaging comprises a substantial part of single molecule methods used in polymer physics. Experimentally, fluorescent microscopy, scanning force microscopy (SFM), and a combination of the two - near field microscopy - are the most commonly used methods for the imaging of single macromolecules. These methods have different niches. The optical techniques provide good resolution in time, but the spatial resolution is limited to several hundred nanometers. Thus, most commonly, optical techniques are used for dynamic measurements or imaging of large macromolecules ($>1\mu\text{m}$). SFM provides excellent resolution in space, on the order of nanometers, but its capability to monitor dynamic processes is limited to slow, on a time scale of seconds, events. Moreover, SFM measurements are conducted on surfaces, with extrapolation the surface measurement to macromolecules in bulk a major concern. Near field microscopy aspires to blend the advantages of optical and SFM methods, but, at the same time, it blends the disadvantages of the two. Near field microscopy does provide the spatial resolution on the order of tens of nanometers, and it can also monitor fast processes, but it is still challenging to follow the spatial and temporal trajectories simultaneously.[34-37]

To date, single molecule imaging has not offered breakthrough results in polymer science. However, this method has provided a way to confirm directly many important theoretical concepts and trends inferred through indirect measurement. In particular, regarding polymer dynamics, reptation was visualized in concentrated DNA and actin filament solutions.[11, 12, 38] Also, the coil-globule transition of polyelectrolytes,[39] single molecule elasticity and stiffness,[40-43] and interactions between macromolecules[44] have been studied with single molecule imaging methods.

The future for the use of single molecule imaging methods looks increasingly bright and promising, with the improvement of imaging techniques and fluorescent tags.

Polymer Transports in Ordered Structures

An ability to make molecular size and geometrically well controlled pores opens a window of opportunity for study of the effect of confinement on such important processes as macromolecule electrophoresis, filtration, and diffusion. Many reports that have appeared in recent years explore self-assembly and lithography to create media for macromolecule separation with pores or obstacles which can be tailored in size and geometry.[45-57]

Many have studied DNA electrophoresis in effort to obtain more efficient separation and to develop DNA manipulation devices. These reports focus on materials produced by lithographic methods, aiming to create “lab on a chip” technologies. Channels with alternating regions of different height,[45, 53-55] ratchet-like structures,[47, 49] and post arrays[46, 57] have been created and the electrophoresis of DNA in the structures investigated. Entropic recoil of macromolecules from an array of posts has been observed [50] but a quantitative description of the phenomenon was lacking because of the geometrical complexity of the system.

Electrophoresis in these system showed promise for miniature separation devices, especially for large – hundreds of kilobase pairs – DNA. Literature studies also revealed complications associated with the use of silicon – the material essential for lithography. The main complications are the presence of electrosmotic flow, which is hard to control, and high mismatch of dielectric constants between water solution and

the silicon. The mismatch leads to locally complex electric field lines which govern the mobility of the polymer in those structures. The aforementioned complications are not necessarily harmful for the macromolecule separation but prevent the use of such systems for study of polymer physics.

Fewer reports describe the use of self-assembled structures for study of polymer behavior under confinement. Employing colloidal templating, the entropic localization, of polymer inside cavities in hydrogel was demonstrated, chain partitioned to the cavities in preference to the hydrogel matrix.[58, 59] The electrophoretic migration of DNA molecules in interstitial spaces of a colloidal crystal was also measured, and apparent reptation dynamics was observed.[56] The confining geometry in the latter case was complicated and not systematically varied. Choice of silica particles to create the colloidal crystal introduced the same problems discussed above for lithographic methods.

Natural porous materials with well defined pores of molecular size scale have also been explored as a means to study polymer transport and confining effects.[32] Such studies have examined polymer translocation through, and partitioning in, membrane ion channels. Pore geometry and chemistry is not controlled and hard to vary.

Until this study, macromolecular transport in ordered and geometrically well defined structures was investigated solely in the context of the electrically driven migration of chains. No diffusion studies in defined porous materials have ever been performed.

References

1. Muthukumar, M. and A. Baumgärtner, *Macromolecules*, 1989. **22**(4): p. 1937-1941.
2. Muthukumar, M. and A. Baumgärtner, *Macromolecules*, 1989. **22**(4): p. 1941-1946.
3. Zimm, B.H. and O. Lumpkin, *Macromolecules*, 1993. **26**(1): p. 226-234.
4. Doi, M. and S.F. Edwards, *J. Chem. Soc. Faraday Trans. II*, 1978. **74**: p. 1789-1801.
5. deGennes, P.G., *J. Chem. Phys.*, 1971. **55**(2): p. 572-579.
6. Ogston, A.G., *Trans. Faraday. Soc.*, 1958. **54**: p. 1754-1757.
7. Muthukumar, M., *J. Non-Cryst. Solids*, 1991. **131**: p. 654-666.
8. Smisek, D.L. and D.A. Hoagland, *Science*, 1990. **248**: p. 1221-1223.
9. Slater, G.W., P. Mayer, and G. Drouin, *Methods Enzymol.*, 1996. **270**: p. 272-295.
10. Rodbard, D. and Chrambac.A, *Proc. Natl. Acad. Sci. U. S. A.*, 1970. **65**(4): p. 970-&.
11. Käs, J., H. Strey, and E. Sackmann, *Nature*, 1994. **368**: p. 226-229.
12. Smith, D.E., T.T. Perkins, and S. Chu, *Phys. Rev. Lett.*, 1995. **75**(22): p. 4146-4149.
13. Masaro, L. and X.X. Zhu, *Prog. Polym. Sci.*, 1999. **24**(5): p. 731-775.
14. Guillot, G., L. Läger, and F. Rondelez, *Macromolecules*, 1985. **18**(12): p. 2531-2537.

15. Casassa, E.F., J. Polym. Sci. B, 1967. 5(9PB): p. 773-778.
16. Casassa, E.F. and Y. Tagami, Macromolecules, 1969. 2(1): p. 14-&.
17. de Gennes, P.G., *Scaling Concepts in Polymer Physics*. 1979, Ithaca: Cornell Univ. Press.
18. Giddings, J.C., et al., J. Phys. Chem., 1968. 72(13): p. 4397-&.
19. Davidson, M.G., U.W. Suter, and W.M. Deen, Macromolecules, 1987. 20(5): p. 1141-1146.
20. Odijk, T., Macromolecules, 1983. 16(8): p. 1340-1344.
21. Teraoka, I., K.H. Langley, and F.E. Karasz, Macromolecules, 1992. 25(23): p. 6106-6112.
22. Muthukumar, M., Journal of Chemical Physics, 2003. 118(11): p. 5174-5184.
23. Limbach, K.W., J.M. Nitsche, and J. Wei, AIChE J., 1989. 35(1): p. 42-52.
24. Cifra, P. and T. Bleha, Macromolecules, 2001. 34(3): p. 605-613.
25. Tsonchev, S. and R.D. Coalson, Chem. Phys. Lett., 2000. 327(3-4): p. 238-244.
26. Jaeckel, A. and J. Dayantis, J. Phys. A, 1994. 27(23): p. 7719-7731.
27. Jaeckel, A. and J. Dayantis, J. Phys. A, 1994. 27(8): p. 2653-2667.
28. Colton, C.K., C.J. Lai, and C.N. Satterfield, AIChE J., 1975. 21(2): p. 289-298.
29. Satterfield, C.N., et al., AIChE J., 1978. 24(5): p. 937-940.
30. White, J.A. and W.M. Deen, Macromolecules, 2000. 33(22): p. 8504-8511.

31. Teraoka, I., *Macromolecules*, 1996. **29**(7): p. 2430-2439.
32. Bezrukov, S.M., et al., *Macromolecules*, 1996. **29**(26): p. 8517-8522.
33. Weiss, S., *Science*, 1999. **283**(5408): p. 1676-1683.
34. Garcia-Parajo, M.F., et al., *Ultramicroscopy*, 1998. **71**(1-4): p. 311-319.
35. Ha, T., et al., *Proc. Natl. Acad. Sci. U. S. A.*, 1996. **93**(13): p. 6264-6268.
36. Kirsch, A.K., C.K. Meyer, and T.M. Jovin, *J. Microsc.-Oxf.*, 1997. **185**: p. 396-401.
37. Betzig, E. and R.J. Chichester, *Science*, 1993. **262**(5138): p. 1422-1425.
38. Perkins, T.T., D.E. Smith, and S. Chu, *Science*, 1994. **264**: p. 819-822.
39. Kiriya, A., et al., *Journal of the American Chemical Society*, 2002. **124**(45): p. 13454-13462.
40. Bustamante, C., et al., *Science*, 1994. **265**(5178): p. 1599-1600.
41. Perkins, T.T., et al., *Science*, 1994. **264**(5160): p. 822-826.
42. Perkins, T.T., et al., *Science*, 1995. **268**(5207): p. 83-87.
43. Perkins, T.T., D.E. Smith, and S. Chu, *Science*, 1997. **276**(5321): p. 2016-2021.
44. Friddle, R.W., et al., *Biophysical Journal*, 2004. **86**(3): p. 1632-1639.
45. Han, J. and H.G. Craighead, *J. Vac. Sci. Technol. A-Vac. Surf. Films*, 1999. **17**(4): p. 2142-2147.
46. Tegenfeldt, J.O., et al., *Anal. Bioanal. Chem.*, 2004. **378**(7): p. 1678-1692.

47. Huang, L.R., et al., *Anal. Chem.*, 2003. **75**(24): p. 6963-6967.
48. Cabodi, M., S.W.P. Turner, and H.G. Craighead, *Anal. Chem.*, 2002. **74**(20): p. 5169-5174.
49. Huang, L.R., et al., *Physical Review Letters*, 2002. **89**(17).
50. Turner, S.W.P., M. Cabodi, and H.G. Craighead, *Physical Review Letters*, 2002. **88**(12).
51. Foquet, M., et al., *Anal. Chem.*, 2002. **74**(6): p. 1415-1422.
52. Korlach, J., et al., *Biophysical Journal*, 2002. **82**(1): p. 361A-361A.
53. Han, J.Y. and H.G. Craighead, *Anal. Chem.*, 2002. **74**(2): p. 394-401.
54. Han, J. and H.G. Craighead, *Science*, 2000. **288**(5468): p. 1026-1029.
55. Han, J., S.W. Turner, and H.G. Craighead, *Physical Review Letters*, 1999. **83**(8): p. 1688-1691.
56. Meistermann, L. and B. Tinland, *Phys. Rev. E*, 2000. **62**(3): p. 4014-4017.
57. Kaji, N., et al., *Anal. Chem.*, 2004. **76**(1): p. 15-22.
58. Liu, L., P.S. Li, and S.A. Asher, *Nature*, 1999. **397**(6715): p. 141-144.
59. Liu, L., P.S. Li, and A.S. Asher, *Journal of the American Chemical Society*, 1999. **121**(16): p. 4040-4046.

CHAPTER 2

EXPERIMENTAL METHODS AND MATERIAL PREPARATION

In this chapter we describe the general experimental procedures and materials used throughout this work unless specified otherwise in a discussion.

Templating with Colloidal Crystals

Controlled drying of a suspension of monodisperse colloidal particles can produce ordered particle structures on a surface. By changing drying conditions, solvent nature, substrate and particle surface chemistry, a variety of structures is obtainable. The main features of this structure formation mechanism are known, but the process is difficult to control precisely due to its complexity.[1-7]

The following system variables are critical to particle assembly: solvent drying rate, which determines the rate at which particles are brought to the drying front and the forces at which particles are held to this front; solvent surface-tension and particle wettability, which affect the quality of the structure via the capillary forces imparted on the particles during the final stages of drying; the particle-particle and particle-surface interactions, which should be repulsive or only weakly attractive to generate highly ordered structures (in the case of strong, attractive interactions, structural annealing is impossible, leading to a poor degree of order); and substrate wettability, which stabilizes the thin liquid films during the final stages of drying. (Thin films are unstable on non-wetted surfaces.)

The colloidal crystal can be infused with a polymerizable liquid. After polymerization, the particles can be removed by soaking the material in a solvent specific for the particles, leaving behind the porous material with pores of controlled geometry.[8-10] While a variety of systems produce excellent colloidal ordering, the direct use of such systems for colloidal templating is often inappropriate. The DNA diffusion experiment imparts restrictions on the kinds of materials we can use for templating. Ideally we would like to minimize the dielectric constant mismatch between the templated material and the solvent, while producing arrays that are inert to DNA molecules, optically transparent, and conductive. Hydrogels that do not interact with DNA molecules are good material candidates. To infuse a colloidal crystal with the hydrogel precursor, the templating particles as well as substrate surfaces should be wettable by the low viscosity precursor. Otherwise, capillary forces prevent infusion of the colloidal crystal with the precursor.

Based on these considerations, we developed the following techniques and materials for the colloidal templating.

Colloidal Crystal Preparation

A variety of solvents and techniques were explored for colloidal crystal preparation. Methanol, ethanol, iso-propanol, water, and mixtures of these solvents were tried as volatile solvents for the colloidal suspension. Evaporation rate for each was controlled by the temperature (4°C – 40°C) and solvent vapor pressure. The following procedure was developed that provides good quality colloidal crystals in a short time.

A suspension of nearly monodisperse polystyrene spheres (polydispersity < 1.5%) purchased from Duke Scientific Corp. was purified by repeating three times successive sedimentation, decantation of supernatant, and addition of clean reverse osmosis (RO) water. The sedimentation was done at relative centrifugal forces ranging from 2000 to 12000 g for 10 – 90 min depending on the particles' size. It is important to spin particles only for the time necessary to achieve complete sedimentation; longer spinning times lead to particle aggregation and difficulties in particle re-suspension. The sedimentation should also be done at the minimum force required to sediment particles in the reasonable amount of time. The particles' re-suspension was done by simple vortexing; sonication did not improve the quality of re-suspension and was not used in most cases.

After cleaning, a 0.33 wt.% suspension of the particles was prepared in 80 v.% ethanol solution in water. The final suspension quality was better when water was added before addition of ethanol to the particles.

A droplet (25-45 μ l) of the suspension was deposited on a functionalized glass cover slide and dried under ambient laboratory conditions to form predominantly 2-D colloidal crystal. The glass functionalization will be described in a subsequent section. The suspension concentration and ethanol content were slightly adjusted for different particle sizes and change in room temperature and humidity to maximize the yield of a two-dimensional colloidal crystal.

The deposited colloidal crystal on the glass substrate was covered with a glass cover slip separated from the substrate by 0.17 mm glass spacers coated with a small amount of vacuum grease. The assembly was used within one day for hydrogel

polymerization. Longer waits before the polymerizations led to incomplete infusion with a hydrogel precursor and numerous voids in the resulting hydrogel film with embedded particles.

Surface Modification

The ideal substrate to form colloidal crystals with a high degree of order is one that is completely wetted by the solvent in the colloidal suspension. On the other hand, the ideal support for colloidal crystals during infusion with hydrogel precursor is one that allows for good wetting with the precursor and at the same time does not reduce the interaction between the particles and the support. Sufficient interaction must be maintained to overcome Brownian motion or flow during the infusion that would move particles around, thus destroying the order in the colloidal crystal. The clean glass cover slips are ideal for the first task – to form colloidal crystals – but they are unsatisfactory for the infusion with hydrogel precursor. Low interaction between the polystyrene colloidal particles and glass substrate does not allow infusion of single layer colloidal crystals with monomer solution without the destruction of the crystals. The multilayer colloidal crystals can be infused with the hydrogel precursor while supported on the neat glass without crystal destruction. If the multilayers coexist with the single layers on the same substrate, the particles forming the single layers are washed of into the bulk of the hydrogel which makes the hydrogel opaque and hinders observation of templated structures with optical microscopy. Hence, it is necessary to tune the surface properties so that the surface is still wetted with hydrogel precursor and colloidal particles do not stick to the surface during suspension evaporation. Once the suspension

is dried out and the colloidal crystal is formed, the affinity of the particles to the surface should increase irreversibly.

Various alkyl silanes – Sigmacote™ (Sigma), vinyltrimethoxysilane (Aldrich), 3-glycidoxypropyltrimethoxysilane (**GS**) (Aldrich), and hydrolyzed **GS** - were grafted to the glass surface in order to control the surface hydrophobicity and particle adhesion. After silane grafting, all surfaces except hydrolyzed **GS** were hydrophobic and only poor quality colloidal crystals could be obtained.

The surfaces with hydrolyzed **GS** allow for highly ordered structures of particles and their infusion with hydrogel precursor. The scheme of **GS** grafting to glass cover slip and **GS** hydrolysis is shown in Figure 3.

The degree of hydrophobicity of the surface and adhesion strength of the particles to the surface can be controlled by changing the time of substrate exposure to the silane solution and the time of hydrolysis. Figure 4 shows the grafted layer thickness of **GS** on an oxidized silicon wafer measured by ellipsometry. An oxidized silicon surface was used to mimic glass. The general trends in the silane adsorption and hydrolysis should be the same on both surfaces.

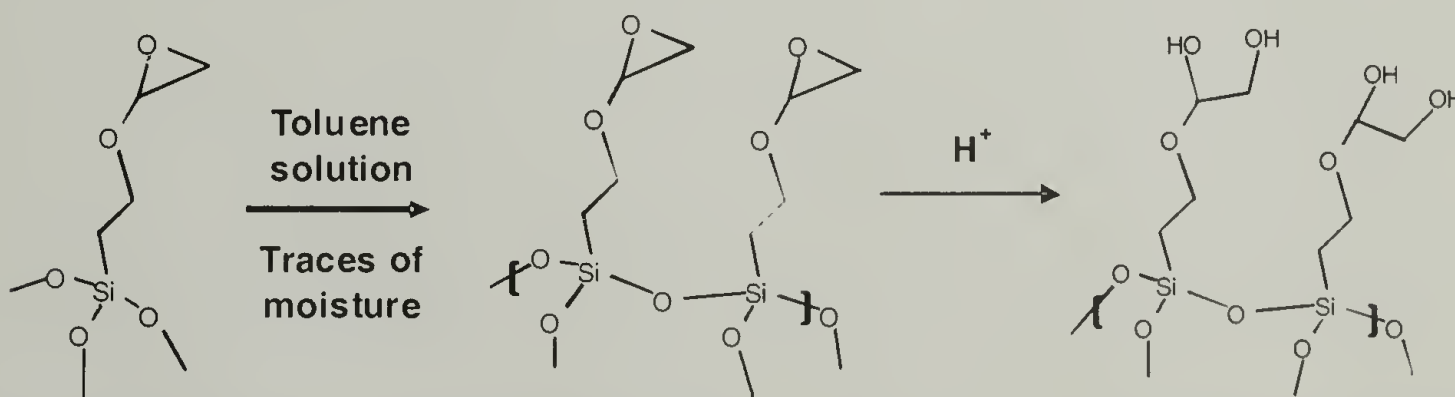


Figure 3. Schematic of surface modification with 3-glycidoxypropyltrimethoxysilane.

We have found a linear dependence of **GS** layer thickness with time of treatment for **GS** solution in toluene, Figure 4A. Such behavior indicates that **GS** forms

multilayers on the glass if adsorbed from the solution. The acidic hydrolysis of **GS** with 0.01M HCL makes surfaces more hydrophilic – dewetting does not occur while drying the suspension. During one hour treatment with HCL, the **GS** layer thickness does not change; for exposures longer than one hour the thickness gradually decreases, Figure 4B.

The thickness measurements correlated well with the results of colloidal crystal deposition and particle adhesion to the surface during infusion with hydrogel precursor. All other conditions being equal, the thicker the initial **GS** layer, the stronger the final adhesion of particles to the surface was. The longer hydrolysis times led to better quality colloidal crystals, but adhesion of the colloidal crystals to the surface starts to deteriorate for hydrolysis times above one hour. The experimental conditions were chosen by minimizing the time of **GS** adsorption and maximizing time of hydrolysis under which satisfactory adhesion of colloidal particles was observed. Longer adsorption times and shorter hydrolysis times resulted either in poor packing of particles on the surface or excessive adhesion of the particles which complicated the separation of formed hydrogels with embedded particles from the surface.

In the optimized procedure, the glass cover slips were cleaned with Nochromix solution in concentrated sulfuric acid. The cover slips were rinsed with ample RO water, dried in a stream of nitrogen, treated for 15 min with 10% solution of **GS** in toluene, and then washed with ethanol and water. A droplet of 0.01M HCL was put in the middle of the cover slide and left for approximately 40 minutes. The glass slides were washed with RO water, dried in a stream of nitrogen, and immediately used as a substrate for colloid crystal deposition.

This procedure should be considered as a generalized guideline only, as the adsorption and hydrolysis times were slightly adjusted depending on the toluene and glass cover slip batch. The attempts to conduct surface modification under better controlled conditions – in the gas phase – were unsuccessful; the resulting surfaces did not provide enough adhesion between particles and the surface to retain the colloidal crystal structure during the infusion with the hydrogel precursor.

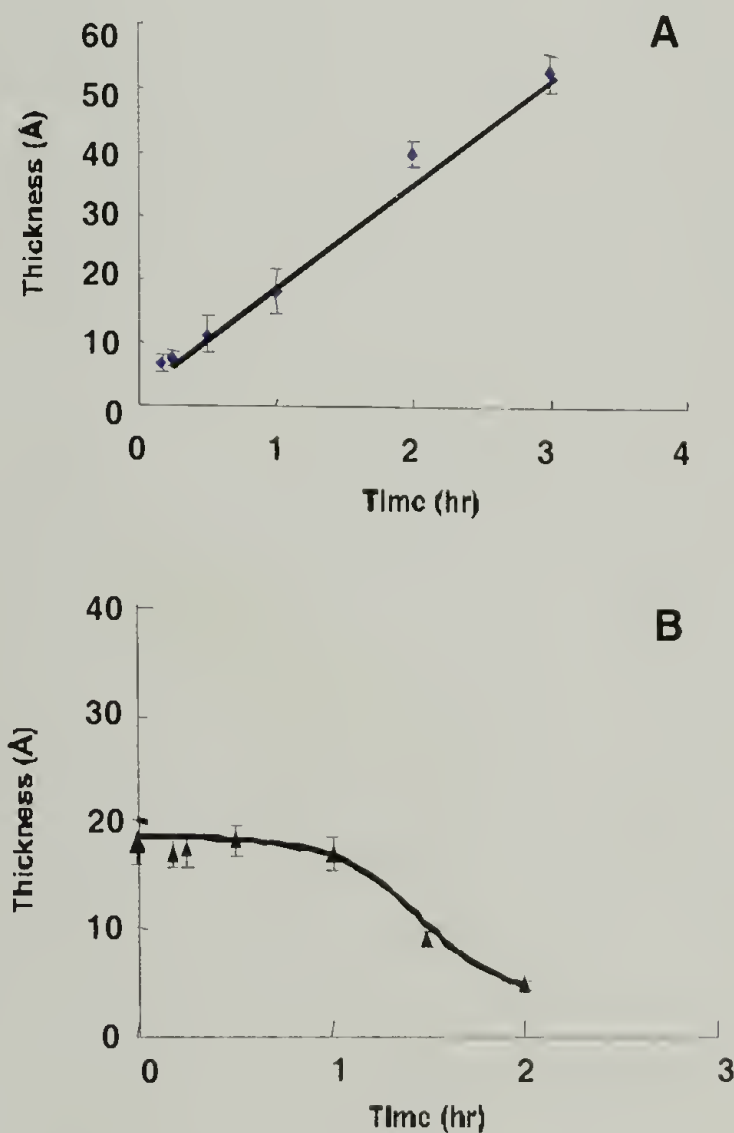


Figure 4. 3-Glycidoxypropyltrimethoxysilane thickness measured by ellipsometry on a silicon wafer. **A** – effect of adsorption time on **GS** layer thickness; adsorption done from 10% **GS** solution in toluene. **B** – change of **GS** layer thickness during its exposure to 0.01N solution of HCl.

Template Polymerization

Colloidal crystals provide templates to create materials with well defined pores. A precursor of a solid material can be infused into the colloidal particle structure and solidified.[8-10] The colloidal particles can be removed with a specific solvent, leaving behind a porous material. The requirements for the matrix forming these porous materials, in regard to our experiment, were discussed above. Our approach is to use chemically cross-linked hydrogels which are inert to DNA molecules. 2-Hydroxyethyl methacrylate (HEMA), HEMA and ethyleneglycol dimethacrylate mixtures, ethyleneglycol diacrylates, and acrylamide with N,N'-bis-acrylamide as a crosslinking agent were tested as possible materials for the template.

The monomer solutions were polymerized by photopolymerization and redox polymerization. Photopolymerization was proven ineffective. The photopolymerized hydrogels had high background fluorescence, as detected by fluorescence microscopy, which makes such materials unsuitable for the diffusion study by single molecule microscopy. The fluorescence in the materials was most probably due to initiator (2-bethyl-2-(dimethyl-amino)-4'-morpholino-butiro-phenon) residues. Using atomic force microscopy, Figure 5, we have also found that templating polystyrene particles in many cases could not be dissolved after UV illumination and were impossible to remove from the hydrogel film. For redox polymerization, we used ammonium persulfate as an initiator and N,N,N',N'-Tetramethylethylenediamine (TEMED) as a starter. Out of all aforementioned monomers, only acrylamide/N,N'-bis-acrylamide mixture, produced optically transparent hydrogels, at desired monomer concentrations.

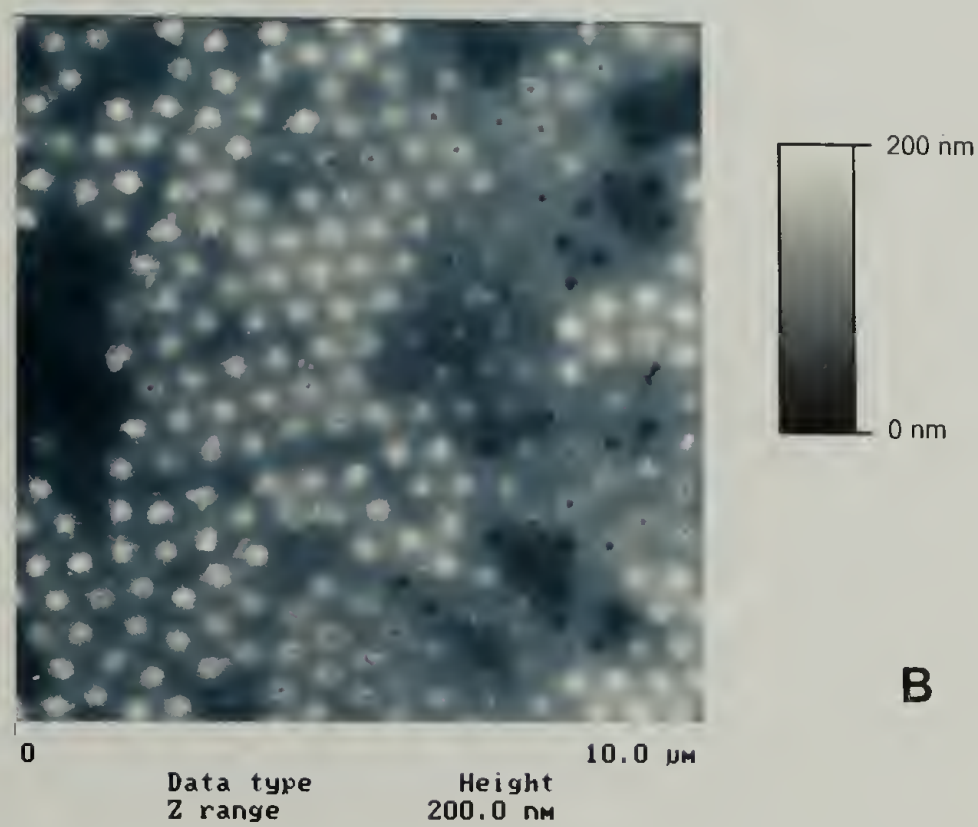
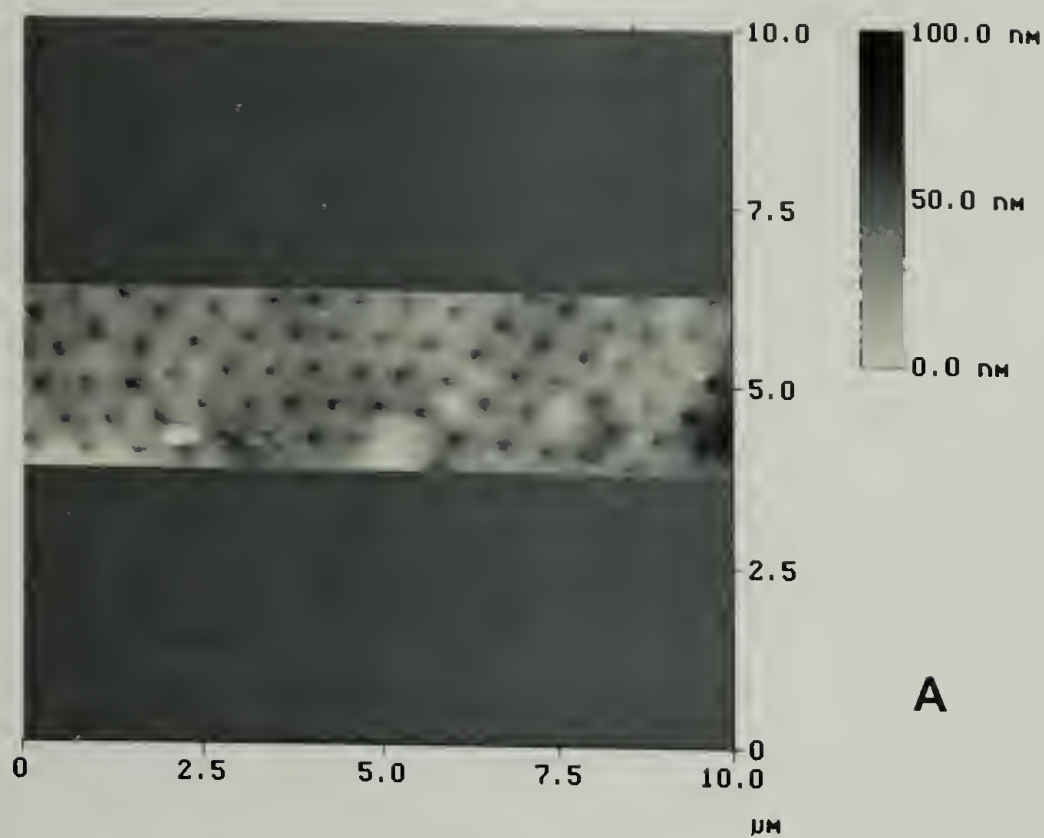


Figure 5. Height image of the photopolymerized 80% HEMA hydrogel with embedded 600 nm polystyrene particles after attempt to remove particles with toluene. Part A shows successful removal and part B unsuccessful removal of the particles.

The composition of the acrylamide hydrogels was adjusted to obtain minimum swelling of the gel while maintaining good optical and mechanical properties. Swelling studies were done by measuring the weight increase of the gel during equilibration in a buffer.

The following procedure was used throughout this work to obtain a hexagonal array of spherical cavities unless specified otherwise. The hydrogel was produced by radical polymerization of 30 wt.% solution of acrylamide/*N,N'*-bis-acrylamide (crosslink density 10%). Prior to polymerization, the monomer solution was degassed by bubbling nitrogen for 10 minutes. Ammonium persulfate was used as an initiator at approximately 0.1 wt.% and TEMED was used as a starter at ~0.2% concentration (both purchased from Sigma-Aldrich). Immediately after the starter was added, the monomer solution was poured in a small (30mm diameter) Petri dish containing colloidal crystals sandwiched between cover slides. The cover slides were positioned in the Petri dish to form a 45° angle with the dish bottom. The capillary forces draw the monomer solution into the ~200µm slit formed by two cover slides that sandwich the colloidal crystal. Polymerization was carried out for approximately 40 minutes.

The resulting hydrogel film, with an embedded array of colloidal particles on one side, was carefully separated from the glass substrate and put in toluene (~10 ml) for at least several hours and up to one day. Toluene was exchanged once during this period. The exposure of the hydrogel to the toluene for a day does not visibly change the gel itself. The monitoring of a gel weight in toluene (1g of the gel in 20ml of toluene) for several weeks with frequent change of the solvent did not reveal any weight change of the gel. However, we expect that longer exposures of the hydrogels to larger

amounts of toluene may result in a change of gel dimensions and/or properties due to small but non-negligible solubility of toluene in water and visa versa and resulting change of solvent quality. In most cases one day exposure of hydrogel film to toluene was enough to remove embedded polystyrene colloidal particles. In some cases the particles did not dissolve completely in the areas of multilayered structures, leaving behind small patches of embedded particles visually located in the top layers of the multilayered colloidal crystal. The particles forming single layer colloidal crystal always dissolve in less than one day.

After extraction of polystyrene particles with toluene, the hydrogel film was washed in an ample amount of water and equilibrated in a buffer solution (40mM Tris-Acetate buffer, pH=8 with 1mM EDTA – 1xTAE – and 10mM NaCl) for at least three days at 4°C. We observed insignificant swelling of the hydrogel films resulting in a change in linear dimensions of 1-2%. After equilibration, the hydrogel films were degassed under reduced pressure to insure absence of trapped air in the arrays. The hydrogel films were then stored in tightly sealed containers in a refrigerator at 4°C and used for the diffusion study within two weeks after preparation.

Array Characterization

The array morphology was characterized with optical microscopy and scanning electron microscopy. Both methods confirmed excellent replication of a colloidal crystal structure in a hydrogel, as displayed in Figure 6.

Optical microscopy was used to monitor the structure replication and general integrity of the structure. It was also used to measure the dimensions of replicated

spherical cavities after gel equilibration in the buffer. The final magnification obtained with optical microscopy was determined by taking pictures of a diffraction grating. To minimize the error in measurement, the length of a cavity string containing twenty cavities was measured within the array. Such measurements were repeated along three directions aligned with the colloidal crystal orientation. The deviation between measurements irrespective of measurement direction did not exceed 1%.

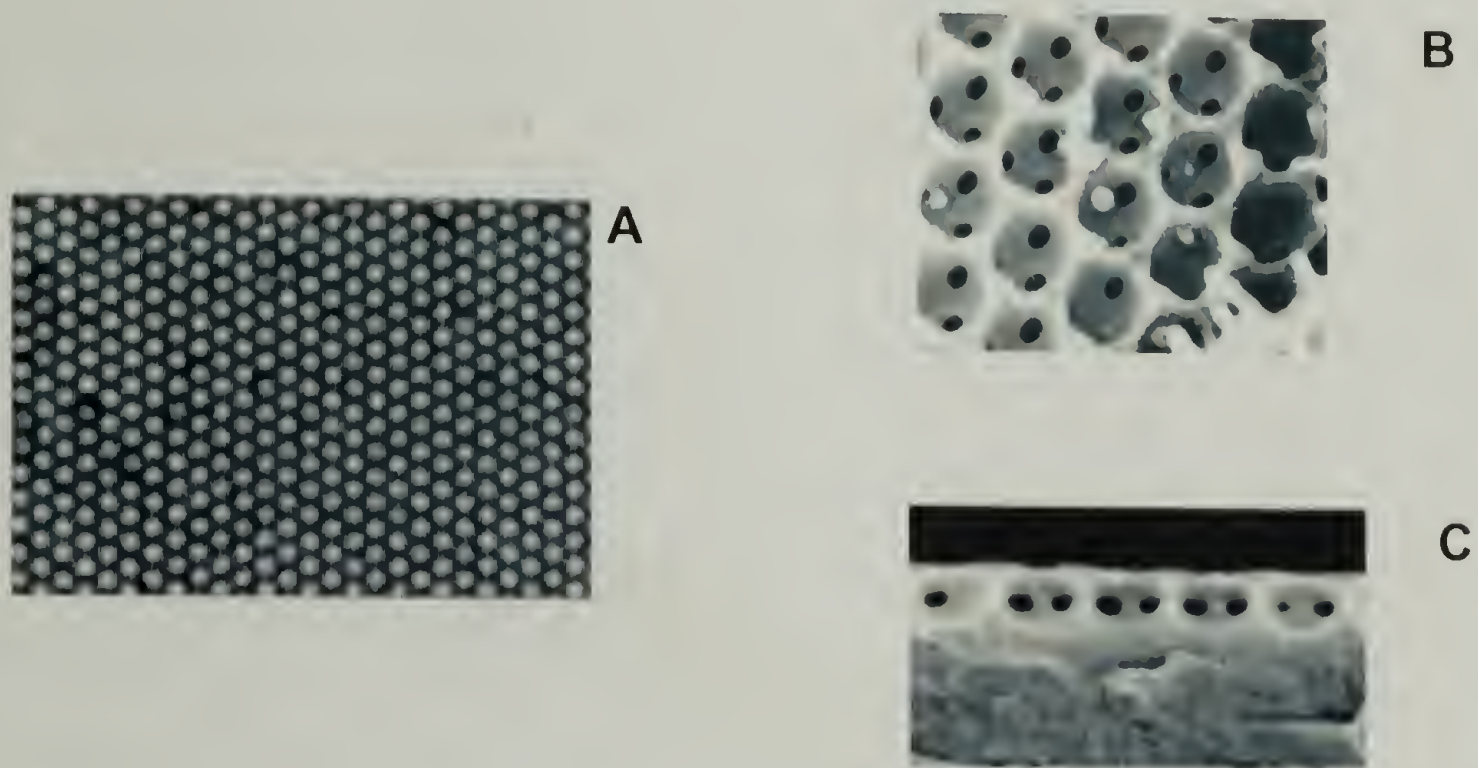


Figure 6. Optical (A) and electron micrographs (B and C) of hydrogels templated with colloidal crystals. Parts A and C show single layer arrays and part B shows multilayer arrays.

Electron microscopy was used to determine the size and geometry of the holes connecting the cavities. Prior to imaging, the hydrogels with embedded arrays were dehydrated by successively soaking the films in 30, 50, 70, 80, and 95 v.% ethanol in water for at least 30 min in each, except for 80% solutions where samples were left for at least 3hrs. This procedure gradually reduces the solvent quality and leads to the

hydrogel shrinkage to approximately 50% of the original linear dimensions. Also, the hydrogel loses its flexible nature and becomes glassy in the solutions with ethanol content above 80%. Then, hydrogel films were dried first on a bench-top and then in vacuum. During drying, no visible changes to the hydrogel were observed. The visual observation also revealed iridescence in the film, suggesting that the structure of cavity arrays was preserved.

The dried polyacrylamide films were freeze fractured under liquid nitrogen. The Petri dish with the films was immersed in liquid nitrogen and the film was lightly pressed with a scalpel blade until the film shattered. The Petri dish with the fractured film covered with liquid nitrogen was dried in a vacuum oven. The drying step requires care not to allow condensation of moisture on the fractured film or melting of ice crystals on the film. Once the film is moisturized, the replicated structure is lost. The dried films were sputter-coated with a gold layer of 15 to 30 nm and imaged with field emission scanning electron microscope (JEOL 6320). The hole size was determined relative to the cavity size and the actual size calculated based on the optical microscopy measurements of cavity sizes. The hole size was averaged over at least one hundred measurements. In many electron micrographs, cavity and hole shapes were oval, as noted in Figure 6B and 4C, a feature which we ascribe to the sample tilt. When the cavities and/or holes had the oval shape, they were sized along their longest dimension. The measurement results are presented in later chapters. It should be pointed out that the high polydispersity found in the hole size may be an overestimate of polydispersity relevant to diffusion experiments. The sizing with electron microscopy gives

polydispersity and sizes averaged over the entire sample while the diffusion studies were conducted in defect free regions of the cavity arrays.

DNA labeling and characterization

DNA samples –pUC19(2.69kbp), pBR322(4.36kbp), M13mp18(7.25kbp), and non-methylated λ -phage DNA(48.5kbp)- as well as restriction enzymes –Xba I and Hind III - were purchased from New England Biolabs. Hind III restriction enzyme was used to linearize pBR322 plasmid and Xba I was used to linearize pUC19 and M13mp18 as well as to cut λ -phage DNA into 24kbp fragments. DNA digestion was carried out according to the enzyme supplier's protocol. The digestion completion was checked with gel electrophoresis.

Digested DNA was purified by phenol-chloroform-isoamyl alcohol extraction and ethanol precipitation following the procedures given in [11]. The purified DNA was re-dissolved in a buffer, targeting concentrations around 10 μ g/ml and assuming 50% yield after purification. The exact DNA concentration was determined with fluorimetry according to [12].

Several buffers - 0.5x Tris-Borate, EDTA (TBE) pH 8.3, 1x Tris-Acetate EDTA (TAE) pH 8.0 and 1x Tris EDTA (TE) pH 7.95 – were tested for suitability in single molecule fluorescence experiments, Figure 7. The fluorescent intensity of λ -DNA labeled with TOTO-1 (Molecular Probes) at 1:6 dye-bp ratios at DNA concentration 100ng/ml was measured. Neat buffers, the buffers with addition of 10mM NaCl, and 5 mM sodium ascorbate (NaAs) were checked for fluorescence quenching. The highest fluorescence intensity was recorded for the TBE buffer followed closely by solutions in

TAE buffer. TE buffer solutions showed noticeably lower fluorescence compared to both TBE and TAE buffers, this difference was especially large for the buffers with additions of both 10mM NaCl and 5mM NaAs, as shown in Figure 7. The solutions in TBE buffer demonstrated the highest fluorescence intensity but only marginally higher than in TAE buffer. The 1x TAE was picked as the medium for single molecule visualization since its ionic strength can be easily determined. In TBE buffer, the composition of ionic species is not easily determined, making estimate of ionic strength more difficult.

DNA was labeled with TOTO-1 dye at 1:6 dye – DNA base pair (bp) ratio according to the protocol provided by the dye supplier, with DNA final concentration being 30ng/ml. Labeled DNA solutions were protected from light and left to equilibrate for at least two hours prior to experiment. The solutions of λ -DNA fragments were additionally incubated at 80°C for 3min to attain separation of the DNA ends.

It is known that the diazocyanine dyes of the TOTO family can lead to the degradation of DNA under illumination.[13] Care was taken throughout the experimental procedure to minimize the DNA – dye complex exposure to light. The microscope was equipped with red filters on an optical illumination block which prevents the labeled DNA degradation while positioning and observing the arrays in optical microscope. The fluorescence observations were done at the minimum illumination required to produce acceptable picture quality.

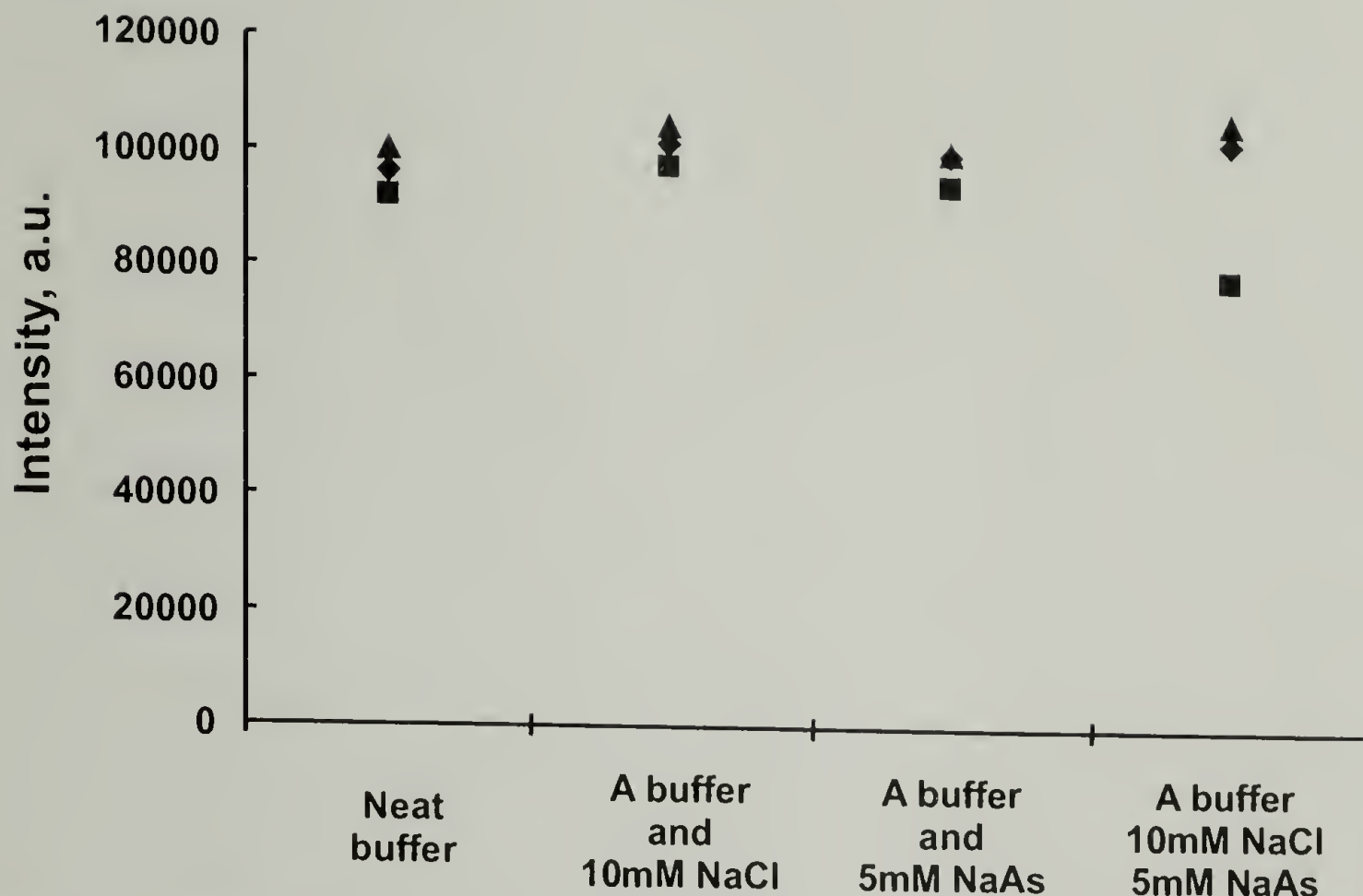


Figure 7. Fluorescence intensity of TOTO-1 labeled λ -DNA in buffers of different compositions. Triangles corresponds to 0.5x TBE based buffers, diamonds corresponds to 1x TAE based buffers, and squares corresponds to 1x TE based buffers.

β -Mercaptoethanol is routinely used for reduction of both fluorescence quenching and DNA degradation under illumination in single molecule visualization experiments.[13, 14] We found the compound to be unsuitable for the DNA diffusion study. The diffusion measurements were not reproducible at 2% concentration of β -mercaptoethanol, the most common concentration used for DNA imaging. Electrophoretic measurements of DNA mobility in agarose gel in the presence and absence of the β -mercaptoethanol confirmed that β -mercaptoethanol affects DNA mobility. Instead of β -mercaptoethanol, we used sodium ascorbate as a radical scavenger as proposed in [15]. Sodium ascorbate was added to all buffering solutions at 5 mM final concentration within half an hour of a diffusion experiment, and nitrogen

was bubbled for 10 minutes through the buffer to reduce the oxygen content in the solutions.

Visualization of Diffusion

It is entropically unfavorable for DNA molecules to enter from solution into the produced array of pores. We used an electrical field to draw the molecules inside the array. The assembly consisted of platinum wire electrodes embedded in ~1% agarose gel slabs which sandwiched the hydrogel film with embedded array of holes and DNA solution, Figure 8.

An electric field of about 10 V/cm applied for several seconds was enough to achieve good filling of the array with the DNA molecules without multiple occupancies of a single cavity. The best results were obtained when electrodes were parallel to each other and located right above and below the areas to be filled with DNA molecules. Immediately after the electric field was turned off, the hydrogel film side with the embedded array was covered with silicon oil (Silicon oil 1100, Aldrich). The time interval between the moment when electric field was turned off and the surface was sealed with the silicon oil was crucial. When the interval was too short, the arrays were overfilled with DNA, when the interval was too long the majority of DNA escaped the cavities before array was sealed. The latter case was more common than the former, thus as fast as possible sealing of the arrays is recommended. If excess of buffer was observed between hydrogel and silicon oil, the buffer was carefully removed with filter paper. The film was tightly pressed onto a cover slip hydrophobized with Sigmacote and covered with a few droplets of the silicon oil. The oil was used

sparingly, which helped not only to seal the surface of the array but also to prevent the evaporation of water from the hydrogel and oxygen transport from the atmosphere into the diffusion media.

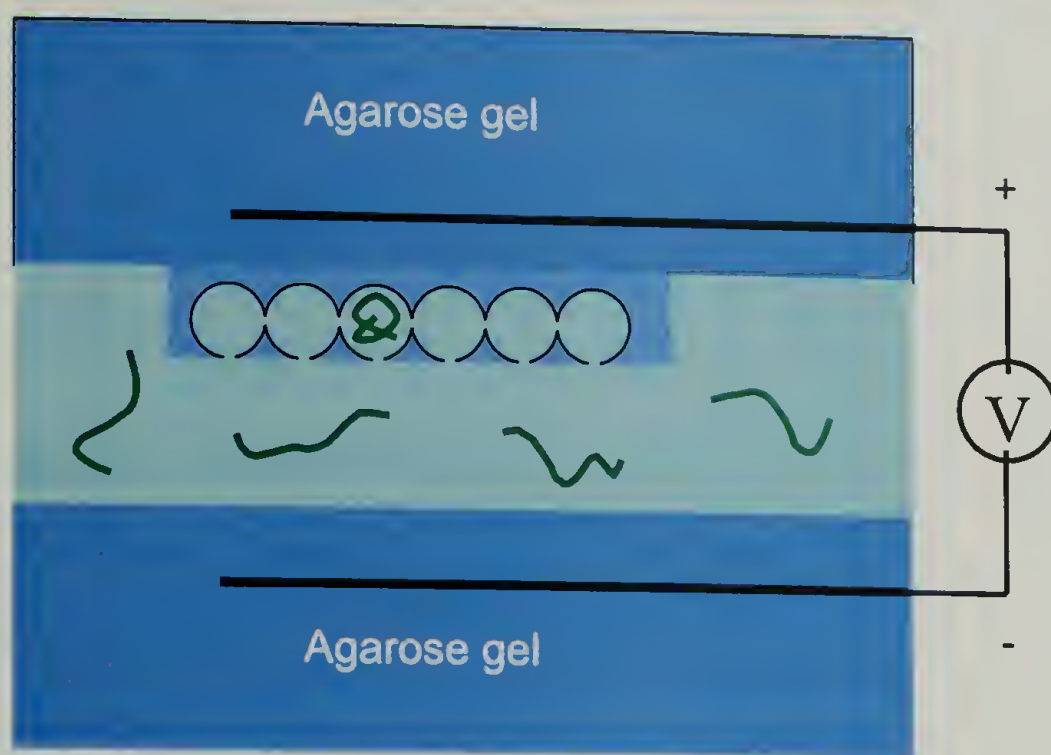


Figure 8. Schematic of the assembly used to fill the spherical cavity arrays with DNA molecules.

Mounted on the microscope stage, the assembly was left for approximately 15 minutes to equilibrate in temperature and position. The Brownian motion of DNA was studied with a Zeiss Axovert S100TV fluorescent microscope equipped with 63x, oil, phase contrast objective. The fluorescent images were recorded with a SensiCam QE (Cooke) CCD camera at 2x2 binning. The acquisition rate was varied from 0.5 to 7 frames per second and typically 501 frames taken for a single viewing area. The frame rate was adjusted to get maximum statistical information on molecule movement without loss of finer details of the dynamics. Before and after acquiring the sequence of

fluorescent images, optical images of the arrays were taken. Image analysis was carried out with IPLab software package (Scanalytics).

References

1. Denkov, N.D., et al., *Langmuir*, 1992. **8**(12): p. 3183-3190.
2. Jiang, P., et al., *Chem. Mater.*, 1999. **11**(8): p. 2132-2140.
3. Dimitrov, A.S., et al., *Langmuir*, 1994. **10**(2): p. 432-440.
4. Velikov, K.P., et al., *Science*, 2002. **296**(5565): p. 106-109.
5. Braun, P.V., et al., *Adv. Mater.*, 2001. **13**(10): p. 721-724.
6. Bartlett, P., R.H. Ottewill, and P.N. Pusey, *Physical Review Letters*, 1992. **68**(25): p. 3801-3804.
7. Kiely, C.J., et al., *Nature*, 1998. **396**(6710): p. 444-446.
8. Jiang, P., J.F. Bertone, and V.L. Colvin, *Science*, 2001. **291**(5503): p. 453-457.
9. Jiang, P., et al., *J. Am. Chem. Soc.*, 1999. **121**(50): p. 11630-11637.
10. Park, S.H. and Y. Xia, *Chem. Mater.*, 1998. **10**(7): p. 1745-1747.
11. Sambrook, J. and D.W. Russell, *Molecular cloning : a laboratory manual*. 3rd ed. 2001, Cold Spring Harbor, N.Y.: Cold Spring Harbor Laboratory Press. 3 v.
12. Rye, H.S., et al., *Anal. Biochem.*, 1993. **208**: p. 144-150.
13. Ekerman, B. and E. Tuite, *Nucleic Acids Res.*, 1996. **24**(4): p. 1080-1090.

14. Gurrieri, S., et al., *Anal. Biochem.*, 1997. **249**(1): p. 44-53.
15. Maier, B. and J.O. Rädler, *Macromolecules*, 2000. **33**(19): p. 7185-7194.

CHAPTER 3

VISUALIZATION OF DNA DIFFUSION UNDER PERIODIC CONFINEMENT

Diffusion Mechanism

Under incessant Brownian motion, mobile macromolecules in gels, membranes, or cytoplasm constantly squeeze through and around obstructions of molecular size. Until recently, neither the surroundings nor the motion of a single molecule could be directly observed, and the understanding of such sterically constrained motions was principally deduced through examination of the macroscopic diffusion coefficient. The dynamics of a single, large macromolecule can now be visually monitored by fluorescence microscopy [1-4], but studies of macromolecular diffusion by this approach have not extended to environments providing well-defined spatial constraints. We describe the observation of macromolecular motion in highly ordered media of controlled geometry and chemistry.[5]

By infusion and subsequent polymerization of liquid monomer, colloidal templating replicates in a polymeric solid the structure of a precursor colloidal array[6-8]. The details on the array preparation and its use as a diffusion media with monodisperse holes are given in Chapter 2. For this study, the precursor array consists of nearly monodisperse polystyrene spheres (895 nm diameter) resulting in the array of 920 nm cavities interconnected with 200 nm holes.

Figure 9A superimposes transmission and fluorescence still frames of four neighboring 7.25 kbp DNA fragments of contour length $3.4 \mu\text{m}$ and equilibrium (unconfined) radius of gyration $0.26 \mu\text{m}$. Figure 9B overlays 500 subsequent

exposures of 0.5 s; over the 250 s time period, molecules variously moved through 8 to 14 cavities. A closer look at the path followed by one molecule is provided in Figure 9C. As suggested by the figure and easily discerned in the associated movie, diffusion occurs via discrete jumps from cavity to cavity, with rapid jumps (<1 second) separated by long periods (18 seconds average) over which molecules remain essentially stationary. Even with centers-of-mass localized inside single cavities, small chain sections continuously probe neighboring cavities. Details of the probing are hard to resolve, but growth of a probing fluctuation beyond a threshold extension likely leads to abrupt jump of an entire molecule. Molecules are rarely observed to straddle adjacent cavities, and when they do, they slip into one of the cavities before the next frame. The color code and jumping times attached to Figure 9C reveal how the highlighted molecule jumped through the array. Extended illumination in the microscope causes a small fraction of molecules to degrade, and this fraction, along with any molecules that approached lattice defects, are discarded from subsequent analysis.

Movies were obtained for five DNA samples with lengths from 2.69 to 48.5 kbp. For lengths less than about 24 kbp, jump dynamics are similar to those of Figure 9. Molecules smaller than 2 kbp are difficult to identify against the background, while those larger than 24 kbp behave differently. The entropic barriers transport mechanism accounts for the jump dynamics observed across the range 2.69 to 24 kbp, corresponding to macromolecular radii of gyration from 0.1 to 0.3 μm (assuming ideal DNA chain conformations, the real dimensions, when excluded volume effect is taken into account, are expected to be somewhat bigger, from 0.1 to 0.38 μm , see Chapter 6). These radii are greater than the hole radius, and with the radius of gyration recognized

as a small measure of coil size, the molecules can be viewed as squeezing through the holes. According to the entropic barriers transport mechanism [9, 10], molecular configurations spanning two cavities define a transition state possessing a higher free energy than a chain occupying a single cavity. The higher free energy corresponds to a reduced number of configurations, i.e. lower configurational entropy, for a flexible chain “pinched” along its length.

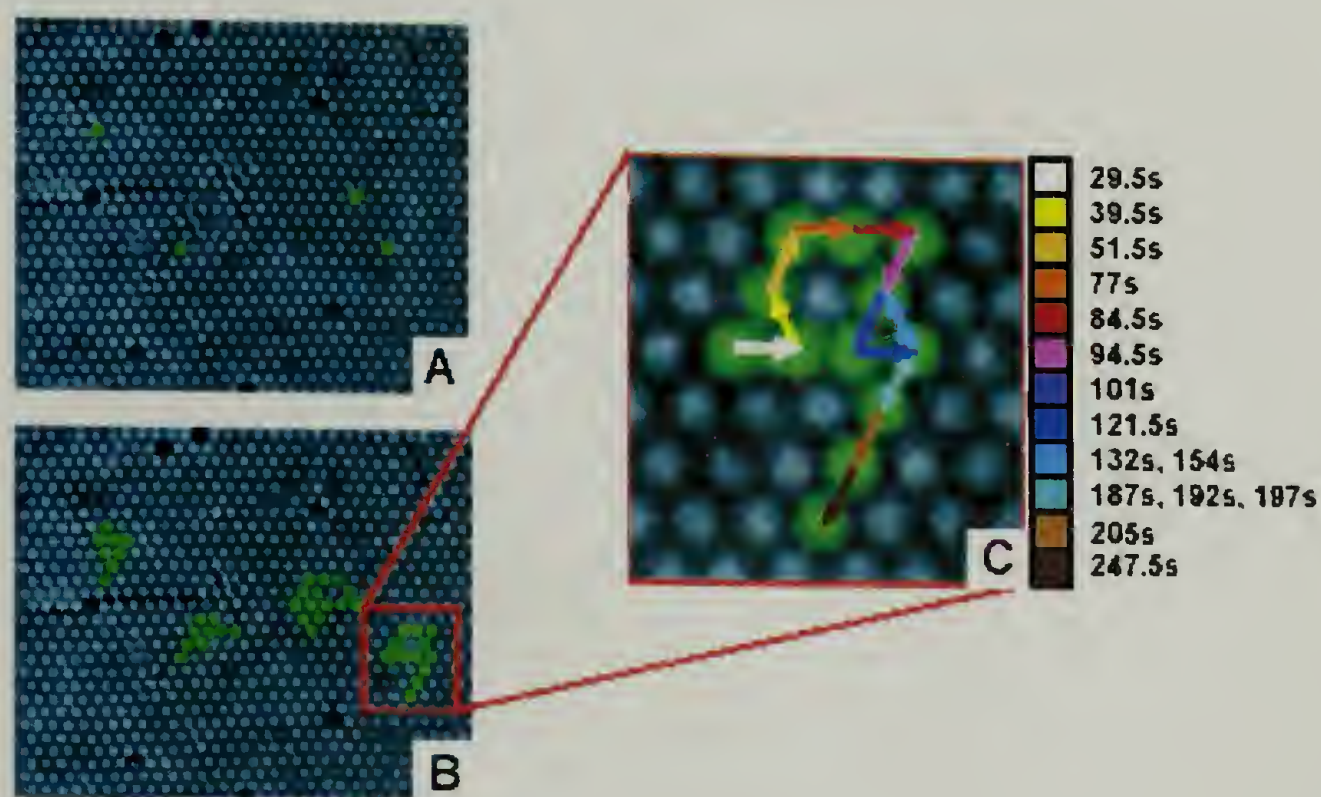


Figure 9. Visualization of 7.25 kbp DNA trajectories. (A) Still frame displaying four DNA molecules trapped inside single cavities. (B) Overlay of 500 consecutive frames of the same molecules. (C) Expanded image of the path taken by one molecule. The color code provides the times along this path at which the molecule jumped between cavities.

Figure 10 displays a series of unequally timed images of 48.5 kbp DNA, the largest of this study. The equilibrium radius of gyration and contour length are 0.58 and 22 μm , respectively (see Chapter 6).[11] Fully stretched, this molecule would span more than 20 cavities, seemingly enough to define a reptation tube. Indeed, some

aspects of reptation are noted in this molecule's motion. Nevertheless most aspects of the motion differ markedly from classic reptation. With a fluctuating number of cavities occupied, motion is more akin to the bunching and stretching of an inchworm. In contrast to the smaller DNA molecules, diffusion can no longer be interpreted in terms of discrete cavity-to-cavity jumps. Although localization to a single cavity still occurs, the dominant configuration is occupation of two adjacent cavities. The figure shows a variety of three and four cavity configurations that are both bent and straight.

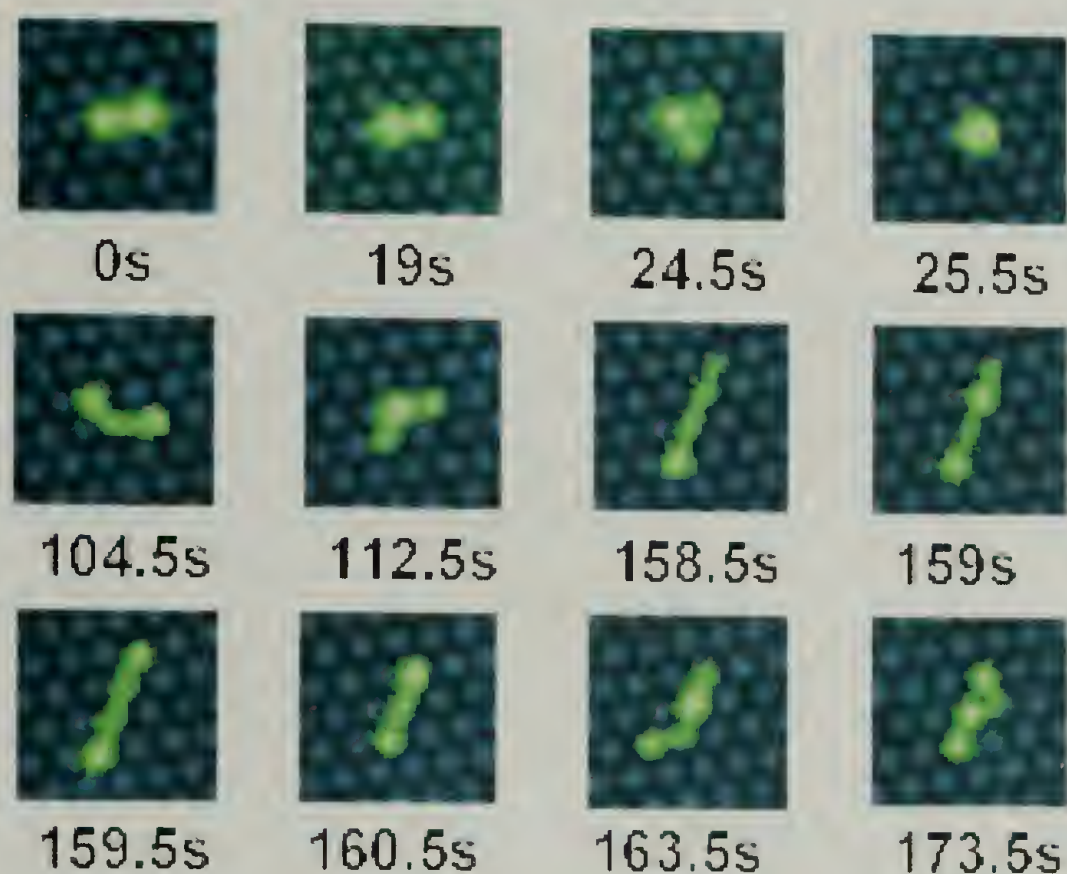


Figure 10. A sampling at various times of configurations observed for a single 48.5 kbp DNA. The diffusing molecule has been re-centered in each image.

Interestingly, linear molecules spanning three or four cavities were not observed to form new configurations through “hernias” that spill out laterally from central cavities. Instead, the molecules dominantly alter configuration by expanding or

contracting from the cavities that appear to host end segments. The persistence length of DNA is about 50 nm, so hernias would be expected to form readily in the interconnecting holes [12]. We tentatively ascribe the dynamics for this largest DNA to the beginnings of a crossover from entropic barriers transport to reptation.

Hopping Frequency Distribution

Ideally, a molecule equilibrated inside a single cavity should jump randomly in time and direction to one of six neighboring cavities. Such uncorrelated jumps follow Poisson time statistics [13], an expectation checked by plotting histograms of $P(n)$, the probability that n jumps are taken in time interval τ . With τ adjusted to equalize approximately the average number of jumps, Figure 11 compares measured histograms to Poisson distributions. Excellent agreement is found between measured and predicted values of $P(n)$. A single parameter, the average jumping frequency Γ , characterizes a Poisson distribution. As molecular size grows from 2.69 to 24 kbp, Γ decreases from 0.187 ± 0.021 to $0.017 \pm 0.002 \text{ s}^{-1}$, corresponding to an average interval between jumps of several seconds to several tens of seconds. As expected, larger molecules move more sluggishly. Error is estimated from the fitting Poisson distribution and taken as plus/minus three standard deviations of the fitting parameter Γ .

Sometimes jumping frequencies higher than allowed by Poisson distribution are observed. Such frequent jumps we attribute to molecules that were degraded by light. Usually, the degraded molecules can be unambiguously discerned as having low fluorescent intensity and are discarded from the data set prior to quantitative analysis. In rare instances, the degraded molecules are hard to identify solely based on the

intensity. In this case, jumping probability was plotted for τ equal the length of entire movie and compared with Poisson distributions of equal mean. The molecules which jumping frequency had probability less than $1 \cdot 10^{-5}$ according to theoretical Poisson distribution were discarded from the analysis. This procedure did not change the mean jumping frequency by more than several per cent, but improved the fitting of the experimental data to Poisson distribution.

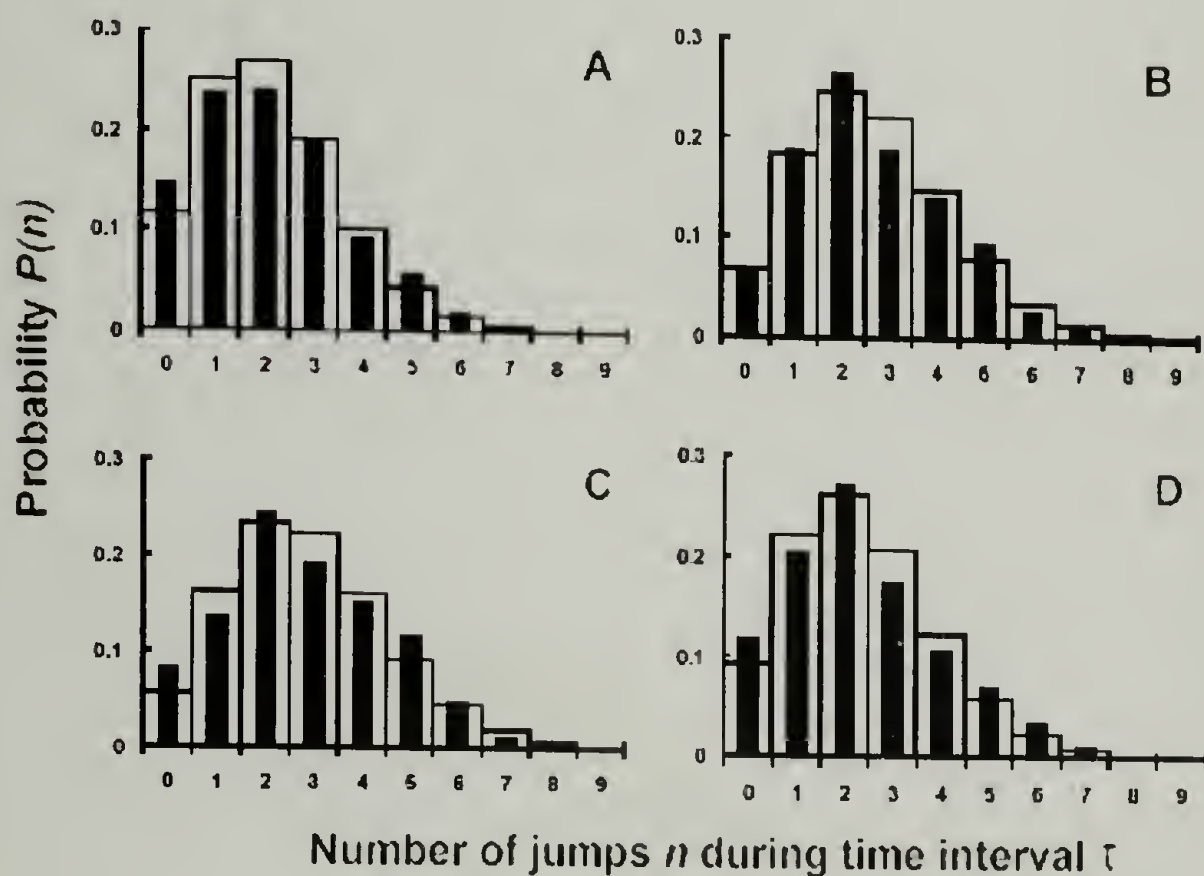


Figure 11. Measured values of $P(n)$ (plotted as solid bars) compared to Poisson distributions (plotted as open bars) with identical means. (A) 24.3 kbp ($R_g=0.38$ nm), $\tau=125$ s, $\Gamma=0.017$ s $^{-1}$. (B) 7.25 kbp ($R_g=0.19$ nm), $\tau=50$ s, $\Gamma=0.053$ s $^{-1}$. (C) 4.36 kbp ($R_g=0.14$ nm), $\tau=25$ s, $\Gamma=0.115$ s $^{-1}$. (D) 2.69 kbp ($R_g=0.10$ nm), $\tau=12.5$ s, $\Gamma=0.187$ s $^{-1}$.

Jumping Direction Distribution

To follow the jumping direction distribution, we indexed the direction of molecular jumping relative to the direction of the previous jump. Figure 12 depicts the way jumping direction was monitored for the molecule jumping from the central cavity

in the figure. Zero direction represents the cavity from which the molecule initially entered the central cavity. Starting from cavity zero, all other cavities are indexed from 1 to 5 clockwise. Practically, the movement in “zero” direction will mean back and forth jumping between two cavities. And, for example, movement in “three” direction represents the molecular jumping in a straight line. The use of relative direction indexing versus absolute direction indexing is dictated by the absence of a single direction that can be unambiguously assigned to the whole array.

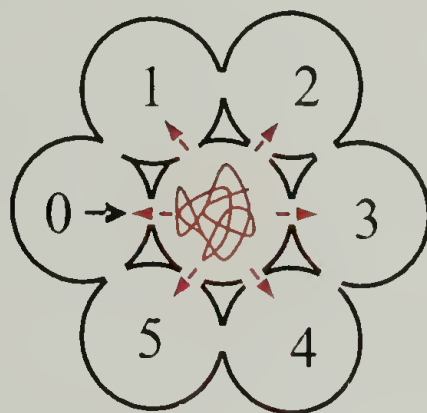


Figure 12. Schematic of hopping direction indexing

Using the relative direction indexing, histograms of jumping direction distribution were created, as illustrated in Figure 13. Unexpectedly, histograms of jump direction are not fully in accord with random jumping, as molecules exit cavities preferentially in the forward direction, i.e., through the hole opposite to the one by which they entered, and in the backward direction, i.e., through the same hole by which they entered. The forward bias weakens as time spent in a cavity increases, revealed in Figure 13B. This time dependence suggests that some molecules jump before becoming

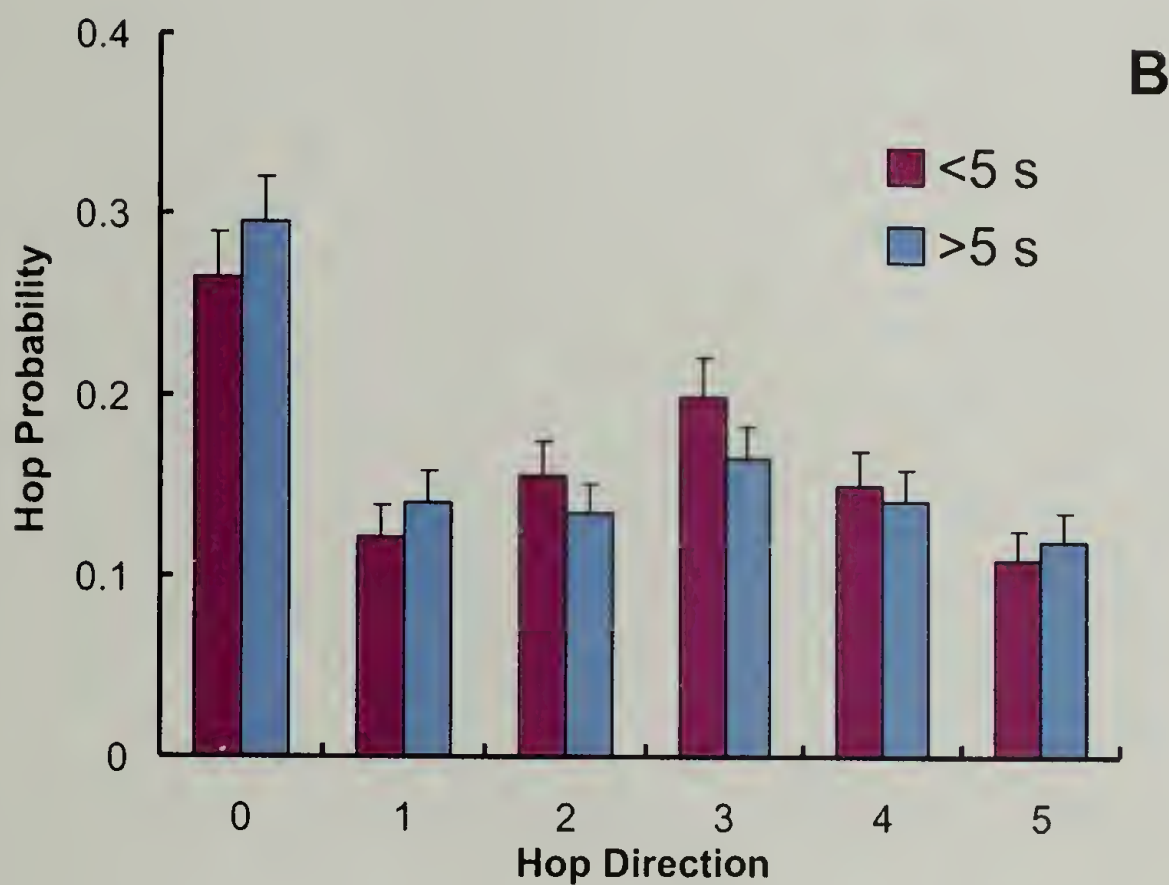
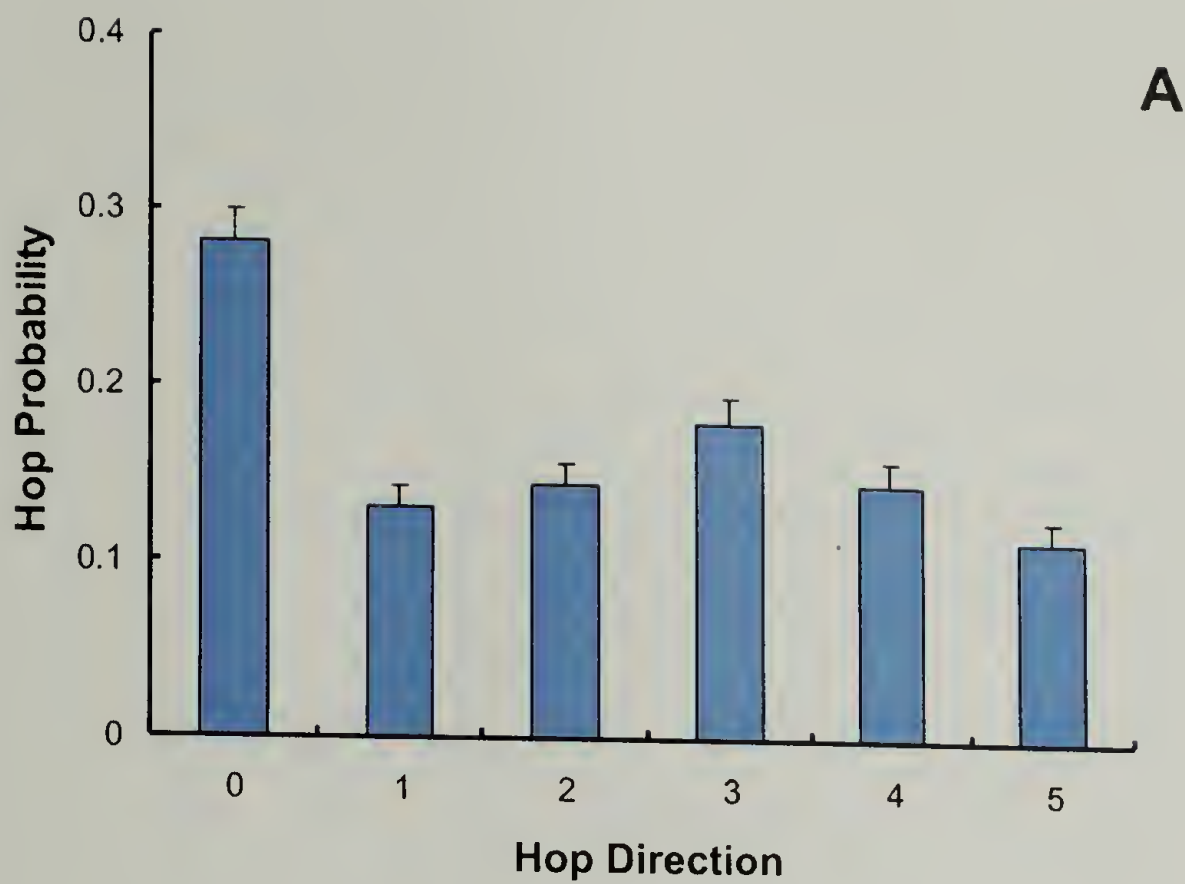


Figure 13. The histograms of hopping direction distribution measured for 4.69kbp DNA molecules in 920 nm cavity arrays. Part **A** shows the hopping direction distribution irrespective to the time molecule spends in a cavity before a hop. Part **B** presents the hopping direction distribution for hops occurred when molecules spend less than 5 seconds in a cavity before the hop (red bars), and for hops when molecules spend more than 5 seconds in a cavity before the hop (blue bars).

fully equilibrated and that partial memory of the deformation undertaken to enter a cavity forward biases the direction of exiting. The backward bias, on the other hand, seems independent of time spent in a cavity. This bias is believed to manifest hole polydispersity; DNA molecules are expected to jump more frequently backward and forward between cavities bridged by a larger than average hole. To investigate the possibility, the hole diameter distribution was determined by freeze-fracture scanning electron microscopy, and a standard deviation of 40 nm was found. Such breadth is consistent with the measured backward bias. Because both biases of jump direction are small, neglecting directional bias in the diffusion analysis is inconsequential.

Microscopic vs. Macroscopic Diffusion Coefficient

Einstein [14, 15] first derived the relationship between the diffusion coefficient D and random molecular displacements of average magnitude a . Extrapolated to two dimensions, his theory predicts

$$D = \frac{a^2\Gamma}{4} \quad (7)$$

Equating a to the cavity diameter and substituting Γ measured for 4.36 kbp DNA, this formula predicts that D equals 2.45×10^{-10} cm²/s, representing the microscopic prediction of D . After a large number of jumps, he showed that the mean-square-position displacement $\langle r^2 \rangle$ depends linearly on time interval t , where in two-dimensions,

$$D = \frac{1}{4} \frac{d\langle r^2 \rangle}{dt} \quad (8)$$

For 4.36 kbp DNA, Figure 14A plots $\log\langle r^2 \rangle$ vs. $\log t$, and as expected, data are well fit by a line of slope equal to unity. The line's intercept reveals that D equals

$2.3 \times 10^{-10} \text{ cm}^2/\text{s}$, representing the macroscopic prediction of D . The microscopic and macroscopic values for D are essentially identical. In the absence of confinement, D for the same DNA is $1.94 \times 10^{-8} \text{ cm}^2/\text{s}$, approximately two orders-of-magnitude larger than in the array [11]. Confinement produces both hydrodynamic and configurational interactions that reduce D , but hydrodynamic interactions play a much smaller role [2, 16].

Visualizations of molecular motion, combined with Poisson jump statistics, verify the dominance of entropic barriers transport for the sizes less than 24 kbp. These statistics also provide D as a function of M , as plotted in Figure 14B. The data in the figure reasonably conform to scaling theories [9, 17] for entropic barriers transport that argue for an approximately exponential dependence of D on M . The constrained diffusion literature more frequently correlates this dependence through a power-law, $D \propto M^{-\nu}$. Forcing the power-law form, a satisfactory fit is obtained with $\nu = 1.1 \pm 0.07$. In typical diffusion studies, i.e. those without visualizations, ν so close to unity would be interpreted as evidence for nearly unconstrained (Rouse) diffusion of freely drained DNA molecules [2, 16]. Visualizations unambiguously demonstrate the error of this interpretation. The ability of different functions to correlate D reflects the limited span of M and the freedom in choice of fitting parameters. Only through visualization can the correct diffusion mechanism in the arrays be identified.

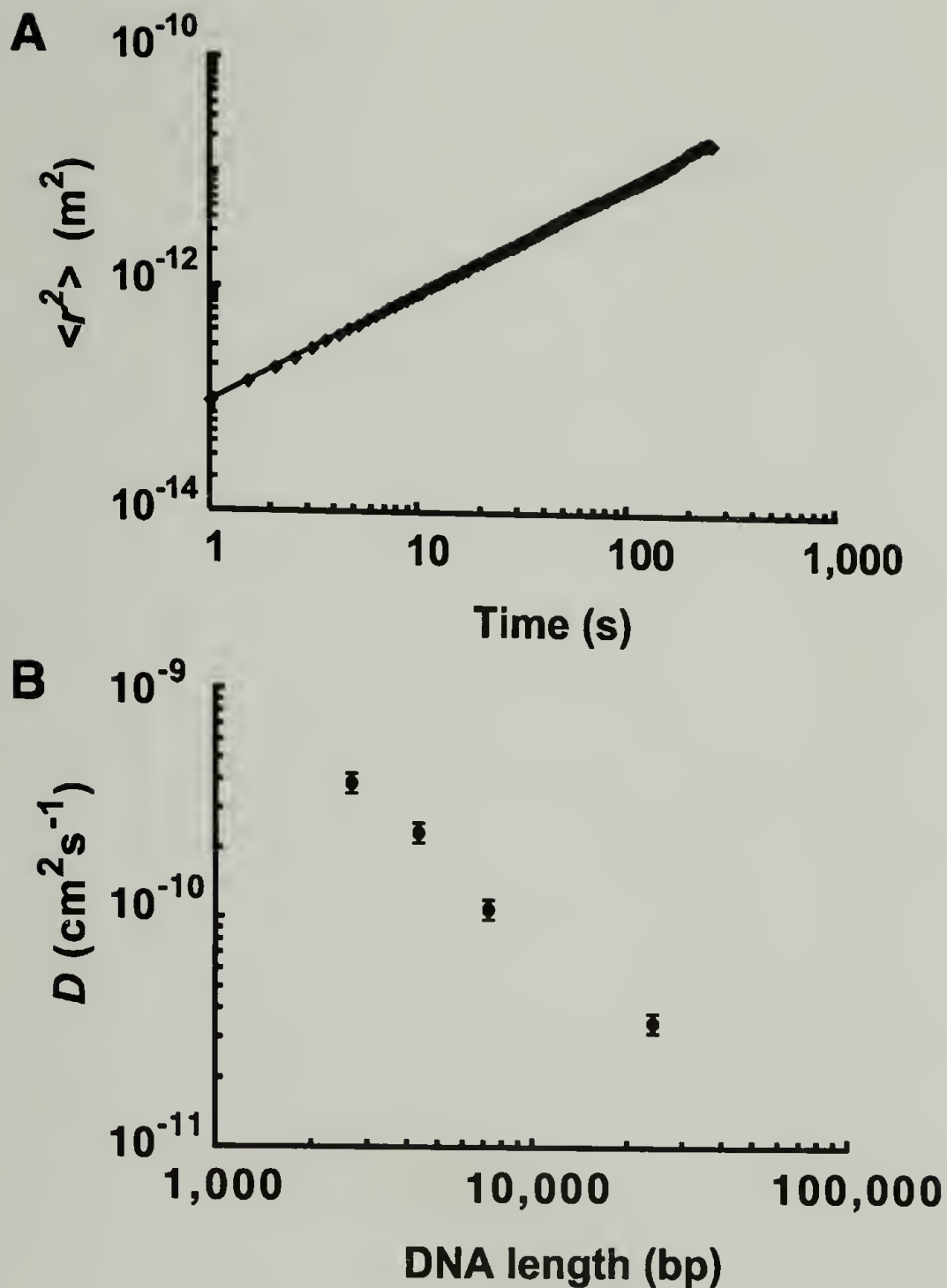


Figure 14 DNA diffusion analysis. (A) The linearity of the mean square displacement as a function of time for 4.36 kbp DNA reveals diffusive transport, with the molecule's diffusion coefficient given by the intercept. (B) Variation of diffusion coefficient with molecular weight when the observed mode of diffusion is jumping from cavity to cavity.

Macromolecular diffusion in constrained environments has significant technological and scientific ramifications. Most macromolecular separation techniques rely on the selective penetration and/or diffusion of macromolecules within gels and other media of ill-defined pore structure. In this context, switching from disordered to

patterned media promises to improve both speed and resolution [18-21]. Success as a separation medium hinges on the proper choice of pattern chemistry, feature size, dielectric mismatch, and surface charge. Weighed against its most prominent competitor, lithography, one can identify several advantages for colloidal templating: broad choice of pattern chemistry, reduced dielectric mismatch, and straightforward elimination of surface charge. On the other hand, the number of pattern geometries possible through colloidal templating remains limited [22].

References

1. Perkins, T.T., D.E. Smith, and S. Chu, *Science*, 1994. **264**: p. 819-822.
2. Matsumoto, M., et al., *J. Polym. Sci.: Part B: Polym. Phys.*, 1992. **30**: p. 779-783.
3. Käs, J., H. Strey, and E. Sackmann, *Nature*, 1994. **368**: p. 226-229.
4. Houseal, T.W., et al., *Biophys. J.*, 1989. **56**: p. 507-516.
5. Nykypanchuk, D., H.H. Strey, and D.A. Hoagland, *Science*, 2002. **297**(5583): p. 987-990.
6. Park, S.H. and Y. Xia, *Chem. Mater.*, 1998. **10**(7): p. 1745-1747.
7. Jiang, P., et al., *J. Am. Chem. Soc.*, 1999. **121**(50): p. 11630-11637.
8. Liu, L., P. Li, and S.A. Asher, *Nature*, 1999. **397**(6715): p. 141-144.
9. Muthukumar, M. and A. Baumgärtner, *Macromolecules*, 1989. **22**(4): p. 1937-1941.

10. Muthukumar, M. and A. Baumgärtner, *Macromolecules*, 1989. **22**(4): p. 1941-1946.
11. Smith, D.E., T.T. Perkins, and S. Chu, *Macromolecules*, 1996. **29**(4): p. 1372-1373.
12. Åkerman, B., *Phys. Rev. E*, 1996. **54**: p. 6686-6696.
13. Haus, J.W. and K.W. Kehr, *Phys. Rep.*, 1987. **150**: p. 263-406.
14. Einstein, A., *Ann. Phys.*, 1905. **17**: p. 549-560.
15. Einstein, A., *Z. Electrochem. Angew. Phys. Chem.*, 1908. **14**: p. 235-239.
16. Gennes, P.-G.d., *Scaling Concepts in Polymer Physics*. 1979, Ithaca and London: Cornell Univ. Press. 193-197.
17. Guillot, G., L. Läger, and F. Rondelez, *Macromolecules*, 1985. **18**(12): p. 2531-2537.
18. Volkmuth, W.D. and R.H. Austin, *Nature*, 1992. **358**: p. 600-602.
19. Han, J., S.W. Turner, and H.G. Craighead, *Physical Review Letters*, 1999. **83**(8): p. 1688-1691.
20. Chou, C.-F., et al., *PNAS*, 1999. **96**(24): p. 13762-13765.
21. Meistermann, L. and B. Tinland, *Phys. Rev. E*, 2000. **52**(3): p. 4014-4017.
22. Velikov, K.P., et al., *Science*, 2002. **296**(5565): p. 106-109.

CHAPTER 4

DIFFUSION OF A LINEAR DNA IN AN ARRAY OF SPHERICAL CAVITIES

Effect of Molecular Weight

We have measured the diffusion coefficient D of DNA molecules ranging in size from 2 kbp to 24 kbp in arrays with various cavity sizes and the results are summarized in Figure 15. In literature, the most common way to analyze polymer diffusion is to follow how the diffusion coefficient scales with molecular weight.[1, 2] Based on the observed scaling exponent, a judgment is usually made for the diffusion mechanism operative in that system. One can immediately see, from Figure 15, that diffusion in the array of spherical cavities cannot generally be described via a simple single exponent power law. In 1400 nm arrays, D can be fitted with a power law of $M^{-1.5}$, which would normally be taken as an indication of motion intermediate between free diffusion and reptation. In 920 nm arrays, the power law decreases to $M^{-1.1}$, which indicates Rouse dynamics or basically free diffusion with screened hydrodynamic interactions.

Molecular visualization of motion, on the other hand, clearly shows that diffusion is not free, lacking features of reptation, but rather resembling activated hopping. In 608 nm arrays, D shows a completely different behavior, as a power law does not fit data at all; for DNA sizes ranging from 2 kbp to 7 kbp D in 620 nm arrays decreases quite rapidly from $6.4 \cdot 10^{-10}$ to $1.8 \cdot 10^{-10} \text{ cm}^2/\text{s}$, while for longer DNA molecules, from 7 to 24 kbp, the decrease is only from $1.8 \cdot 10^{-10}$ to $1.5 \cdot 10^{-10} \text{ cm}^2/\text{s}$; D is practically independent of M in the latter range. Such independence of D on M may manifest itself unconventionally in an increasing electrophoretic mobility for longer molecules.

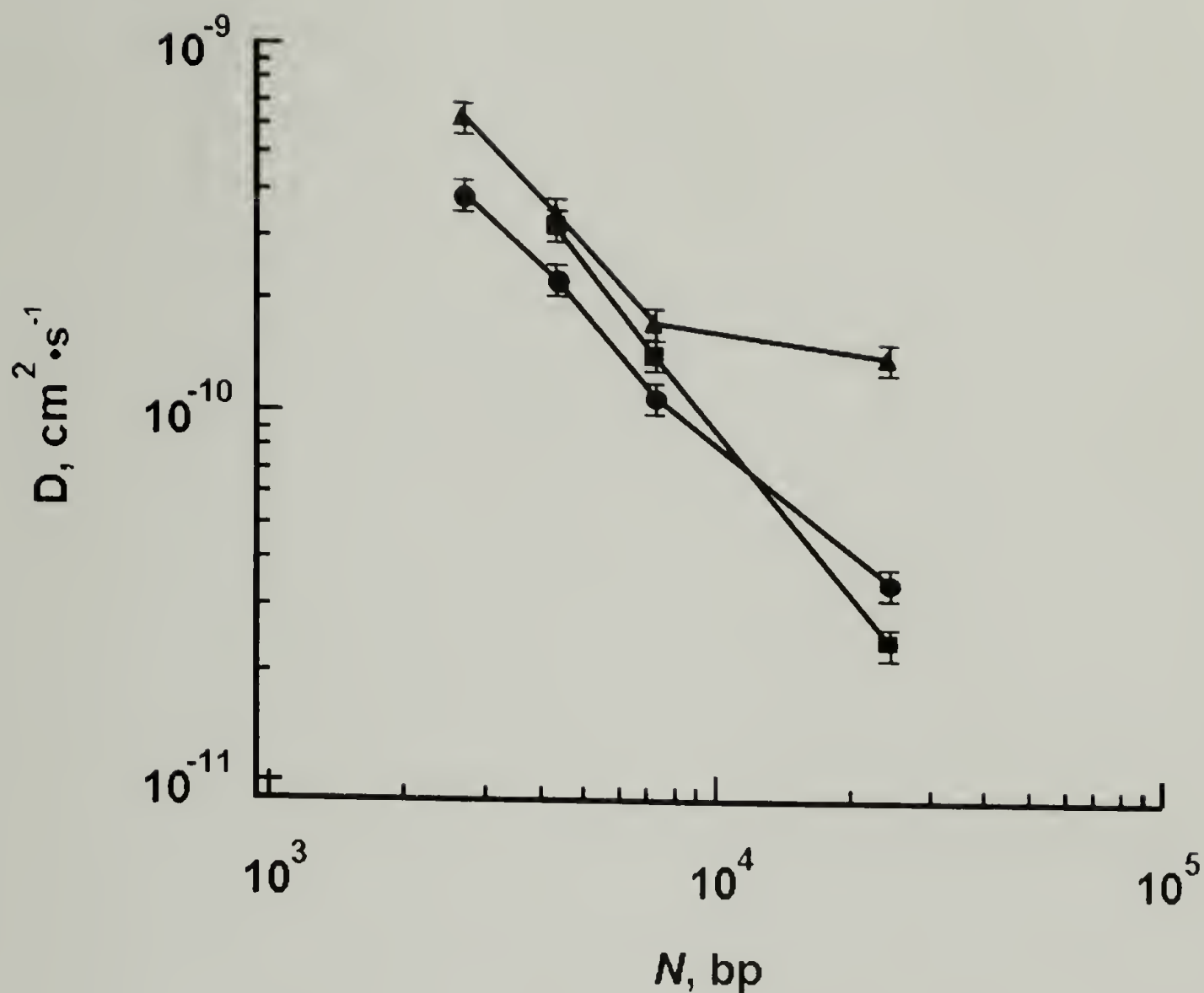


Figure 15. Variation of diffusion coefficient with size of DNA molecules. Triangles, circles, and squares represent diffusion coefficients in arrays with 608, 920, and 1400 nm cavities, respectively.

As was discussed in Chapter 3, the visualization of diffusion in the spherical cavity arrays reveals diffusion by an entropic barrier mechanism. Diffusion in the presence of an energy barrier can be described by a general equation (2). For submicron pores, D_0 in this equation should be substituted by D_c - the rate of polymer diffusion inside the cavity in the absence of an energy barrier. Due to confinement induced screening of hydrodynamic interactions between chain segments and appearance of hydrodynamic interactions between chain segment and cavity walls, D_c is not necessarily equal to the polymer diffusion coefficient in free solution, D_0 . In confined spaces, diffusing macromolecules experience the full or partial screening of

intramolecular (segment-segment) hydrodynamic interactions, an effect which changes the character of diffusion compared to a bulk solution.[3, 4] Change of hydrodynamic interactions is generally hard to take into account quantitatively in the presence of fixed boundaries. Qualitatively, compared to unconfined spaces, pore boundaries hinder diffusion by a factor of order of unity. For all our experiments, diffusion is hindered by 1-2 orders of magnitude, suggesting that hydrodynamics is important, but is not dominating factor. The screening of hydrodynamic interactions by pore boundaries manifests itself in an increase of the scaling exponent of D . With full screening, D is proportional to the length of polymer chain – the polymer behaves as a free draining coil. Since in a free solution D is proportional to $N^{0.65}$, [5] D_c becomes proportional to N^n , where n is anywhere between -0.65 and -1, depending on the degree of screening of the hydrodynamic interactions in the experiments. Although, the exact value of D_c is not known, it can be related to D_0 as $D_c = m_1 N^{(n-0.65)} D_0$, where m_1 is a proportionality coefficient that takes into account the diffusion slowdown due to hydrodynamic interactions. The change of the cavity size and geometry changes m_1 .

Thus, equation (2) can be rewritten as follows,

$$D = m m_1 N^{(n-0.65)} D_0 \exp(-\Delta F), \quad (9)$$

where ΔF is the energy barrier height, and m is a proportionality coefficient which takes into account geometric effects. When enthalpic interactions are constant irrespective of the molecule position within the diffusion media, the energy barrier ΔF reflects only

changes in the configurational entropy that chain experiences in the various locations inside the media, which is the case for our system.

By plotting the reduced diffusion coefficient D/D_0 versus DNA size we can assess the effect of N on the entropic barrier height, as revealed in Figure 16A, when hydrodynamics effects due to confinement are not important and are not screened. $D/(D_0N^{0.35})$ against N serves the same information but for the case when the intramolecular hydrodynamic interactions are completely screened, shown in Figure 16B. Our experimental conditions are between these two extremes. We expect the segment-segment hydrodynamic interactions to be at least partially screened. This screening can be different for each set of array sizes, and if so, greater screening is anticipated for the smaller cavity arrays. Segment-pore boundary hydrodynamic interactions if anything will increase in the smaller cavities. The data in Figure 16 gives us the trend in ΔF with N , but not a quantitative measure of ΔF . A better understanding of hydrodynamics for diffusing polymer chains in confined spaces is necessary for quantitative assessment of the entropic barrier from diffusion data.

In the 920 nm array, the diffusive behavior of DNA molecules is in accord with the screening of intramolecular hydrodynamic interactions as the reduced diffusion coefficient scales as $N^{0.4}$. This value is very close to what one would expect for a free draining coil, which indicates the energy barrier for diffusion has a very weak dependence on N .

In the arrays with 1400 nm cavities, the reduced diffusion coefficient falls off faster with N than one would expect from screening of the hydrodynamic interactions,

suggesting a steeper dependence of energy barrier on the polymer size for diffusion in the biggest cavities.

The diffusion character in the 620 nm arrays is more complicated. For N below 7 kbp, the diffusion behavior is similar to that in the 920 nm arrays – weak dependence of energy barrier (increase) on polymer size. For N from 7 kbp to 24.3 kbp, the energy barrier decreases for the larger molecules.

Thus, there are three distinct regimes of diffusion depending on the relative sizes of the DNA molecules and the cavity. Behavior changes as follows when looking at the weakest to the highest degree of confinement: in the largest cavities - the lowest confinement studied - the entropic barrier increases with N ; for higher confinement, in 920 nm arrays and for lower N in 608 nm arrays, the entropic barrier becomes virtually independent of N , assuming screening of intramolecular hydrodynamic interactions; under the highest confinement – the highest N in 608 nm arrays – the entropic barrier decreases when N increases.

Monte Carlo simulations and scaling arguments [6, 7] for a geometry similar to ours, as sketched in Figure 2, show that the logarithm of reduced diffusion coefficient should depend linearly on N and the slope of such dependence is negative but approaches zero as the hole diameter decreases below a certain value. In the latter case, molecules can show apparent Rouse dynamics, though the diffusion is hindered by the presence of holes and dominated by entropic barriers.

The electron microscopy measurements show that diameter of interconnecting holes between cavities becomes narrower for arrays patterned with smaller particles, as seen in Table 1.

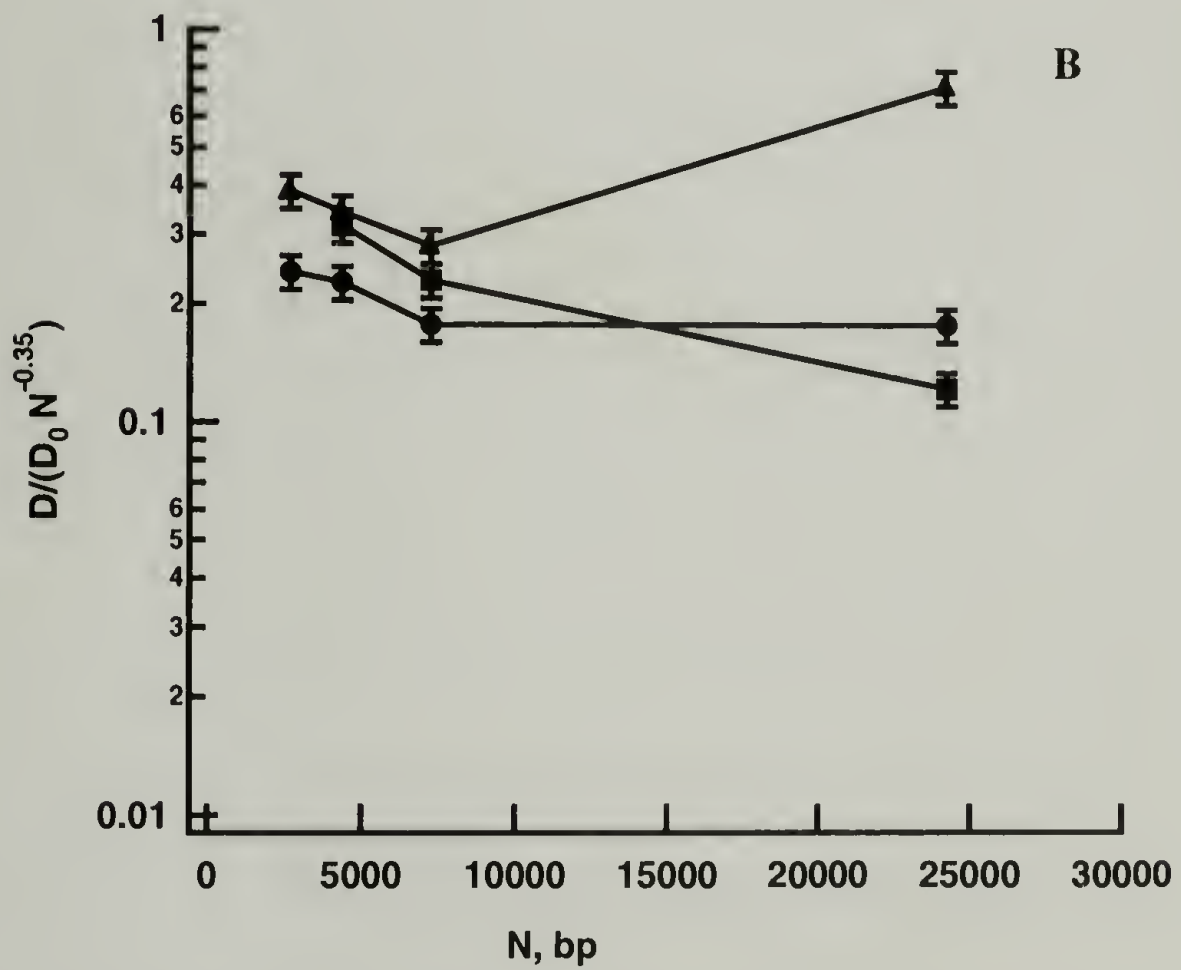
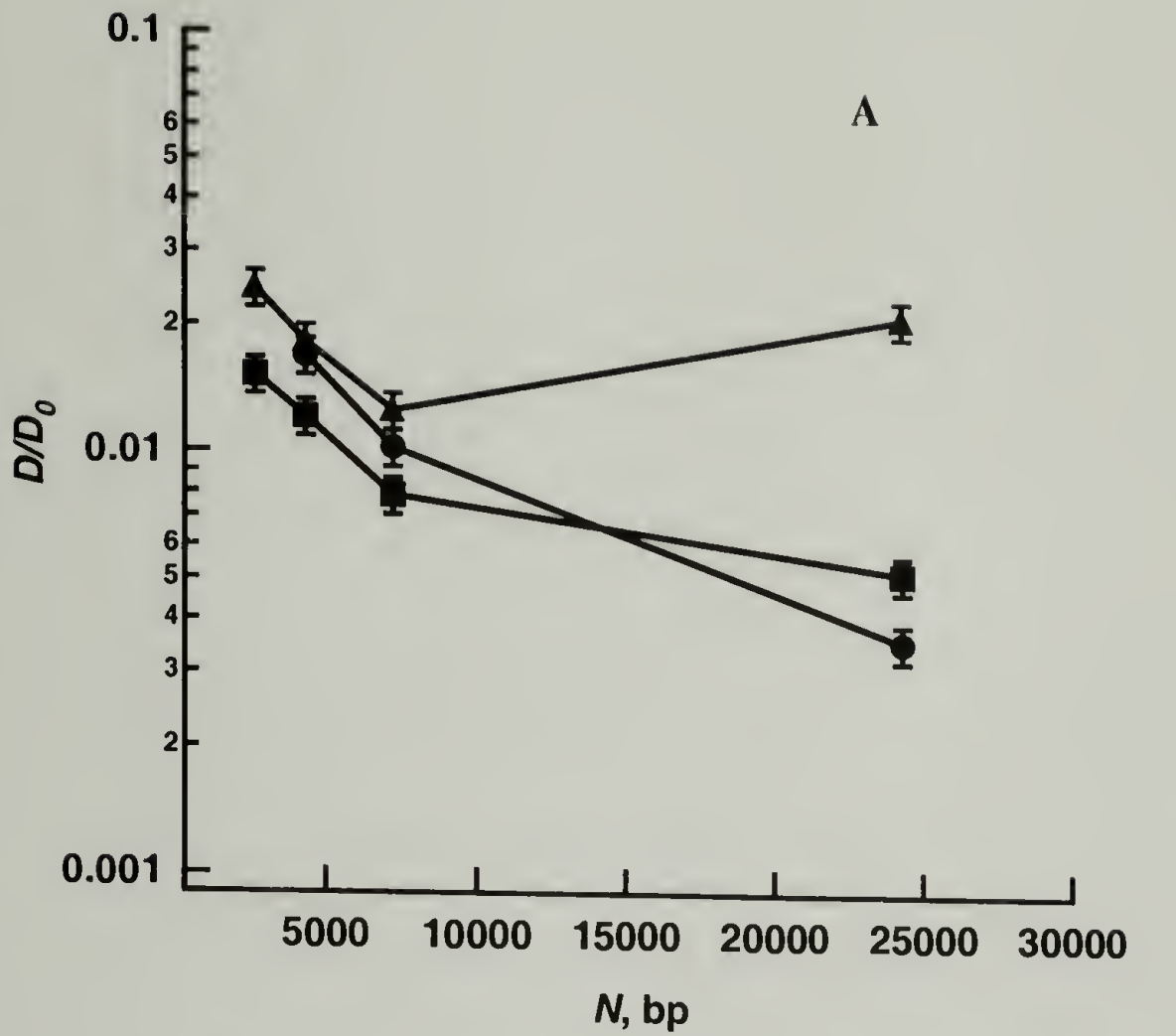


Figure 16. Variations of reduced diffusion coefficient with DNA size. Triangles, circles, and squares represent D in array of 608, 920, and 1400 nm cavities, respectively.

Table 1. The dimensions of cavities and holes in the templated arrays

Cavity Size, nm	Hole Size, nm	SD of Hole Size, nm	Hole/Cavity Size Ratio
608	135	40	0.22
920	195	40	0.21
1400	235	57	0.18

When the hole diameter is small – much smaller than a coil size - and its length is short, it effectively confines only a single segment of a polymer chain. When confined, the segment loses its translational entropy, increasing the free energy of the chain by approximately one kT . For a Gaussian chain in spherical confinement, the confinement energy scales as N , [8] thus redistribution of segments between cavities does not change total confinement energy. Together, these two effects result in virtually constant energy barrier with N change for chain translocation through the hole. For the wider holes, which can confine a whole coil, one expects the energy barrier to depend on the chain size. Experimentally, we see that for the widest holes, in 1400 nm arrays, the radius of gyration is comparable to the hole size, and the dependence of the reduced diffusion coefficient on molecular weight is the strongest. As the hole size decreases, 608 and 920 nm arrays, the dependence become less steep.

Interestingly, the reduced diffusion coefficient starts to increase with N in 620 nm arrays for DNA molecules longer than 7 kbp. Such behavior, to the best of our knowledge, has not been addressed previously either theoretically or with simulations. Apparently, in this case, the energy barrier for translocation through the hole becomes smaller as the chain size increases. Qualitatively this upturn can be explained by the excluded volume effect. Modeling the effect of excluded volume on ΔS_c through self-

consistent-mean-field approximation adds a contribution to the total entropy in the form of $\nu N^2/a^3$, where ν is a measure of excluded volume interaction strength.[9] The removal of a segment from the cavity and then putting it in the hole gives two contributions to the chain energy. The segment confined inside the hole partially loses translational entropy, and this loss is roughly independent of the chain size if the hole is much smaller than the coil dimensions; the removal of the segment from the cavity also decreases segment concentration, lowering the free energy of the remaining chain. The latter effect depends on the total chain length squared and is greater for longer molecules and stronger confinements (smaller cavity sizes). The net result is a lower entropic barrier for the longer molecules. This explains the weak dependence of the reduced diffusion coefficient on N for shorter molecules and its increase for molecules longer than 7 kbp.

Effect of Cavity Size

D depends non-monotonically on cavity size in the arrays, as shown in Figure 17. Independently of N , the diffusion slows down as cavity diameter increases from 608 to 920 nm. For even bigger cavities, both the diffusion increase as well as decrease is observed depending on N . Smaller DNAs, 4.36 and 7.25 kbp length, exhibit a diffusion minimum somewhere around 900 nm cavity size, while there is a consistent reduction of diffusion with the cavity size for 24.3 kbp DNA.

Within the entropic barrier model, cavity size itself does not determine the diffusion rate; it is the interplay of the cavity and hole sizes that controls the diffusion, all other factors being equal.[6, 7, 10] In our experiments we did not vary the cavity

and hole size independently. When the cavity size was increased the hole size also increased, the cavity-to-hole size ratio measured with the scanning electron microscopy, as shown in Table 1, stays approximately constant for all cavity sizes. Unintuitively, D decreases in gels with larger cavity and hole sizes. In general, the electron microscopy imaging of the aqueous gel systems is prone to numerous artifacts which can emerge from sample preparation. Even though care was taken to minimize such possible artifacts, the error in the hole size measurements can still be significant. Uncertainties in measurements of hole-to-cavity size ratios and deficiencies in current theory for entropic barrier transport prevented us from quantitatively explaining the observed phenomena.

To insure the constant ratio between cavity and hole sizes, we performed a control swelling experiment where we used 900 nm spheres to pattern a gel with decreased the crosslink density. The final cavity size, after gel swelling, was 1020 nm, compared to 920 nm in gels with the regular crosslink density. In gel swelling experiments, the cavity-to-hole size ration should stay constant. Nevertheless, D still decreases in the arrays with bigger pores, as illustrated in Figure 17. Such behavior for the first time has been shown to occur and cannot be explained with simple Gaussian description within an entropic barrier model.[10] All studied DNA samples in 608 and 920 nm cavity arrays as well as to the DNA of highest molecular weights studied in 1400 nm cavity arrays show this interesting behavior.

In general, deviations from Gaussian behavior for real chains can be attributed to excluded volume effect and finite chain flexibility.[11-19] Simulations are needed to account for the impact of limited chain flexibility on D , but we do not expect this

impact to be of much significance. Excluded volume, on the other hand, readily explains the upturn in reduced diffusion coefficient with N .

At the mean-field level, when N is kept constant but cavity size is varied, the contribution to the free energy from excluded volume scales as a^{-3} . [9] When the segment is removed from the cavity and placed in the hole, there is a gain in free energy due to the loss of the segment's translational entropy as well as a free energy loss due to reduction of segment concentration inside the cavity. The energy gain should be roughly constant for all cavity sizes. The energy loss is bigger for smaller cavities, resulting in a lower barrier, and accordingly, faster diffusion in the arrays with smaller pores. When cavities become larger, one can expect a smaller contribution from excluded volume in overall free energy so that behavior predicted elsewhere for Gaussian chain, namely the increase of D in the array with larger cavities, is observed.

When analyzing the effect of cavity size on D , hydrodynamic effects are hard to take into account then when looking at N dependence. D_c is not constant within each data set and may change as cavity size changes. The scaling of such change on cavity size is unknown. If anything, D_c is smaller for chains in smaller cavities. This trend cannot explain the unusual behavior we observed. Purely hydrodynamic effects will lead to a slowdown of diffusion in smaller cavities, contrary to our observations, and the reduced diffusion coefficient, D/D_c , will show more pronounced tendency to increase as cavity size becomes smaller. These trends support the conclusion that observed phenomenon – faster diffusion in smaller pores – is brought by an entropic barrier mechanism.

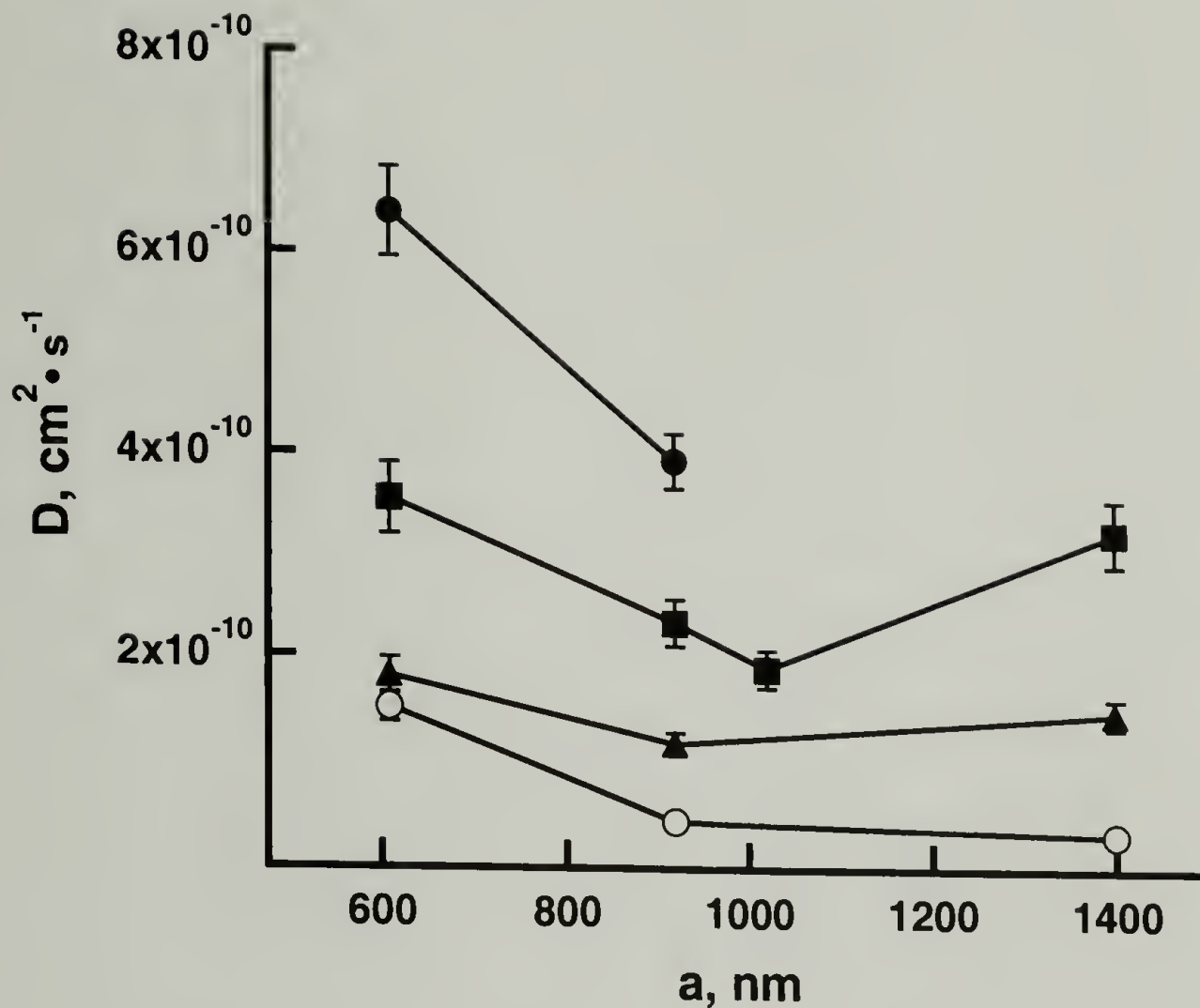


Figure 17. Change of diffusion coefficient of DNA molecules with the size of cavities in the arrays. Closed circles, squares, triangles, and open circles represent DNA sizes of 2690, 4360, 7260, and 24300 bp respectively.

Single macromolecule diffusion has been visualized in a tailorable, ordered environment obtained by colloidal templating.[20] The entropic barriers mechanism of diffusion dominates chain dynamics over a wide range of confinement conditions, producing unexpected effects with respect to chain length and pore size. Under high confinements, the DNA molecules diffuse faster in a medium with smaller pores. For the highest confinement – the biggest molecules in the media with smallest pores - diffusion becomes almost independent of N . Qualitatively such behavior can be explained by the effect of excluded volume on the height of entropic barrier, but

quantitative explanation requires advances in theory polymer confinement and possibly computer simulations.

References

1. Masaro, L. and X.X. Zhu, *Prog. Polym. Sci.*, 1999. **24**(5): p. 731-775.
2. Lodge, T.P., N.A. Rotstein, and S. Prager, *Adv. Chem. Phys.*, 1990. **79**: p. 1-132.
3. Matsumoto, M., et al., *J. Polym. Sci.: Part B: Polym. Phys.*, 1992. **30**: p. 779-783.
4. de Gennes, P.G., *Scaling Concepts in Polymer Physics*. 1979, Ithaca: Cornell Univ. Press.
5. Smith, D.E., T.T. Perkins, and S. Chu, *Macromolecules*, 1996. **29**(4): p. 1372-1373.
6. Muthukumar, M. and A. Baumgärtner, *Macromolecules*, 1989. **22**(4): p. 1937-1941.
7. Muthukumar, M., *J. Non-Cryst. Solids*, 1991. **131**: p. 654-666.
8. Casassa, E.F., *J. Polym. Sci. B*, 1967. **5**(9PB): p. 773-778.
9. Grosberg, A.I.U. and A.R. Khokhlov, *Statistical physics of macromolecules*. AIP series in polymers and complex materials. 1994, Woodbury, NY: American Institute of Physics. xxvii, 350.
10. Muthukumar, M., *Journal of Chemical Physics*, 2003. **118**(11): p. 5174-5184.
11. Giddings, J.C., et al., *J. Phys. Chem.*, 1968. **72**(13): p. 4397-&.

12. Davidson, M.G., U.W. Suter, and W.M. Deen, *Macromolecules*, 1987. **20**(5): p. 1141-1146.
13. Odijk, T., *Macromolecules*, 1983. **16**(8): p. 1340-1344.
14. Teraoka, I., K.H. Langley, and F.E. Karasz, *Macromolecules*, 1992. **25**(23): p. 6106-6112.
15. Limbach, K.W., J.M. Nitsche, and J. Wei, *AIChE J.*, 1989. **35**(1): p. 42-52.
16. Cifra, P. and T. Bleha, *Macromolecules*, 2001. **34**(3): p. 605-613.
17. Tsonchev, S. and R.D. Coalson, *Chem. Phys. Lett.*, 2000. **327**(3-4): p. 238-244.
18. Jaeckel, A. and J. Dayantis, *J. Phys. A*, 1994. **27**(8): p. 2653-2667.
19. Jaeckel, A. and J. Dayantis, *J. Phys. A*, 1994. **27**(23): p. 7719-7731.
20. Nykypanchuk, D., H.H. Strey, and D.A. Hoagland, *Science*, 2002. **297**(5583): p. 987-990.

CHAPTER 5

DIFFUSION OF A CIRCULAR DNA IN AN ARRAY OF SPHERICAL CAVITIES

In previous chapters, we discussed the diffusion of linear chains in a porous media with well controlled pore size and geometry. The direct observation of diffusion let us to elucidate the mechanism of diffusion and explain the general behavior of the molecular diffusion for different sized molecules in different sized pores. Qualitative explanations were given, but additional studies of macromolecular diffusion in the cavity arrays are needed to completely understand macromolecular behavior in a porous medium.

One of the questions to be answered is how a polymer chain threads through a hole. The hole size is certainly big enough to allow bending of the chain, but would chain prefer to form bends or to enter and escape through its ends, as sketched in Figure 18? Will behavior change with chain length? In this respect, it is interesting to compare the diffusion of the linear molecules with the circular ones in the same, well defined porous environment. While the circular chains, in order to diffuse, have to form loops, the linear molecules may diffuse through either threading of the ends or loop formation. The comparison of diffusion coefficients for linear and circular molecules will allow us to estimate the energies of loop formation and the effect of molecular topology on chain dynamics.

The understanding of loop (hernia) formation is important not just for our experimental system. The electrophoretic separation of long DNA molecules in gels is affected, and in some cases, is governed, by loop formation.[1-5] Also, an interesting

technological and scientific challenge is to devise separation methods based on molecular topology not on the size. In biology, this is relevant to separation of circular DNA from linear species. Figure 18D illustrates that loop formation can be important in technological applications when the separation and analysis of branch or star polymers is needed.

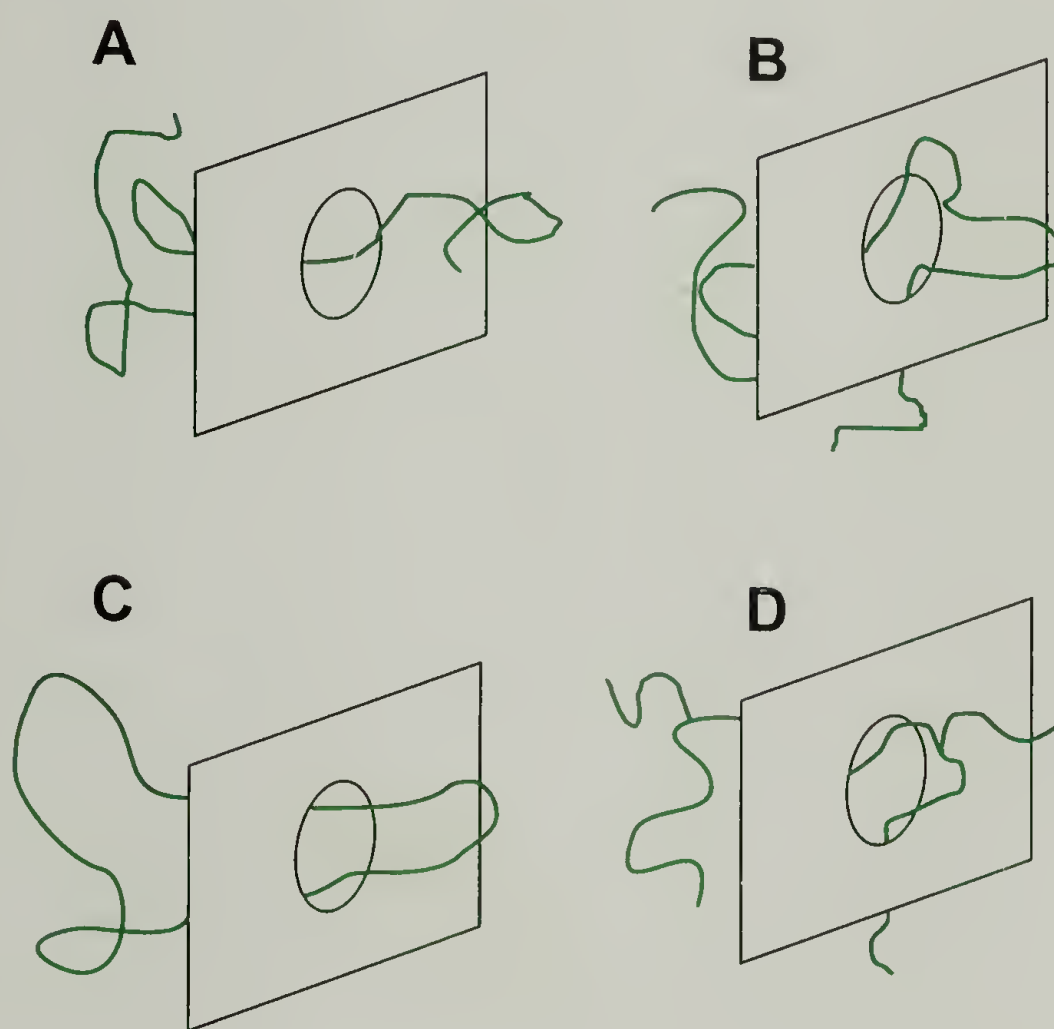


Figure 18. Modes of polymer diffusion through a pore for the molecules of various topologies. **A** and **B** are showing linear molecule diffusion through the pore; **A** – “end first” mechanism and **B** – “loop first” mechanism. **C** and **D** show circular and branched molecule diffusion through a pore.

In biology, understanding of the loop formation mechanism – both its thermodynamics and dynamics – is relevant for a large class of bacterial DNAs – plasmid vectors. These circular molecules are present in a variety of prokaryotic and eukaryotic organisms and are widely used in molecular cloning. In a cellular environment, their transport will be affected by loop formation. Also, DNA bending

occurs during DNA compaction and DNA interaction with enzymes. It is not surprising that considerable attention is directed to study thermodynamic of circular molecules and their diffusion.[6-15]

The behavior of ring polymers in a free solution is well understood.[16-18] Several studies showed that the average chain dimensions for circular molecules is smaller than that for linear molecules, but the scaling of the size with molecular weight does not change. Similarly, the diffusion coefficient in free solution scales the same for linear and circular molecules but circular molecules diffuse faster than linear ones.

Less is known about the behavior of circular molecules in dense environments. Most theoretical studies focused on the effect of loop formation in reptation and electrophoresis of DNA.[9, 10, 15] The experimental studies regarding transport of circular molecules in porous media exclusively looked at electrophoretic experiments.

The comprehensive study of ring polymer diffusion in dense environments has not been done for two main reasons. First, the difficulties to obtain pure samples of ring polymers with low polydispersity and, second, lack of well defined porous media where pore geometry, size, and chemistry can be controlled.

Most naturally occurring plasmid DNA are mixtures of topologically different molecules. A majority of molecules in a typical plasmid sample are superhelical DNAs; such molecules do not behave as statistical coils and have unique conformations. The studies of such molecules are interesting in regard of superhelicity phenomenon but have little value to polymer physics.

Until recently, the few methods accessible to polymer physicists to get relaxed circular molecules could not provide samples of high purity and consistency. Circular

ds-DNA molecules can be relaxed by inducing the nick in a single strand which allows a free rotation of the strands and twist relaxation. The chemical nicking of DNA molecules, which is used most often for this purpose, gives a mixture of nicked (nDNA) as well as linear species. The nicking, in this case, is uncontrolled, nicking sites are randomly distributed along the molecule backbone, and the number of nicks per molecule varies statistically. The use of topoisomerases, enzymes binding to DNA and unwinding the helix, is also not optimal. DNA unwound by these enzymes has both strands covalently bound in a circle. Change of buffer ionic strength, pH, or composition leads to DNA twists and induced superhelicity, limiting studies to buffers similar to the ones used for the enzymatic reaction.

Recently, new and sequence specific DNA enzymes that induce single strand nicks were developed and became commercially available.[19-23] Those enzymes introduce nicks in a DNA molecule in a controlled manner for obtaining topologically pure DNA samples. Likewise, recent advances in polymer chemistry allow synthesis of ring polymers of low polydispersity and various molecular weights.[24] We expect new studies involving synthetic ring molecules to appear soon.

All DNA molecules and enzymes were purchased from New England Biolabs. The linear samples were obtained as described in chapter 2. Relaxed circular DNA molecules were obtained with N.BbvC IA and N.BstNB I nicking enzymes. The N.BbvC IA nicks DNA in the 5'...GC[∇]TGAGG...3'/3'...CGACTCC...5' position, N.BstNB I nicks in the 5'...GAGTCNNNN[∇]N...3'/3'...CTCAGNNNNN...5' position. N.BbvC IA nicking enzyme produces two nicks separated by 49bp located on opposite strands in M13mp18 plasmid. N.BstNB I relaxes pBR322 and pUC19 by making four

nicks in each plasmid. In relaxed pBR322, the nicks are separated by at least 480bp, and in pUC19, the closest nicks are located 266bp apart on opposite strands. The DNA labeling and diffusion visualization was carried out as described in previous chapters. The study was done for 920 nm cavity arrays.

Visually, nDNA molecules diffuse in a similar manner to linear molecules in the cavity arrays. Most of the time, molecules fluctuate inside a single cavity, and the movement from cavity to cavity occurs via rapid jumps. The details of the jumping dynamics could not be resolved.

As described previously, the jumping probability distribution in the arrays should ideally be described by a Poisson distribution.[25] Analysis of the jumping frequency probability for nDNA showed a different behavior. Figure 19 presents the jumping probability for both linear and circular DNA molecules of three molecular weights studied. The average jumping frequency is lower for all circular molecules compared to their linear counterparts. Only for the 7.25 kbp and 4.36 kbp DNA samples can the jumping probability of nDNA be described with a single Poisson. The 2.69 kbp samples of nDNA showed broader jumping probability distribution than a single Poisson. We ascribe this broadening to the degradation of the labeled DNA molecules during handling and imaging.

The labeling with TOTO dye leads to DNA nicking under illumination.[26] Due to prior nicking with enzyme, the relaxed circular DNA already has nicks present even before the imaging. Introduction of additional nicks to DNA strands, during illumination, may result in two nicks being created in close proximity to each other and subsequent DNA breakage. As a result, one would expect the illuminated sample to

contain both relaxed circular molecules and newly formed linear molecules. The probability to form linear molecules due to chain degradation should increase with the number of nicks per chain length. Table 2 shows the enzymatically expected average number of base pairs per single nick in each of the studied samples. Indeed, the jumping probability distribution broadening was observed for the molecules with the shortest average distance between nicks.

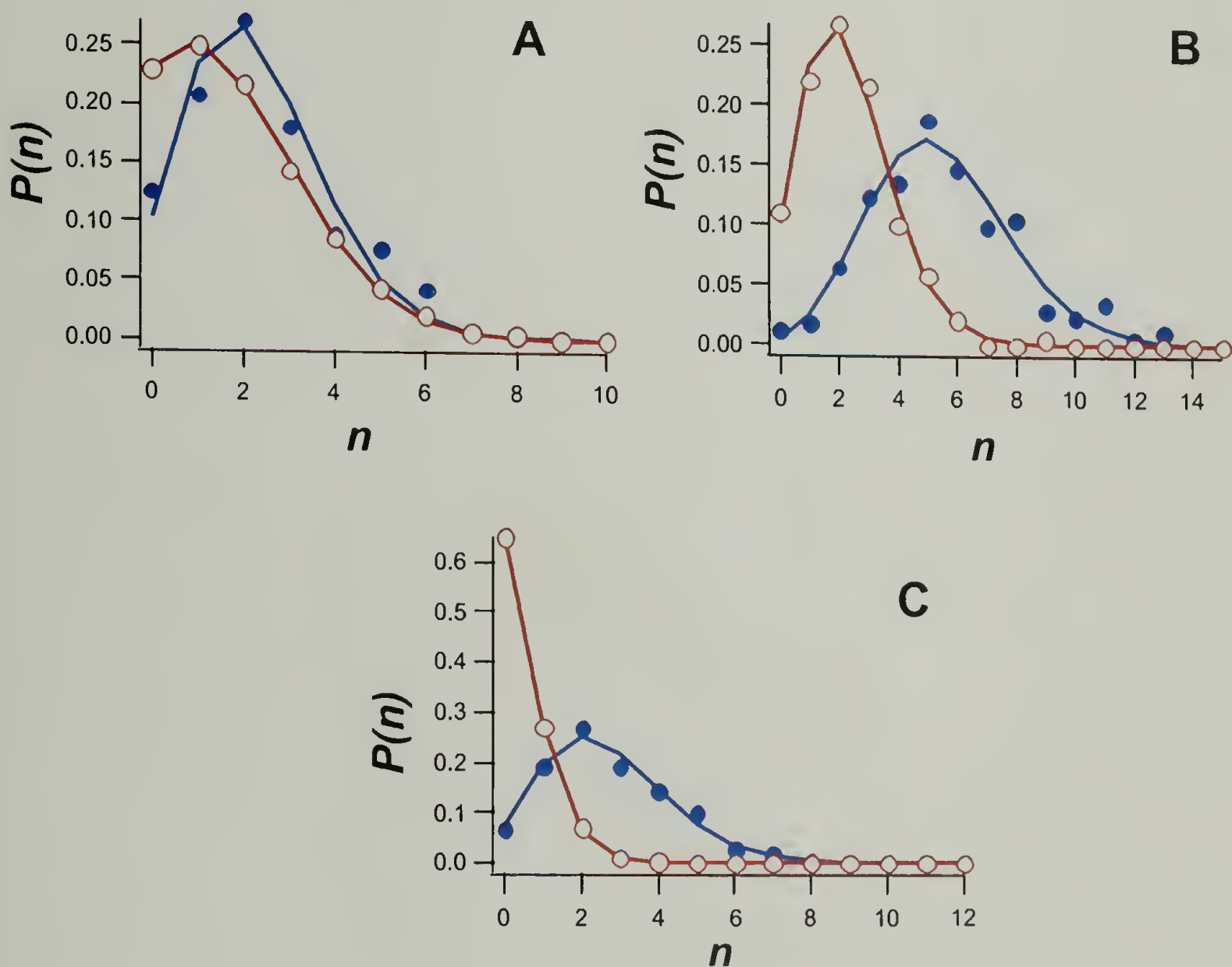


Figure 19. Jumping frequency distribution of linear and nicked DNA molecules plotted as a probability $P(n)$ of number of jumps n in a time window t . Measured jumping frequency of linear molecules is shown as solid circles; jumping frequency nDNA samples shown with open circles. The lines represent the fitting to Poisson distribution or to a sum of two Poisson. **A** – 2.69 kbp DNA, $t=12.5s$; **B** – 4.36 kbp DNA, $t=50s$; **C** – 7.25kbp DNA, $t=50s$.

Table 2. Average number of nicks per circular DNA molecule introduced with nicking enzymes.

N, bp	bp/nick
2,690	675
4,360	1,090
7,250	3,625

To extract the diffusion coefficient of the circular molecules for the samples that showed broad distribution of jumping frequency, we fitted the data with the sum of two Poissons and obtained an excellent fitting, as indicated in Figure 19A for 2.69 kbp DNA. Two values for the jumping frequency, $\Gamma_1 = 0.190 \text{ s}^{-1}$ and $\Gamma_2 = 0.050 \text{ s}^{-1}$ were deduced from this fitting. The jumping frequency for faster moving species corresponds well to the jumping frequency of linear molecules, $\Gamma = 0.187 \text{ s}^{-1}$. Thus, the jumping frequency of 0.050 s^{-1} corresponds to the diffusion of nicked DNA. Since we know that one of the peaks corresponds to diffusion of linear molecules, fixing its position to jumping frequency found for linear DNA of the same molecular weight reduces the fitting uncertainty.

Additional confirmation that jumping frequency distribution broadening occurs because both linear and circular molecules are present in a final mixture was obtained with the 4.36 kbp sample. For 4.36 kbp nDNA samples with higher than usual exposure to light, we observed that the measured jumping frequency distribution was broadened compared to that of the same DNA which had been handled carefully to minimize light exposure, a comparison highlighted in Figure 20. The broadened jumping frequency distribution was again fitted with the sum of two Poisson functions. Two jumping frequencies obtained from the fit, $\Gamma_1 = 0.145 \text{ s}^{-1}$ and $\Gamma_2 = 0.054 \text{ s}^{-1}$. The Γ_1 value is close

to the jumping frequency of linear molecules 0.115 s^{-1} , and Γ_2 is close to the jumping frequency $\Gamma=0.046\text{s}^{-1}$ of nDNA samples that show a single Poisson distribution. When Γ_1 is fixed to 0.115 s^{-1} – the jumping frequency for linear molecules – Γ_2 fits to 0.045s^{-1} , thus confirming that slower moving molecules are relaxed circular DNAs.

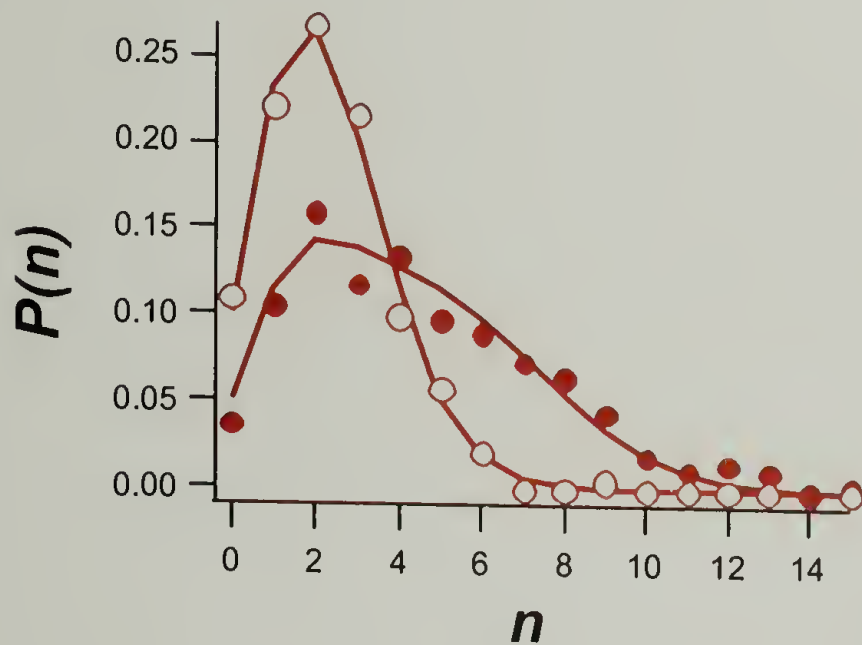


Figure 20. Jumping frequency distribution for nicked 4.36 kbp DNA molecules plotted as a probability $P(n)$ of number of jumps n in a time window $t=50\text{s}$. Measured jumping frequency of molecules for nDNA sample minimally exposed to light are shown as open circles; jumping frequency of molecules for nDNA sample that had longer exposure to light are shown as closed circles. The lines represent fitting to Poisson distribution.

Using equation (7), a jumping frequency can be transformed into a diffusion coefficient. Table 3 compares the measured diffusion coefficients for linear and circular DNA molecules. Values for diffusion coefficients of linear molecules with R_g equal to that of circular molecules are extrapolated from the data for linear DNA assuming that ratio of mean square radii of gyration for linear and circular molecules is 1.7 and that form of D dependence on N for linear molecules does not change outside the measured

interval. R_g for the dye labeled linear DNA molecules are estimated in chapter 6. The extrapolated values for diffusion coefficient are given only for qualitative comparison.

Table 3. Measured diffusion coefficients of circular and linear molecules in the cavity array

Size of Circular DNA, kbp	$D, \text{cm}^2/\text{s}$		
	Circular	Linear of equal N	Linear of equal R_g
2.69	1.14E-10	3.96E-10	6.1E-10
4.36	9.74E-11	2.4E-10	3.6E-10
7.25	1.99E-11	1.12E-10	2.1E-10

Independent of molecular weight, circular molecules diffuse from 2.5 to 5.6 times slower than corresponding linear molecules of the same molecular weight, and 3.7 to 10.6 times slower than corresponding linear molecules of the same average dimension. Such results qualitatively reveal that linear molecules may form loops during translocation through holes between cavities, but the probability of such events is low. The predominant mode of diffusion for linear molecules is “end first”. This result is true for the molecular weights between 2.69 and 7.25 kbp, but the behavior may change for the higher molecular weights, when the fraction of end segment decreases relative to the total concentration of polymer segments. The answer to the question if “loop first” mode of diffusion is possible for molecule of bigger size than studied here and, if so, under what conditions, requires additional investigation.

To explain the slowdown of diffusion for molecules that have to form loops in order to diffuse, we need to look in detail at the energies of loop formation. The free

energy ΔF_l of threading the loop through the hole consist of two contributions, ΔF_b and ΔF_c . [2, 4, 27] The former is the energy of chain bending, approximately equal to kTl_p/a , where l_p is a persistence length. The latter is a confinement energy of a loop. The contribution of the bending term in the total energy is small – less than one kT – since the hole size $a=200$ nm and persistence length l_p of labeled DNA molecules is 25 nm (see chapter 6). The confinement energy term is more complicated and requires separate consideration.

The confinement energy of a polymer threading through the hole, has at least two terms. One part is the loss of entropy of the polymer segments confined inside of the hole, and the other contribution comes from the pinching the chain ends at the surface, thus restricting the total number of conformations available to the chain segments outside of the hole. The entropy loss due to confinement of segments inside a hole, as discussed in chapter 4, is roughly independent of the molecular weight of a polymer and is on an order of kT . Figure 18C illustrates that for the circular molecules, two strands are confined simultaneously inside a hole during the polymer threading. Even though, the strands are connected, the confined segments on the strands behave independently once they are separated by more than one persistence length along the chain contour. The entropy loss due to segment confinement inside of the hole is expected to be at least two times higher than such energy for linear molecule that diffuses in “end first” regime. The repulsive interactions between the segments of the two strands in the hole will increase this confinement term even more for the circular molecules.

The free energy part that is coming from entropy loss due to fixing polymer chain ends on a surface is difficult to estimate. A question that must be answered is for which case is the entropy loss higher – when transferring a linear polymer chain from solution to the surface and fixing one of the chain ends on the surface, or when transferring a circular molecule to the surface and pinching the segment on the surface? The circular molecule pinched by a segment to the surface is equivalent to having the linear chain of the same contour length attached to a point at the surface by both of its ends. To find the change of configurational entropy in the described cases, simulations will be required.

Hydrodynamic interactions have an interesting effect on the diffusion of circular DNA in comparison to linear ones. The pre-exponential term D_c has different dependence on molecular weight for circular and linear molecules depending on the degree of screening of intramolecular hydrodynamic interactions. When the hydrodynamic interactions are not screened, the friction coefficient for chain diffusion is proportional to chain average radius. Under this condition, the D_c is equivalent for circular molecule and the linear molecule of the same R_g . Once confinement increases, the hydrodynamic interactions between segments become screened making the friction coefficient proportional to number of segments N . Hence, D_c for circular molecule, when the hydrodynamic interactions are screened, is closer to D_c of the linear molecule of the same N rather than the same R_g . This fact precludes direct estimation of the energy barrier change by comparing the diffusion coefficients of circular and linear molecules under entropic barrier transport.

The single molecule visualization of circular DNA dynamics in cavities arrays revealed the different mechanism of molecule threading through the hole for these two topologies. Unlike circular molecules that have to form loops in order to diffuse from cavity to cavity, the linear molecules can diffuse through their ends. The differences in diffusion mode give rise to the difference in diffusion coefficients up to ten times for the molecules of the same molecular dimensions but different topology. Such results promise that separation of macromolecules based on the topology is possible under entropic barrier mechanism. Additional theoretical studies are needed to understand in details the differences between circular and linear molecule diffusion under entropic barrier mechanism.

References

1. Akerman, B., J. Chem. Phys., 1997. **106**(14): p. 6152-6159.
2. Akerman, B., Phys. Rev. E, 1996. **54**(6): p. 6685-6696.
3. Long, D. and J.L. Viovy, Physica A, 1997. **244**(1-4): p. 238-253.
4. Long, D. and J.L. Viovy, Phys. Rev. E, 1996. **53**(1): p. 803-811.
5. Semenov, A.N. and J.F. Joanny, Phys. Rev. E, 1997. **55**(1): p. 789-799.
6. Akerman, B., J. Phys. Chem. B, 1998. **102**(44): p. 8909-8922.
7. Alon, U. and D. Mukamel, Phys. Rev. E, 1997. **55**(2): p. 1783-1793.
8. Grosberg, A. and S. Nechaev, Adv. Polym. Sci., 1993. **106**: p. 1-29.
9. Kholodenko, A.L., Macromol. Theory Simul., 1996. **5**(6): p. 1031-1064.

10. Klein, J., *Macromolecules*, 1986. **19**(1): p. 105-118.
11. Lee, W., et al., *Macromolecules*, 2002. **35**(2): p. 529-538.
12. Marko, J.F., *Physica A*, 1997. **244**(1-4): p. 263-277.
13. Muller, M., J.P. Wittmer, and M.E. Cates, *Phys. Rev. E*, 2000. **61**(4): p. 4078-4089.
14. Obukhov, S.P., M. Rubinstein, and T. Duke, *Phys. Rev. Lett.*, 1994. **73**(9): p. 1263-1266.
15. Rubinstein, M., *Phys. Rev. Lett.*, 1986. **57**(24): p. 3023-3026.
16. Bernal, J.M.G., et al., *Macromolecules*, 1990. **23**(13): p. 3357-3362.
17. Naghizad.J and Sotobaya.H, *J. Chem. Phys.*, 1974. **60**(8): p. 3104-3108.
18. Baumgartner, A., *J. Chem. Phys.*, 1982. **76**(8): p. 4275-4280.
19. Besnier, C.E. and H.M. Kong, *EMBO Rep.*, 2001. **2**(9): p. 782-786.
20. Higgins, L.S., C. Besnier, and H.M. Kong, *Nucleic Acids Res.*, 2001. **29**(12): p. 2492-2501.
21. Morgan, R.D., et al., *Biol. Chem.*, 2000. **381**(11): p. 1123-1125.
22. Xu, Y., K.D. Lunnen, and H.M. Kong, *Proc. Natl. Acad. Sci. U. S. A.*, 2001. **98**(23): p. 12990-12995.
23. Zhu, Z.Y., et al., *J. Mol. Biol.*, 2004. **337**(3): p. 573-583.
24. Bielawski, C.W., D. Benitez, and R.H. Grubbs, *Science*, 2002. **297**(5589): p. 2041-2044.

25. Nykypanchuk, D., H.H. Strey, and D.A. Hoagland, *Science*, 2002. **297**(5583): p. 987-990.
26. Akerman, B. and E. Tuite, *Nucleic Acids Res.*, 1996. **24**(4): p. 1080-1090.
27. Cohen, G. and Eisenber.H, *Biopolymers*, 1966. **4**(4): p. 429-&.

CHAPTER 6

DNA PARTITIONING IN SPHERICAL CAVITIES

Weak and Moderate Confinement

Pairs of well-defined spherical cavities of submicron size were prepared by the colloidal templating method as described in chapter 2. A single fluorescently labeled linearized plasmid was trapped inside such pairs and the plasmid motion was observed via fluorescent microscopy. Image acquisition times varied from 100 to 500 ms, and the interval between image collection ranged from 100 ms to 3 s. Molecules were monitored for periods of up to 25 minutes, shuttering (Vincent Associates Uniblitz) employed to eliminate light exposure except during image acquisition.

Combinations of linearized plasmid and cavity sizes that produced useful partitioning data are given in Table 4. Tabulated radii of gyration R_{g0} are estimates of DNA's ideal or unperturbed dimensions in absence of intercalating dye; unfortunately, sample quantities were insufficient for measurement of actual radii of gyration R_g , expected in all cases to exceed R_{g0} by less than 50%. Under all conditions listed in Table 4, R_{g0} is much less than the larger diameter D_1 or the smaller diameter D_2 of the

Table 4. Experimental parameters

Molecular Size (base pairs, bp)	R_{g0} (nm)	D_1 (nm)	D_2 (nm)	K_p
2,686	123	1400	920	0.83 ± 0.16
4,361	157	608	350	0.01 ± 0.009
4,361	157	608	462	0.22 ± 0.11
4,361	157	920	608	0.53 ± 0.18
7,249	203	1400	608	0.054 ± 0.037
7,249	203	920	608	0.095 ± 0.021

cavities in which partitioning was examined. Following past practice, we view confinement under such conditions as “weak” or “moderate.”

In chapter 3, 4, and 5, we reported single molecule visualization of polymer diffusion within two-dimensional cavity arrays made by colloidal templating.[1] The focus now turns to thermodynamics rather than dynamics. The different objective favors pore geometries that impose two regions of unequal confinement connected by a passage that allows rapid chain interchange. From experience with cavity arrays, we envisaged that evaporative deposition of highly dilute, bidisperse colloidal beads would drive at least a few mismatched beads to pair on a substrate, creating templates for isolated, asymmetric cavity pairs. From the same experience, we anticipated that each isolated cavity pair would host a round interconnecting hole. We thus chose the target geometry sketched in Figure 21. Even at the outset, some difficulties could be anticipated with this approach. First, the desired cavity pairs will be extremely sparse, and second, only a small fraction of these pairs will likely contain a DNA molecule. The overall success rate will inevitably be low. We hoped that rapid scanning by optical microscopy would lead us to the few cavity pairs of appropriate configuration.

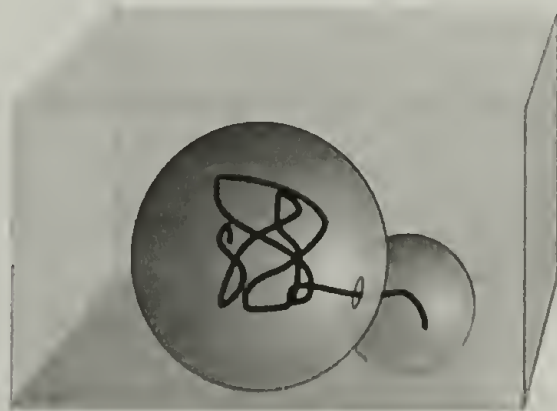


Figure 21. Schematic of two-cavity confinement for unequal size cavities.

Each consideration of the previous paragraph was borne out by actual experiment. Properly trapped DNA chains could be identified and then imaged as Brownian motion “rattled” the chains within and between cavities. Figure 22 shows a sequence of six selected images illustrating the rattling of a 7,249 bp DNA between 1,400 and 608 nm diameter cavities. In the four-minute realization from which these frames were extracted, the molecule jumped from the large to the small cavity, where the molecule resided for several seconds before jumping back. DNA configurations are partially resolved in the large cavity but not elsewhere. Spatial resolution of DNA configuration is mainly limited by fluctuations over the finite period of image capture. Resolution in the small cavity and in the region of the interconnecting hole is reduced by refraction from cavity walls. Of the hundreds of frames collected in this particular sequence, only one (frame e) reveals an obvious bridging configuration. Other frames offer no indication that segments of a confined chain even partially fingered into the opposite cavity, although a small, highly transient fraction of penetrated segments could well escape detection.

Optical and electron microscopies revealed good replication of polystyrene beads by open spherical cavities, as shown in chapter 2, but little information could be garnered about cavity-to-cavity interconnecting holes. For equal-sized cavities in a monolayer, the holes were nearly circular, their diameters roughly 20% of that for the two contacting beads. For pairs of unequal-sized cavities, holes could not be imaged accurately due to their scarcity and awkward geometry. The contact of bead with planar substrate can be viewed as the limit of asymmetric bead contact. Holes created by this asymmetric contact possess a diameter about 30-35% of that of the contacting bead, as

seen in Figure 23. From the similar outcomes at the two limits, we deduce that hole diameter for unequal cavity pairs lies around 20-35% of the small bead diameter. It must be emphasized, however, that to the extent that DNA confinement is not significantly disturbed, hole diameter is unimportant to interpretation of equilibrium partitioning. Holes are needed only to achieve rapid thermal equilibration of polymer between neighboring cavities. If our deduction about their size is correct, holes are large enough to admit DNA kinks and folds.

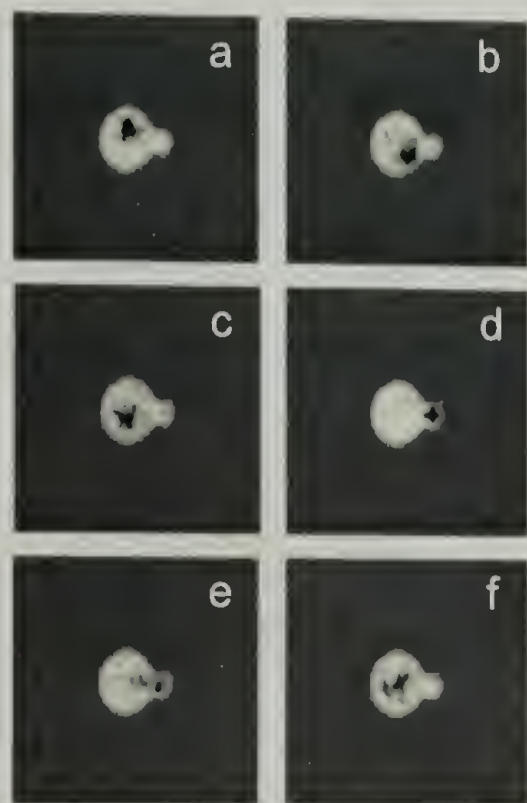


Figure 22. Six frames of 7,249 bp DNA partitioned dynamically between 1,400 and 608 nm diameter cavities. Each frame overlaps visible and fluorescence images. In these non-sequential frames, DNA appears as a diffuse blackened speckle or streak against the lighter background of the cavities; the chain is better resolved when the fluorescent image is colorized. Optical effects exaggerate the size of interconnecting hole. In frame d, the DNA is fully confined to the smaller cavity; in frame e, the DNA bridges.



Figure 23. Scanning electron microscope image of templated hydrogels in a point of contact of templated beads and supporting surface.

Each molecular realization was tracked until fluorescence bleaching led to significant loss of image quality, between 2 to 25 minutes, a period dependent on the size of the chain, the cavity geometry, and the illumination protocol needed to image chain location. Asserting the principle of ergodicity, the cavity-to-cavity partition coefficient K_p is the ratio of times spent in small and big cavities divided by the corresponding ratio of cavity volumes. This coefficient equals the ratio of partition coefficient K_1 and K_2 for the two separated cavities. Since cavity-to-cavity jumps were infrequent, averaging over multiple realizations was necessary to improve statistical accuracy in K_p . Where confinement remained weak or moderate, as was the case for all isolated cavity pairs, the rare frames displaying bridging configurations were ignored. In remaining frames of an image sequence, molecules could be unambiguously assigned to one of the two cavities. Defining ΔS_p as the confinement entropy difference between cavities, $K_p = \exp(\Delta S_p/k)$. The Gaussian chain theory predicts, [2]

$$\text{Ln}K_p = \text{Ln}\frac{K_2}{K_1} = (2/3)\pi^2 Lb(1/D_1^2 - 1/D_2^2) \quad (10)$$

where L and b are the contour and Kuhn lengths of the polymer, respectively. The final expression accounts only for the first term of expansions for K_1 and K_2 (the full expansion is given as eqn. 2 in ref. 2), but at confinement conditions encountered for isolated cavity pairs, higher terms were insignificant.

Although sampling errors in K_p diminished as more cavity-to-cavity jumps were registered, a single molecule method cannot achieve the precision of a method sensitive to the full ensemble. The number of jumps convolutes the abundance of realizations with the magnitude of K_p . We imposed the minimum requirements of 2 realizations and 4 jumps, thereby eliminating many sought-after parameter combinations. Data passing these requirements span the interval $0.01 < K_p < 1.0$ for a disparate set of cavity pairs and DNA sizes. Fortunately, this interval corresponds to the confinement conditions of greatest relevance to polymer separation methods. Values of K_p are listed in the last column of Table 4.

In comparing experiment to theory, an important consideration is the impact of intercalating dye on the physical properties of DNA. According to literature, at the labeling condition chosen, TOTO-intercalated DNA is about 33% longer than native DNA.[3, 4] The literature is less clear about the effect of the dye on DNA stiffness.[3, 5] We used analytical centrifugation (Beckman Optima XL-1) in the velocity mode to measure the friction coefficient of single persistence length, TOTO-intercalated DNA. Single persistence length DNA samples were obtained from NIH. The ultracentrifuge

was run in the three cell mode at 20000 rpm. The sedimentation velocity was measured using UV detection at 260 nm. The sedimentation coefficients for TOTO-labeled DNA and unlabeled DNA were measured during the same run; for both DNA samples, the initial DNA concentration was $50\mu\text{g/ml}$. An example of obtained sedimentation profiles is given in Figure 24. The solute concentration in plateau C_p relates to the initial concentrations in the centrifuge cell C_0 as $C_p = C_0 \exp(-2s\omega^2 t)$, where s is a solute sedimentation coefficient, ω is angular velocity, and t is a sedimentation time. The slopes in the curves in Figure 25 provide the sedimentation coefficient for labeled and unlabeled DNA, which are equal to 10.9 and 9.7 Svedbergs for DNA with and without the intercalated dye respectively.

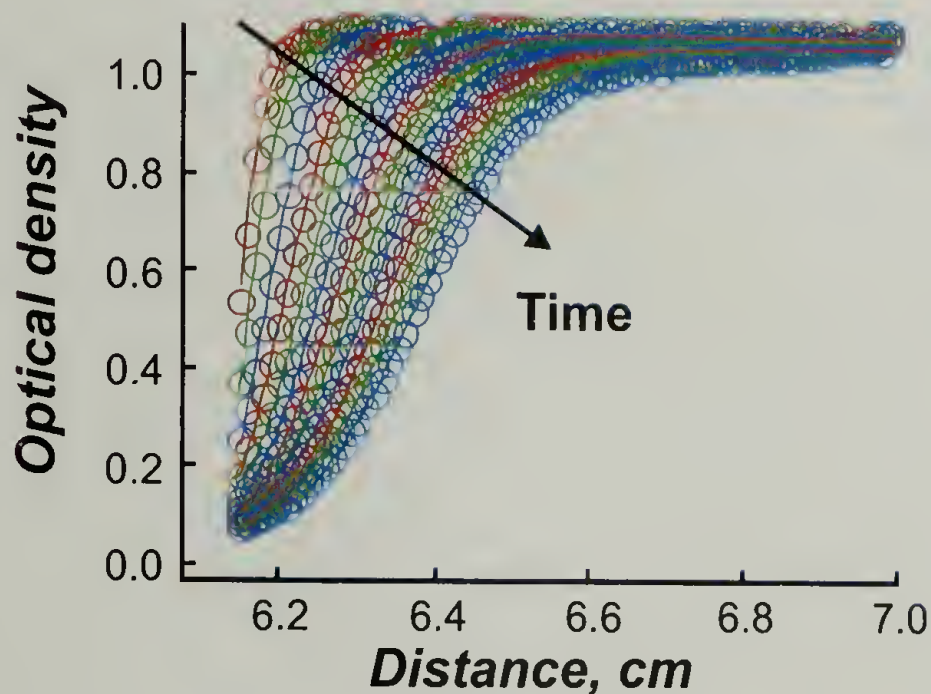


Figure 24. Sedimentation profile of TOTO-labeled DNA given as the optical density of DNA solution as a function of the distance from the center of the centrifuge rotor.

Applying the wormlike chain model[6] and assuming dye-insensitive specific volume, a diameter of 2.5 nm for both labeled and unlabeled DNA, and the persistence length, l_p , of 50 nm for native DNA, the measurement yielded $b=50\pm 22$ nm, the error in

b based on uncertainty in fitting of sedimentation coefficient. For native DNA, $b=100$ nm, demonstrating that dye intercalation, as performed here, reduces chain stiffness. The result is not very sensitive to the values of chain diameter and DNA persistence length. On the other hand, the calculated value for Kuhn length for labeled DNA changes considerably if the diameter of labeled and unlabeled DNA were taken to be different. When labeled DNA is taken to have a bigger diameter than DNA without the intercalating dye, the calculated Kuhn length reduces to values below 50 nm.

A related issue is the potential loss of chain stiffness as single strand nicks form under illumination of the microscope. At high light levels, chain breakage occurs frequently, presumably because of the development of closely spaced nicks on opposite strands of the double helix. At the lower light levels chosen for this study, breakages are rare, and DNA behavior appears steady in time.

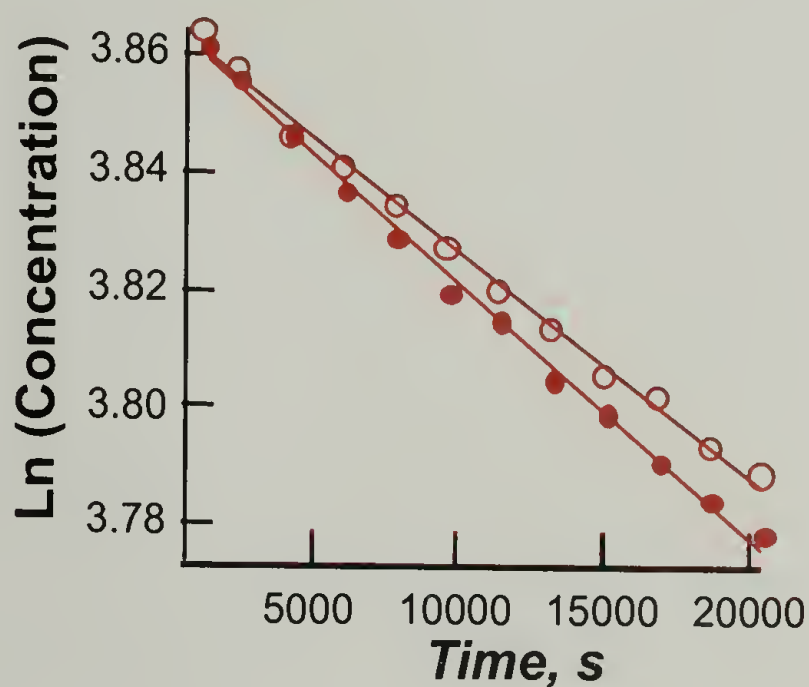


Figure 25. The logarithm of relative concentration change with sedimentation time for labeled (solid symbols) and unlabeled (open symbols) DNA.

Employing dye-corrected values for L and b , Figure 28(a) plots the measured K_p against the theoretical prediction of equation (10). The 95% confidence interval error bars plotted in the figure and listed in Table 4 manifest random sampling errors, which are substantial for the experimental conditions providing few jumps. The ratios of R_{g0} to D_1 and D_2 ranged from 0.072 to 0.21 and 0.11 to 0.37, respectively, and the ratio of D_1 to D_2 ranged from 1.0 to 2.3. Both small and large cavity diameters varied sufficiently to illustrate both weak and moderate chain confinement, corresponding to chains trapped in much larger or comparably sized pores, respectively. With no adjustable parameters, good agreement is demonstrated between experiment and Gaussian chain theory for the interval $0.3 < K_p < 1.0$, but agreement worsens at smaller K_p , where the theory systematically overpredicts the measurements. Large uncertainty in the measured Kuhn length for the labeled DNA may be responsibly for the observed deviation. Figure 26 shows two limiting cases in which the Kuhn length is taken at its extreme values, $b_{min}=28$ nm and $b_{max}=72$ nm, parts **A** and **B**, respectively. The Gaussian chain theory for partitioning can both underpredict and overpredict the experimental results due to uncertainty in Kuhn length. Using the least mean squares method, the best fitting is at $b=56$ nm, where the agreement of the theory with the experiment is excellent, as displayed in Figure 27. We conclude that the Gaussian theory correctly identifies a complex variable combination that controls K_p when confinement conditions are weak and not too dissimilar between cavities. Deviations at small K_p may be due to errors in the Kuhn length measurement, but other explanations are also possible. In particular, as suggested by the results for DNA diffusion in the cavity array, the segmental excluded volume may be important at the studied levels of confinement.

The enhanced segment density in the small cavity emphasizes excluded volume interactions, lowering K_p

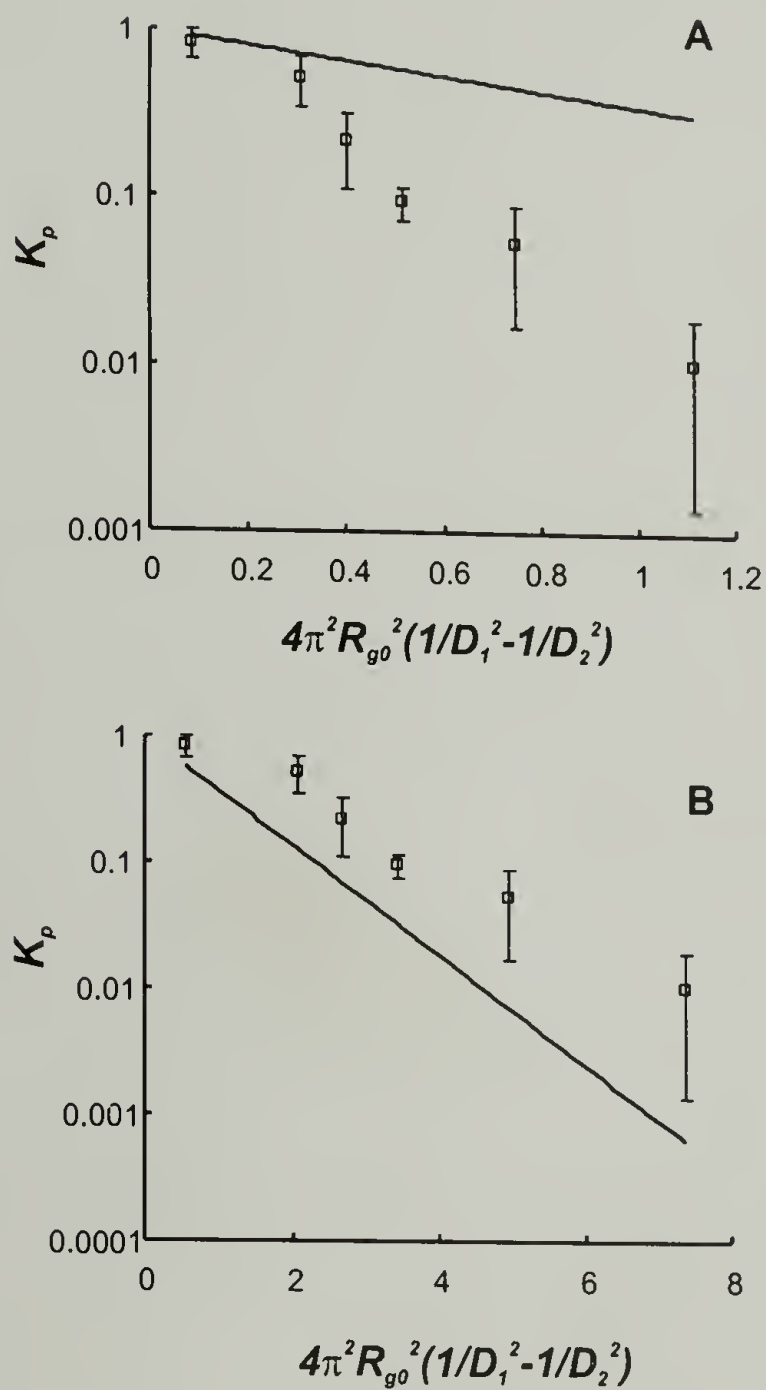


Figure 26. Experiment compared to theory for the Gaussian chain cavity-to-cavity partition coefficient K_p using extreme values for b . **A** is for b_{min} and **B** is for b_{max} .

below Gaussian predictions. Modeling this “crowding” effect via an approximate mean-field or Flory-type argument adds a contribution to ΔS_p of the form,[7]

$$\Delta S'_p \sim \nu N^2 (1/D_1^3 - 1/D_1^3) \quad (11)$$

where ν , a measure of excluded volume interaction strength, is proportional to the segment-segment binary cluster integral. The mean field argument supposes that segments distribute themselves uniformly throughout the cavity interior, only a zero order approximation to the actual distribution. Further, the argument assumes that excluded volume makes only an additive correction to ΔS_p , again a crude approximation. Onsager evaluated the binary cluster integral for a pair of charged cylinders,[8] and numerous successful models for DNA virial coefficients and single chain dimensions have incorporated his result.[9, 10] For confinement of cylindrical segments in a large spherical cavity, Onsager’s result can be written $\nu=1.5b^2d_{\text{eff}}$, where d_{eff} is the effective DNA backbone diameter. For 0.035 molar 1:1 electrolyte, parameters characterizing the buffer of this study, Stigter solved the nonlinear Poisson model for a DNA segment to find $d_{\text{eff}}=9$ nm. Substituting Stigter’s value into Onsager’s expression, we find $\nu=34,000$ nm³. Figure 28(b) presents a comparison of experiment measurements to excluded volume-extended theory. Agreement is excellent throughout, and without any fitting parameters, deviation from the experimental results is even smaller than for the case of fitted Kuhn length.

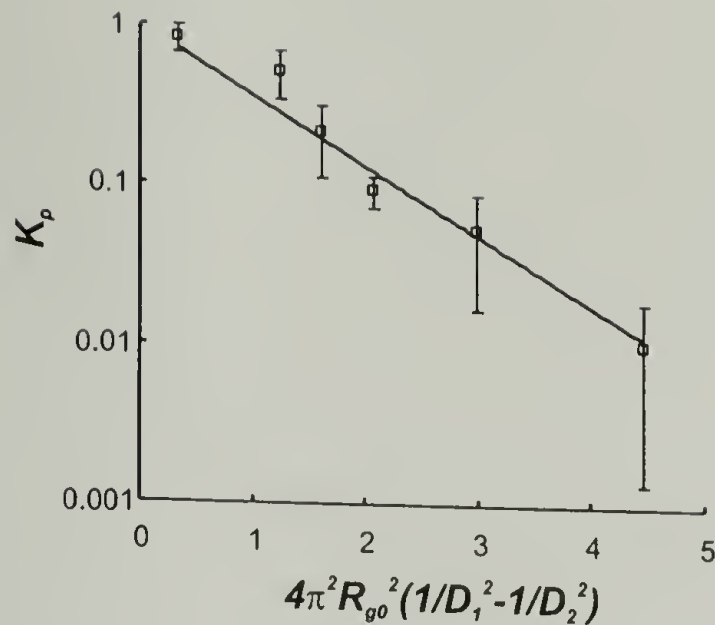


Figure 27. Experiment compared to theory for the Gaussian chain cavity-to-cavity partition coefficient K_p when b is fitted.

Several confinement studies[11-14] have treated excluded volume differently than has been thus far described, replacing $Lb/6$ of Casassa's formula by R_g^2 , the squared radius of gyration of the unconfined polymer in the presence of excluded volume. Conceptually, the excluded volume correction to K_p is thereby implemented prior to pore entry rather than afterwards. Unfortunately, given the minute sample amounts available, R_g is not available for our systems. If we adopt the usual scaling relationship for R_g , i.e., $R_g = aN^{3/5}$, and apply the alternative excluded volume treatment with a as a fitting parameter, theory and experiment mesh about as well as in Figure 28(b), a comparison shown in Figure 28(c). The fitted value for a is 15 nm providing a possibility to estimate the labeled DNA radius of gyration. Neither treatment of excluded volume is entirely satisfactory from the theoretical perspective, but the good agreement both offer for experimental data convincingly demonstrates the substantial impact of excluded volume on K_p when this parameter is less than 0.3.

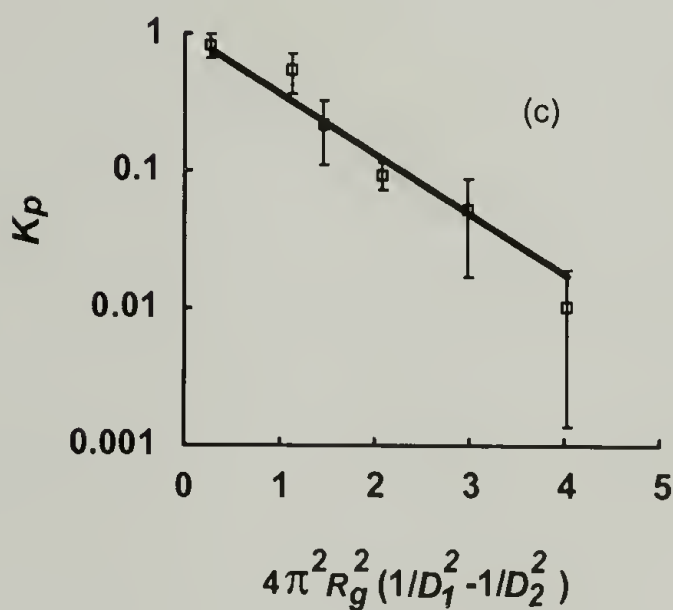
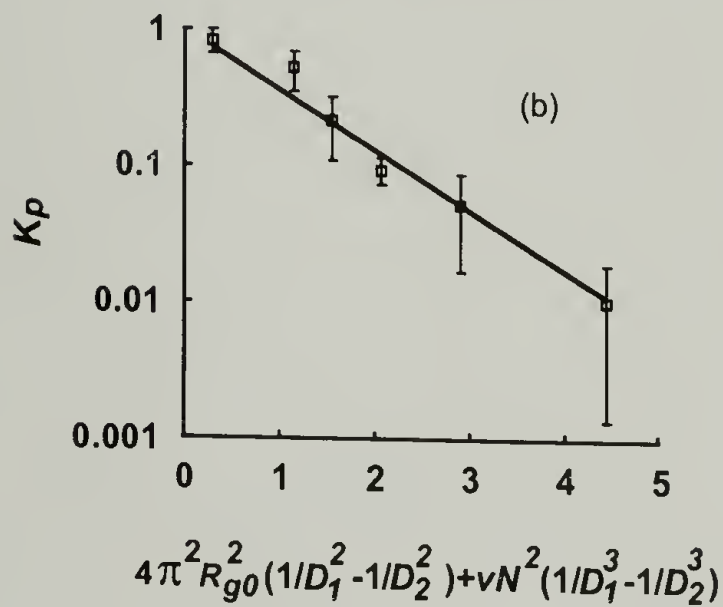
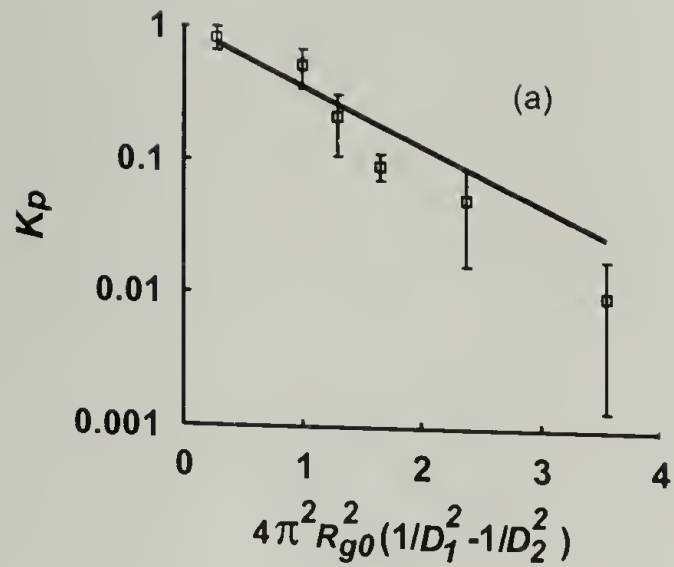


Figure 28 Experiment compared to theory for the cavity-to-cavity partition coefficient K_p : (a) Gaussian chain theory and (b), (c) excluded volume theory. In (b), correction for excluded volume is made by adding to the abscissa of (a) a term manifesting segment-segment repulsion. In (c), correction for excluded volume is made by replacing the unperturbed radius of gyration R_{g0} of (a) with a fitted scaling form for the perturbed radius of gyration R_g .

A correction for finite chain/segment length does not seem necessary to improve theory-experiment agreement. However, without theory or simulation results available for a semiflexible chain in a spherical cavity, we have no direct means to confirm this conclusion rigorously. Confinement in closed cavities of the type examined here, those which fully encase trapped chains, differs significantly from confinement in unbounded slit or cylinder pores, which offer unlimited chain stretching in one or more directions.[7, 15] For the latter geometries, de Gennes showed through the notion of “blobs” that the scaling relationship $\Delta S_c \sim N$ could easily be modified to account for excluded volume;[16] the premise of the scaling argument does not hold in closed cavities for chains with excluded volume. The argument fails because one cannot depict the chain as a sequence of independent blobs, each with a size comparable to the local pore dimension. Unlike the experiments to be described next, confinement levels in these first partitioning experiments were always low enough to maintain the segment density of the confined polymer below the bulk overlap concentration. In terms of their physical dimensions, chains occupied volume fractions varying from 4×10^{-6} to 4×10^{-4} , for chain diameter $d=2.5$ nm; in terms of their larger, electrostatically defined dimensions, chains occupied volume fractions varying from 5×10^{-5} to 6×10^{-3} , for chain diameter $d_{\text{eff}}=9$ nm.

Strong Confinement

In this round of experiments, we explored polymer partitioning under “strong” confinement conditions, those for which R_{g0} approaches or exceeds cavity diameter. A

single DNA (48,502 bp; $R_{go} = 420$ nm) was examined in a two-dimensional hexagonally packed monolayer of interconnected, equal-sized cavities (diameter = 920 nm). Difficulty inserting DNA into cavities at strong confinement underscored the change of protocols from the previous round of experiments. Valid realizations are much more abundant in cavity monolayers than in isolated cavity pairs.

In these partitioning experiments, the propensity of a single, large, and strongly confined DNA molecule to bridge or straddle between two equal-sized cavities was explored. These experiments focused on just one DNA species trapped in cavities of just one size, the polymer's radius of gyration selected to exceed the cavity radius. The latter condition was observed to change confinement behavior abruptly from that described already. The immediately obvious difference is dominance of bridging configurations.

To quantify these configurations, we defined an asymmetry parameter α to designate how chain segments split among cavities. Referencing the cavities by subscripts 1 and 2, $\alpha = (I_2 - I_1)/(I_2 + I_1)$, where I_i is the integrated fluorescence intensity of cavity i . We established that for a single confined chain, the total intensity $I_2 + I_1$ is constant, a fact confirming linear response of integrated intensity with respect to number of segments. As a polymer moved from complete confinement in cavity 1 to complete confinement in cavity 2, α shifted from -1 to $+1$, passing through 0 when the segment split was even. Because observing strong confinement in isolated cavity pairs proved problematical (we never observed even a single realization for the polymer/cavity combination we now discuss), behavior at this condition was studied in hexagonally closed-packed cavity arrays, which produce abundant realizations. Each

cavity in an array has six interconnecting holes, which combine to perturb idealized spherical confinement more so than do the single holes of isolated cavity pairs.

Although observed regularly, the minority of polymer configurations involving three or more cavities was simply ignored. Statistical analysis provided the function $P(\alpha)$, the probability of a particular bridging configuration. By definition, $P(\alpha)$ is symmetric about $\alpha = 0$. The Boltzmann distribution transforms $P(\alpha)$ to $\Delta F(\alpha)$, the free energy distribution for two-cavity configurational states.

Figure 29 displays $\Delta F(\alpha)/kT$ for 48,502 bp DNA trapped in 920 nm diameter cavities, a polymer/cavity combination producing frequent bridging. Indeed, the figure demonstrates that the equally split configuration, $\alpha = 0$, is the one of lowest free energy. Slightly less favored, by about $1 kT$, are the fully asymmetric configurations, $\alpha = \pm 1$, that place the molecule wholly in one of the two cavities. The $\alpha = \pm 1$ configurations are separated from the $\alpha = 0$ configuration by an energy barrier of about $3 kT$. The curve of Figure 29 demonstrates that a strongly confined polymer with excluded volume must overcome a doubly peaked energy barrier to move from one cavity to another. Smaller polymers, such as those analyzed earlier, must only surmount a singly peaked energy barrier at $\alpha = 0$, making bridging configurations unstable. Consequently, these configurations were relatively rarer than for larger chains and also more fleeting. These characters prevented us from developing meaningful free energy histograms with a single peak. Nonetheless, the observed dynamics unequivocally reveals singly peaked energy barriers for smaller chains, i.e. these chains do not pause at all as they pass through $\alpha = 0$. For 920 nm diameter cavities, the crossover DNA size characterizing

the switch from doubly to singly peaked barrier seems to be about 20-25 kbp, roughly corresponding to R_g equal to cavity radius.

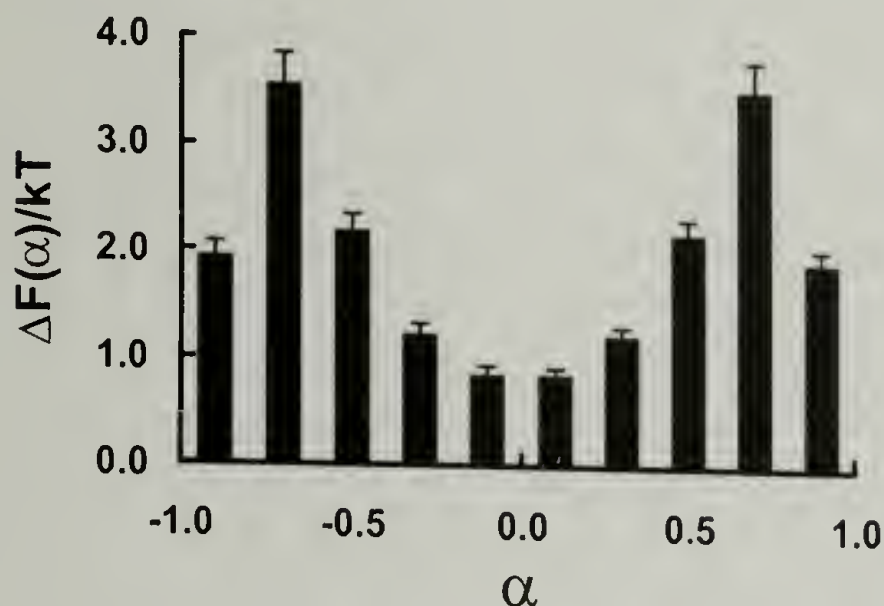


Figure 29. Free energy histogram for configurations adopted by 48,502 bp DNA in a pair of 920 nm diameter cavities. The asymmetry parameter α reflects the split of the chain segments between cavities. Cavities, with $\alpha = 0$ representing configurations which exactly balance the chain between cavities and $\alpha = \pm 1$ representing configurations with the chain localized to a single cavity.

The origins of stable bridging configurations are clear. As a DNA molecule traverses from one cavity to another, the intervening hole “pinches” the molecule’s midsection, costing it configurational entropy. The molecule can avoid this penalty by escaping to a single cavity. But for a strongly confined chain with excluded volume the escape also has its cost, as single cavity configurations increase repulsive segmental interactions. These interactions are weakest in the symmetric, pinched configuration, where the spreading of segments over the full accessible volume minimizes crowding. The excluded volume effect is negligible at low molecular weight, allowing pinched configurations to be avoided, but dominates at high molecular weight, where pinched configurations are not just tolerated but favored. For chains with excluded volume,

bridging configurations first become stable when R_g exceeds about the cavity radius. Thus, from a different perspective, bridging can be viewed as a mechanism for excluded volume chains to evade strong confinement.[17] Gaussian chains also bridge, but only due to fluctuations. Since the various energies are all of order kT , simulations will be necessary to explore tradeoffs fully.

Although an old topic, polymer partitioning has not previously been scrutinized by experiment in such a detailed manner. This work pioneers the study of partitioning in highly ordered environments – a longstanding problem to the polymer separations community – and introduces the quantitative measurement of polymer partition coefficients by direct visualization – a task made feasible by recent innovations in single molecule imaging. In combination, these contributions point toward a rigorous, molecule-level assessment of both classic and new partitioning theories. Such assessments are needed as new nanotechnologies, with pore spaces optimized for separation efficiency and speed, replace conventional disordered polymer separation media.

The partitioning behaviors reported here for flexible polymers are consistent with both theoretical expectations and past measurements. As the single molecule method improves so as to produce more realizations in a greater variety of confinement geometries, many nuances of partitioning should become open for study for the first time. The current results highlight complications associated with excluded volume, a property of relevance to nearly all applications of partitioning.

References

1. Nykypanchuk, D., H.H. Strey, and D.A. Hoagland, *Science*, 2002. **297**(5583): p. 987-990.
2. Casassa, E.F., *J. Polym. Sci. B*, 1967. **5**(9PB): p. 773-778.
3. Bordelon, J.A., et al., *Journal of Physical Chemistry B*, 2002. **106**(18): p. 4838-4843.
4. Perkins, T.T., et al., *Science*, 1995. **268**(5207): p. 83-87.
5. Smith, D.E., T.T. Perkins, and S. Chu, *Macromolecules*, 1996. **29**(4): p. 1372-1373.
6. Yamakawa, H. and M. Fujii, *Macromolecules*, 1973. **6**(3): p. 407-415.
7. Grosberg, A.Y. and A.R. Khohlov, *Statistical Physics of Macromolecules*. AIP Series in Polymers and Complex Materials, ed. P.P. Pincus. 1994, New York: American Institute of Physics.
8. Onsager, L., *Annals of the New York Academy of Sciences*, 1949. **51**(4): p. 627-659.
9. Odijk, T., *Macromolecules*, 1983. **16**(8): p. 1340-1344.
10. Stigter, D. and K.A. Dill, *Macromolecules*, 1995. **28**(15): p. 5325-5337.
11. Cifra, P., T. Bleha, and A. Romanov, *Polymer*, 1988. **29**(9): p. 1664-1668.
12. Cifra, P. and T. Bleha, *Macromolecules*, 2001. **34**(3): p. 605-613.
13. Bleha, T., P. Cifra, and F.E. Karasz, *Polymer*, 1990. **31**(7): p. 1321-1327.
14. Teraoka, I., *Progress in Polymer Science*, 1996. **21**(1): p. 89-149.

15. Jaeckel, A. and J. Dayantis, *Journal of Physics a-Mathematical and General*, 1994. **27**(23): p. 7719-7731.
16. de Gennes, P.G., *Scaling Concepts in Polymer Physics*. 1979, Ithaca: Cornell Univ. Press.
17. Kong, C.Y. and M. Muthukumar, *Journal of Chemical Physics*, 2004. **120**(7): p. 3460-3466.

BIBLIOGRAPHY

- Akerman B, Tuite E: *Nucleic Acids Res.* 1996, **24**:1080-1090.
- Akerman B: *Phys. Rev. E* 1996, **54**:6685-6696.
- Akerman B: *J. Chem. Phys.* 1997, **106**:6152-6159.
- Akerman B: *J. Phys. Chem. B* 1998, **102**:8909-8922.
- Alon U, Mukamel D: *Phys. Rev. E* 1997, **55**:1783-1793.
- Bartlett P, Ottewill RH, Pusey PN: *Phys. Rev. Lett.* 1992, **68**:3801-3804.
- Baumgartner A: *J. Chem. Phys.* 1982, **76**:4275-4280.
- Baumgärtner A, Muthukumar M: *J. Chem. Phys.* 1987, **87**:3082-3088.
- Baumgärtner A, Muthukumar M: *Adv. Chem. Phys.* 1996, **XCIV**:625-708.
- Bernal JMG, Tirado MM, Freire JJ, Delatorre JG: *Macromolecules* 1990, **23**:3357-3362.
- Besnier CE, Kong HM: *EMBO Rep.* 2001, **2**:782-786.
- Betzig E, Chichester RJ: *Science* 1993, **262**:1422-1425.
- Bezrukov SM, Vodyanoy I, Brutyan RA, Kasianowicz JJ: *Macromolecules* 1996, **29**:8517-8522.
- Bielawski CW, Benitez D, Grubbs RH: *Science* 2002, **297**:2041-2044.
- Bleha T, Cifra P, Karasz FE: *Polymer* 1990, **31**:1321-1327.
- Bloomfield VA, Crothers DM, Tinoco I: *Nucleic acids : structures, properties, and functions*. Sausalito, Calif.: University Science Books; 2000.

- Bordelon JA, Feierabend KJ, Siddiqui SA, Wright LL, Petty JT: *J. Phys. Chem. B* 2002, **106**:4838-4843.
- Braun PV, Zehner RW, White CA, Weldon MK, Kloc C, Patel SS, Wiltzius P: *Adv. Mater.* 2001, **13**:721-724.
- Bustamante C, Marko JF, Siggia ED, Smith S: *Science* 1994, **265**:1599-1600.
- Cabodi M, Turner SWP, Craighead HG: *Anal. Chem.* 2002, **74**:5169-5174.
- Casassa EF: *J. Polym. Sci. B* 1967, **5**:773-778.
- Casassa EF, Tagami Y: *Macromolecules* 1969, **2**:14-&.
- Chou C-F, Bakajin O, Turner SWP, Duke TAJ, Chan SS, Cox EC, Craighead HG, Austin RH: *PNAS* 1999, **96**:13762-13765.
- Cifra P, Bleha T, Romanov A: *Polymer* 1988, **29**:1664-1668.
- Cifra P, Bleha T: *Macromolecules* 2001, **34**:605-613.
- Cohen G, Eisenber.H: *Biopolymers* 1966, **4**:429-&.
- Colton CK, Lai CJ, Satterfield CN: *AIChE J.* 1975, **21**:289-298.
- Daoud M, de Gennes PG: *J. Phys. (Paris)* 1977, **38**:85-93.
- Davidson MG, Suter UW, Deen WM: *Macromolecules* 1987, **20**:1141-1146.
- de Gennes PG: *Scaling Concepts in Polymer Physics*. Ithaca: Cornell Univ. Press; 1979.
- deGennes PG: *J. Chem. Phys.* 1971, **55**:572-579.
- Deniz AA, Laurence TA, Dahan M, Chemla DS, Schultz PG, Weiss S: *Annual Review of Physical Chemistry* 2001, **52**:233-253.

Denkov ND, Velev OD, Kralchevsky PA, Ivanov IB, Yoshimura H, Nagayama K:
Langmuir 1992, **8**:3183-3190.

Dimitrov AS, Dushkin CD, Yoshimura H, Nagayama K: *Langmuir* 1994, **10**:432-440.

Doi M, Edwards SF: *J. Chem. Soc. Faraday Trans. II* 1978, **74**:1789-1801.

Doi M, Edwards SF: *The theory of polymer dynamics*. Oxford, New York: Clarendon Press ;Oxford University Press; 1987.

Doyle PS, Bibette J, Bancaud A, Viovy J-L: *Science* 2002, **295**:2237.

Einstein A: *Ann. Phys.* 1905, **17**:549-560.

Einstein A: *Z. Electrochem. Angew. Phys. Chem.* 1908, **14**:235-239.

Engel A, Gaub HE, Muller DJ: *Curr. Biol.* 1999, **9**:R133-R136.

Fixman M, Skolnick J: *Macromolecules* 1978, **11**:863-867.

Foquet M, Korlach J, Zipfel W, Webb WW, Craighead HG: *Anal. Chem.* 2002, **74**:1415-1422.

Friddle RW, Klare JE, Martin SS, Corzett M, Balhorn R, Baldwin EP, Baskin RJ, Noy A: *Biophys. J.* 2004, **86**:1632-1639.

Garcia-Parajo MF, Veerman JA, Ruitter AGT, van Hulst NF: *Ultramicroscopy* 1998, **71**:311-319.

Giddings JC, Kucera E, Russell CP, Myers MN: *J. Phys. Chem.* 1968, **72**:4397-&.

Gilbert EP, Auvray L, Lal J: *Macromolecules* 2001, **34**:4942-4948.

Gosnell DL, Zimm BH: *Macromolecules* 1993, **26**:1304-1308.

- Grosberg A, Nechaev S: *Adv. Polym. Sci.* 1993, **106**:1-29.
- Grosberg AY, Khohlov AR: *Statistical Physics of Macromolecules*. Edited by Larson RG, Pincus PP. New York: American Institute of Physics; 1994.
- Guillot G, Läger L, Rondelez F: *Macromolecules* 1985, **18**:2531-2537.
- Gurrieri S, Wells KS, Johnson ID, Bustamante C: *Anal. Biochem.* 1997, **249**:44-53.
- Ha T, Enderle T, Ogletree DF, Chemla DS, Selvin PR, Weiss S: *Proc. Natl. Acad. Sci. U. S. A.* 1996, **93**:6264-6268.
- Han J, Craighead HG: *J. Vac. Sci. Technol. A-Vac. Surf. Films* 1999, **17**:2142-2147.
- Han J, Turner SW, Craighead HG: *Phys. Rev. Lett.* 1999, **83**:1688-1691.
- Han J, Craighead HG: *Science* 2000, **288**:1026-1029.
- Han JY, Craighead HG: *Anal. Chem.* 2002, **74**:394-401.
- Haus JW, Kehr KW: *Phys. Rep.* 1987, **150**:263-406.
- Higgins LS, Besnier C, Kong HM: *Nucleic Acids Res.* 2001, **29**:2492-2501.
- Houseal TW, Bustamante C, Stump RF, Maestre MF: *Biophys. J.* 1989, **56**:507-516.
- Huang LR, Silberzan P, Tegenfeldt JO, Cox EC, Sturm JC, Austin RH, Craighead H: *Phys. Rev. Lett.* 2002, **89**.
- Huang LR, Cox EC, Austin RH, Sturm JC: *Anal. Chem.* 2003, **75**:6963-6967.
- Jaeckel A, Dayantis J: *J. Phys. A* 1994, **27**:2653-2667.
- Jaeckel A, Dayantis J: *J. Phys. A* 1994, **27**:7719-7731.

- Jiang P, Bertone JF, Hwang KS, Colvin VL: *Chem. Mater.* 1999, **11**:2132-2140.
- Jiang P, Hwang KS, Mittleman DM, Bertone JF, Colvin VL: *J. Am. Chem. Soc.* 1999, **121**:11630-11637.
- Jiang P, Bertone JF, Colvin VL: *Science* 2001, **291**:453-457.
- Kaji N, Tezuka Y, Takamura Y, Ueda M, Nishimoto T, Nakanishi H, Horiike Y, Baba Y: *Anal. Chem.* 2004, **76**:15-22.
- Käs J, Strey H, Sackmann E: *Nature* 1994, **368**:226-229.
- Kholodenko AL: *Macromol. Theory Simul.* 1996, **5**:1031-1064.
- Kiely CJ, Fink J, Brust M, Bethell D, Schiffrin DJ: *Nature* 1998, **396**:444-446.
- Kiriy A, Gorodyska G, Minko S, Jaeger W, Stepanek P, Stamm M: *Journal of the American Chemical Society* 2002, **124**:13454-13462.
- Kirsch AK, Meyer CK, Jovin TM: *J. Microsc.-Oxf.* 1997, **185**:396-401.
- Klein J: *Macromolecules* 1986, **19**:105-118.
- Kong CY, Muthukumar M: *J. Chem. Phys.* 2004, **120**:3460-3466.
- Korlach J, Foquet M, Zipfel W, Webb WW, Craighead HG: *Biophys. J.* 2002, **82**:361A-361A.
- Lal J, Gilbert EP, Auvray L: *Physica a-Statistical Mechanics and Its Applications* 2002, **304**:244-248.
- Lee W, Lee H, Lee HC, Cho D, Chang T, Gorbunov AA, Roovers J: *Macromolecules* 2002, **35**:529-538.
- Limbach KW, Nitsche JM, Wei J: *AIChE J.* 1989, **35**:42-52.

- Liu L, Li P, Asher SA: *J. Am. Chem. Soc.* 1998, **121**:4040-4046.
- Liu L, Li PS, Asher AS: *Journal of the American Chemical Society* 1999, **121**:4040-4046.
- Liu L, Li PS, Asher SA: *Nature* 1999, **397**:141-144.
- Lodge TP, Rotstein NA, Prager S: *Adv. Chem. Phys.* 1990, **79**:1-132.
- Long D, Viovy JL: *Phys. Rev. E* 1996, **53**:803-811.
- Long D, Viovy JL: *Physica A* 1997, **244**:238-253.
- Maier B, Rädler JO: *Macromolecules* 2000, **33**:7185-7194.
- Marko JF: *Physica A* 1997, **244**:263-277.
- Masaro L, Zhu XX: *Prog. Polym. Sci.* 1999, **24**:731-775.
- Matsumoto M, Sakaguchi T, Kimura H, Doi M, Minagawa K, Matsuzawa Y, Yoshikawa K: *J. Polym. Sci.: Part B: Polym. Phys.* 1992, **30**:779-783.
- Meistermann L, Tinland B: *Phys. Rev. E* 2000, **62**:4014-4017.
- Montanari A, Mezard M: *Phys. Rev. Lett.* 2001, **86**:2178-2181.
- Morgan RD, Calvet C, Demeter M, Agra R, Kong HM: *Biol. Chem.* 2000, **381**:1123-1125.
- Muller M, Wittmer JP, Cates ME: *Phys. Rev. E* 2000, **61**:4078-4089.
- Muthukumar M, Baumgärtner A: *Macromolecules* 1989, **22**:1937-1941.
- Muthukumar M, Baumgärtner A: *Macromolecules* 1989, **22**:1941-1946.

- Muthukumar M: *J. Non-Cryst. Solids* 1991, **131**:654-666.
- Muthukumar M: *J. Chem. Phys.* 2003, **118**:5174-5184.
- Naghizad.J, Sotobaya.H: *J. Chem. Phys.* 1974, **60**:3104-3108.
- Nykypanchuk D, Strey HH, Hoagland DA: *Science* 2002, **297**:987-990.
- Obukhov SP, Rubinstein M, Duke T: *Phys. Rev. Lett.* 1994, **73**:1263-1266.
- Odijk T: *Macromolecules* 1983, **16**:1340-1344.
- Ogston AG: *Trans. Faraday. Soc.* 1958, **54**:1754-1757.
- Onsager L: *Ann. NY Acad. Sci.* 1949, **51**:627-659.
- Park SH, Xia Y: *Chem. Mater.* 1998, **10**:1745-1747.
- Perkins TT, Quake SR, Smith DE, Chu S: *Science* 1994, **264**:822-826.
- Perkins TT, Smith DE, Chu S: *Science* 1994, **264**:819-822.
- Perkins TT, Smith DE, Larson RG, Chu S: *Science* 1995, **268**:83-87.
- Perkins TT, Smith DE, Chu S: *Science* 1997, **276**:2016-2021.
- Rodbard D, Chrambac.A: *Proc. Natl. Acad. Sci. U. S. A.* 1970, **65**:970-&.
- Roovers J: *Macromolecules* 1988, **21**:1517-1521.
- Rotstein NA, Lodge TP: *Macromolecules* 1992, **25**:1316-1325.
- Rubinstein M: *Phys. Rev. Lett.* 1986, **57**:3023-3026.

- Rubinstein M, Colby RH: *Polymer physics*. Oxford ; New York: Oxford University Press; 2003.
- Rye HS, Yue S, Wemmer DE, Quesada MA, Haugland RP, Mathies RA, Glazer AN: *Nucleic Acids Res.* 1992, **20**:2803-2812.
- Rye HS, Dabora JM, Quesada MA, Mathies RA, Glazer AN: *Anal. Biochem.* 1993, **208**:144-150.
- Sambrook J, Russell DW: *Molecular cloning : a laboratory manual* edn 3rd. Cold Spring Harbor, N.Y.: Cold Spring Harbor Laboratory Press; 2001.
- Satterfield CN, Colton CK, Turckheim BD, Copeland TM: *AIChE J.* 1978, **24**:937-940.
- Semenov AN, Joanny JF: *Phys. Rev. E* 1997, **55**:789-799.
- Sikorski A, Romiszowski P: *J. Chem. Phys.* 2004, **120**:7206-7211.
- Slater GW, Mayer P, Drouin G: *Methods Enzymol.* 1996, **270**:272-295.
- Smisek DL, Hoagland DA: *Science* 1990, **248**:1221-1223.
- Smith DE, Perkins TT, Chu S: *Phys. Rev. Lett.* 1995, **75**:4146-4149.
- Smith DE, Perkins TT, Chu S: *Macromolecules* 1996, **29**:1372-1373.
- Stigter D, Dill KA: *Macromolecules* 1995, **28**:5325-5337.
- Strick TR, Croquette V, Bensimon D: *Nature* 2000, **404**:901-904.
- Tegenfeldt JO, Prinz C, Cao H, Huang RL, Austin RH, Chou SY, Cox EC, Sturm JC: *Anal. Bioanal. Chem.* 2004, **378**:1678-1692.
- Teraoka I, Langley KH, Karasz FE: *Macromolecules* 1992, **25**:6106-6112.

- Teraoka I: *Macromolecules* 1996, **29**:2430-2439.
- Teraoka I: *Progress in Polymer Science* 1996, **21**:89-149.
- Tsonchev S, Coalson RD: *Chem. Phys. Lett.* 2000, **327**:238-244.
- Turner SW, Perez AM, Lopez A, Craighead HG: *J. Vac. Sci. Technol. B.* 1998, **16**:3835-3840.
- Turner SWP, Cabodi M, Craighead HG: *Phys. Rev. Lett.* 2002, **88**.
- Velikov KP, Christova CG, Dullens RPA, van Blaaderen A: *Science* 2002, **296**:106-109.
- Viovy JL, Leseq J: *Adv. Polym. Sci.* 1994, **114**:1-41.
- Volkmoth WD, Austin RH: *Nature* 1992, **358**:600-602.
- Volkmoth WD, Duke T, Austin RH, Cox EC: *Proc. Natl. Acad. Sci. U. S. A.* 1995, **92**:6887-6891.
- Weiss S: *Science* 1999, **283**:1676-1683.
- White JA, Deen WM: *Macromolecules* 2000, **33**:8504-8511.
- Xu Y, Lunnen KD, Kong HM: *Proc. Natl. Acad. Sci. U. S. A.* 2001, **98**:12990-12995.
- Yamakawa H, Fujii M: *Macromolecules* 1973, **6**:407-415.
- Yoon HG, Deutsch JM: *J. Chem. Phys.* 1995, **102**:9090-9095.
- Zhu ZY, Samuelson JC, Zhou J, Dore A, Xu SY: *J. Mol. Biol.* 2004, **337**:573-583.
- Zimm BH, Lumpkin O: *Macromolecules* 1993, **26**:226-234.

